SUBNANOSECOND PULSE RADIOLYSIS STUDIES

BY

STEPHEN CHARLES WALLACE

B.Sc.(Hons)   University of British Columbia, 1967.

A THESIS SUBMITTED IN PARTIAL FULFILMENT OF

THE REQUIREMENTS FOR THE DEGREE OF

DOCTOR OF PHILOSOPHY

in the Department

of

Chemistry

We accept this thesis as conforming to the required

standard

THE UNIVERSITY OF BRITISH COLUMBIA

In presenting this thesis in partial fulfilment of the requirements for an advanced degree at the University of British Columbia, I agree that the Library shall make it freely available for reference and study. I further agree that permission for extensive copying of this thesis for scholarly purposes may be granted by the Head of my Department or by his representatives. It is understood that copying or publication of this thesis for financial gain shall not be allowed without my written permission.

Department of __CHEMISTRY__

The University of British Columbia
Vancouver 8, Canada

Date __May 25, 1971__

Abstract

This thesis reports pulse radiolysis investigations on the very early physicochemical and chemical events in the radiation chemistry of polar liquids, in particular liquid water, where transient absorptions due to the hydrated electron have been observed with lifetimes as short as $\sim$ 30 picoseconds. These studies were carried out using the novel technique of Cerenkov reabsorption spectroscopy, which in conjunction with an extremely high dose-rate electron accelerator (peak dose-rate = 1.8 x 10^{28} eV cm^{-2} sec^{-1}) yields information pertaining to subnanosecond radiation chemical events from measurements made with existing nanosecond technology. A critical evaluation of all experimental aspects of this newly developed technique, as well as a partial theoretical analysis of the relationships between the physical parameters and experimental observables, have both been performed in order to establish the validity of such pulse radiolysis studies.

Kinetic effects in molar concentrations of hydrated electron scavengers and relative solvated electron yields in water and the alcohols, have been interpreted to suggest that the time-scale of charge neutralization in radiation chemistry is very much shorter than previously proposed, thus necessitating a modification of the existing description of subnanosecond events as contained in the spur diffusion model for radiation chemical yields.

The primary reducing species in the radiolysis of formamide, a liquid of very high dielectric constant, was postulated as a negative ion, rather than a solvated electron; this negative ion being formed directly by solvent scavenging of thermalized electrons.

With the availability of new spectral data for solvated electrons from this and other work, a revival of the earlier suggested spectral correlation with iodide ion C.T.T.S. spectra has been proposed, with many of the earlier discrepancies now removed.

Finally, because absorption spectra are deduced from light emission measurements in the Cerenkov reabsorption technique, an added feature of this work was the possible observation of radiation-induced molecular luminescence from liquid water; however over the spectral range 200 nm - 850 nm the limiting 100 eV yield of such luminescence was $\leqslant 10^{-3}$ with a lifetime $\leqslant 2$ nanoseconds.

Acknowledgements

I would like to sincerely thank Dr. David C. Walker
for his guidance and understanding during the course of this
work and for sharing his scientific insight in the many
valuable discussions we have had.

I would also like to acknowledge the cooperation of the
technical staff in this Department, in particular, the skills of
Mr. Cedric Neale and Mr. Mark Vagg of the Mechanical Workshop.

To Geraldine

Hypotheses are nets: only he who casts will catch.

NOVALIS

TABLE OF CONTENTS

LIST OF FIGURES

CHAPTER I

A SURVEY OF RADIATION CHEMISTRY

Introductory Remarks

After over a decade of intensive research into the interaction of
high energy radiation with matter, what is really needed in radiation
chemistry is a definitive interpretation of that which is already known.
There is now a staggering amount of information about radiation chemical
yields and the reactions of radiation induced transient species, but
the initial objective of all work in this field, the elucidation of
the primary events of energy deposition and transfer, has been an
extremely elusive goal. The basic problem in attempts to study primary
radiation physical and chemical events has been the extremely short
time scale on which these processes occur. As a result of this temporal
difficulty, the theories of radiation chemistry must in general predict
short time scale events from theoretical deductions based on phenomeno-
logical models derived from long time scale measurements on secondary
species. Therefore, the aim of research on primary processes in radiation
chemistry has been the earliest observation of the highly reactive
transient species formed when radiation interacts with matter. The most
fruitful line of approach in such studies has been the technique of pulse
radiolysis, which over the past few years has advanced from microsecond
(1,2), to nanosecond (3), and finally picosecond (4) time resolution.
The significant advantage of this technique is that, in principle, it

allows one to make direct physical measurements on the yields and rates of reaction of the short-lived radiation-induced transient species on which ones studies are directed. This thesis describes some nanosecond and subnanosecond pulse radiolysis studies on polar liquids, carried out using significantly higher radiation fluxes than any previously reported. The results of this work are extremely relevant at the present time, because they are the first set of data which can be meaningfully compared to the work of Hunt et al (4) on the picosecond pulse radiolysis of polar liquids.
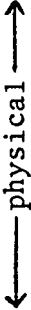
The complex sequence of events following the interaction of ionizing radiation with condensed matter and leading to an observable chemical change may be roughly categorized into the following temporal stages (Table I):

(i) first, the deposition of energy by the ionizing radiation, complete within $\sim 10^{-16}$ seconds

(ii) next, the physicochemical relaxation of the medium following the initial radiation induced excitations, giving rise to the primary chemical species such as solvated electrons and other radical species ($10^{-16} - 10^{-12}$ seconds)

(iii) finally, the diffusion and reaction of these chemical species to form stable products ($> 10^{-12}$ seconds).

The measure of radiation induced chemical change is called a G value and is defined as the number of chemical species formed per 100 eV deposited in the irradiated material. This G value has no intrinsic molecular significance as does a quantum yield in photo-chemistry, it is rather a macroscopic observation giving the stoi-chiometric energy efficiency for the formation of a given species.

TABLE I

Temporal Scale of Events in the Radiation Chemistry of Polar Liquids

-log(time)seconds		Classification
18	Duration of a single electron - electron interaction.	
16	Electronic transitions, ionisations and excitations.	
14	Subexcitation electrons, molecular vibrations, ion-molecule reactions involving H-atom transfer.	
13	Thermalised electrons, dissociation of molecules.	
12	Electron solvation and intraspur reactions.	
11-10	Intraspur reactions.	
9	Electronic emission from allowed transitions.	
8	Interspur reactions.	
7-6	Spur overlap and homogeneous kinetic behaviour.	
1	Thermal equilibrium.	

physical ——→

physicochemical ←——→

chemical ——→

In this definition one has the key to the understanding of energy transfer in radiation chemistry. That is, because energy deposition by ionizing radiations consists of a large number of random excitations both in magnitude and spatial distribution, the only meaningful observable is the average yield per unit energy absorbed. Starting from this point, it is perhaps clearer why the radiation chemist is so concerned with the generic effect of different types of ionizing radiation, since the G value measured is quite dependent on the microscopic mechanism of energy deposition. What follows, therefore, is a detailed discussion of energy transfer in radiation chemistry, from the incidence of the perturbing primary ionizing radiation to the final equilibrium state.

(A) The Physical Interactions of Ionizing Radiation

(1) Electromagnetic Radiation

The interaction of high energy photons with matter is analogous to the absorption of light, in the sense that in both cases photons are either totally absorbed in an individual event, or pass through the medium unaltered in energy (6). The absorption of γ-rays or X-rays (high energy photons are normally described as γ-rays if they originate from nuclear transitions and X-rays from extra nuclear interactions) therefore may be described by an equation of the following form:

$$I_t = I_o \exp\{-\mu x\} \tag{1-1}$$

where I_o = incident flux

I_t = transmitted flux

x = the thickness of the absorber

μ = the attenuation coefficient

Because there are several different energy dependent energy loss mechanisms the attenuation coefficient for a medium of a given atomic number is the sum of the absorption cross-sections for these different interactions.

$$\mu = \mu_a(E,Z) + \mu_b(E,Z) + \mu_c(E,Z) \qquad (1-2)$$

In equation 1-2, the subscripts refer to the following:

(a) The photoelectric effect, important for low photon energies (E < 500 keV). $\mu_a(E,Z) = \tau$

(b) The Compton effect, predominant in the medium energy range (500 keV < E < 5 MeV). This absorption coefficient also includes a term for attenuation due to elastic Compton scattering. $\mu_b(E,Z) = \sigma$

(c) Pair production, becoming the only interaction above photon energies of 20 MeV. $\mu_c(E,Z) = \kappa$

Their relative contributions to μ are shown as a function of energy for water and lead in figure 1-1(a) and 1-1(b).

(a) Photoelectric Effect and (b) Compton Scattering

The photoelectric effect describes the complete absorption of an incident photon and the subsequent transfer of its total energy to a bound electron, with the kinetic energy of this electron diminished by its binding energy in the medium according to the Einstein equation. Because nuclear recoil is required for momentum and energy conservation, only bound electrons may participate in this process, and the direction of the ejected photoelectron will be energy dependent, approaching but never reaching emission in the forward direction collinear with the path of the original high energy photon. As the energy of the incident photon increases, the cross-section for the photoelectric effect decreases, because the electron binding energy is so small in comparison
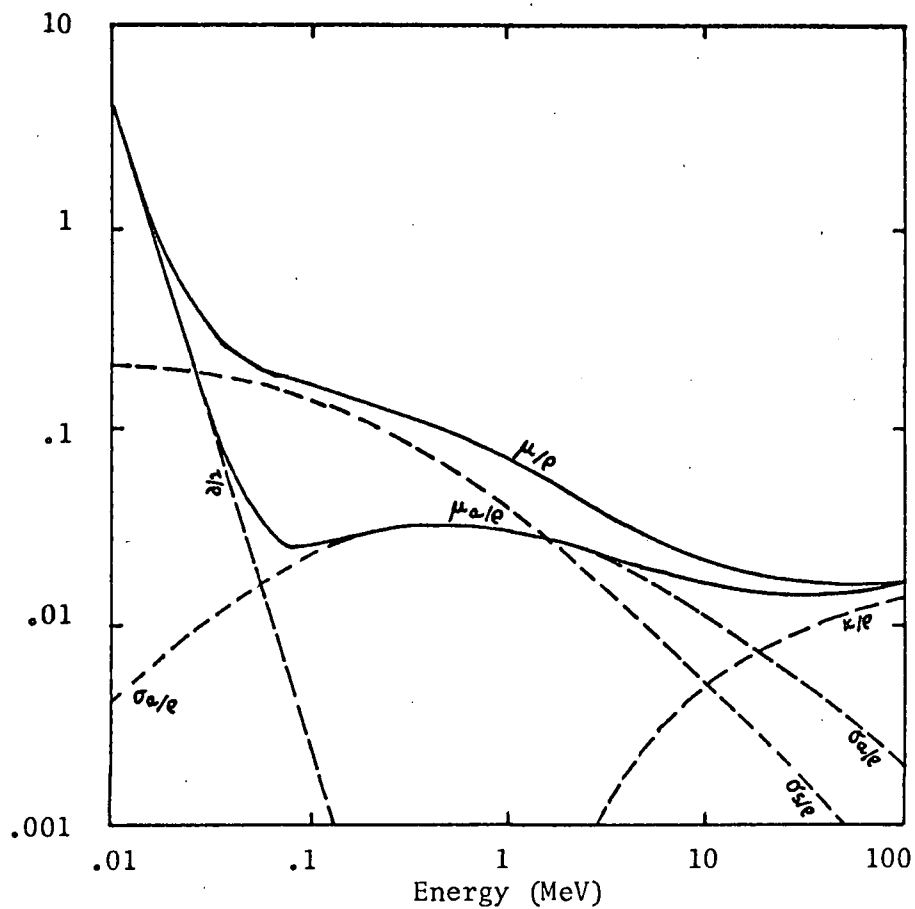
Figure 1-1 (a) and (b). Mass attenuation coefficients
for photons in water and lead respectively. Dashed
lines show relative absorption and scattering
contributions, the upper and lower solid lines are
the total attenuation and absorption coefficients
respectively.
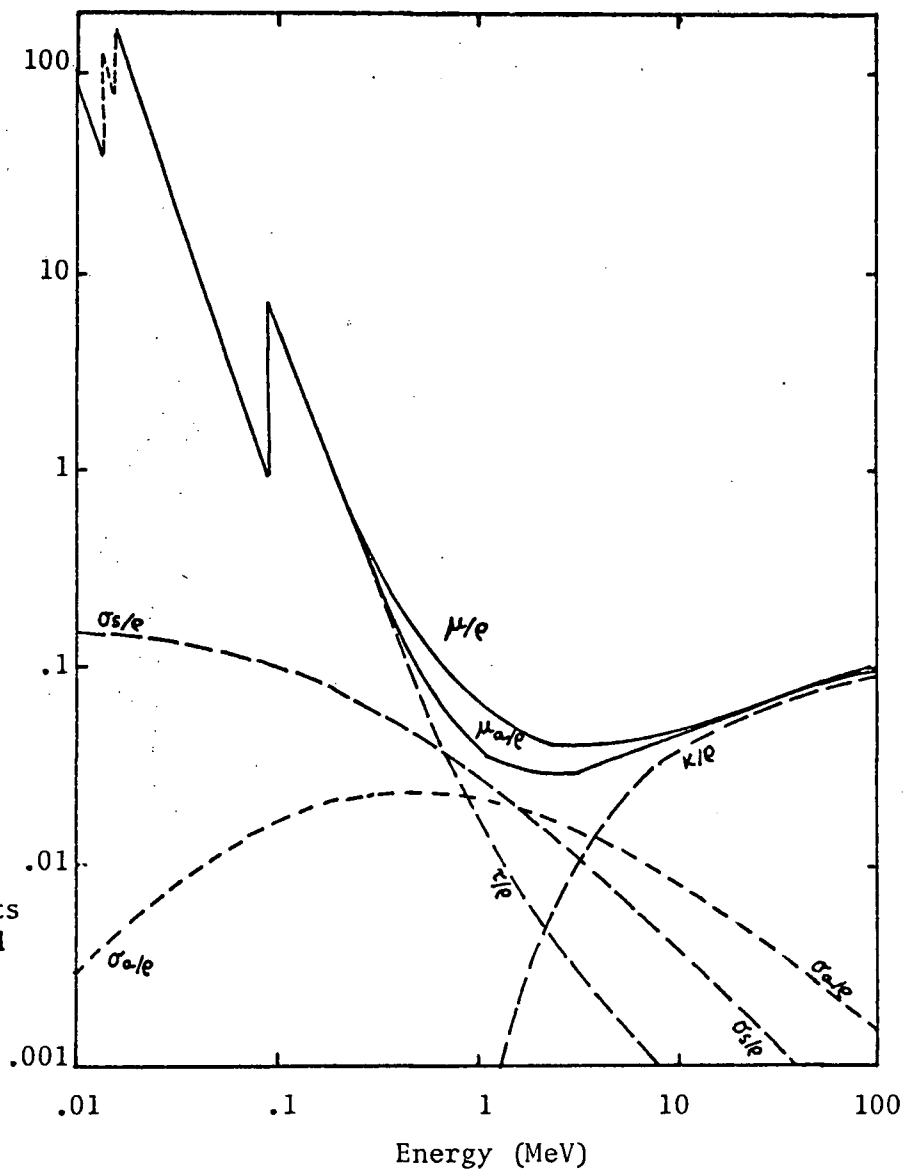
Fig. 1-1(b)

to the photon energy that the electrons in the medium may all be regarded as free. This type of γ-ray scattering by free electrons is called the Compton effect, the difference from the photoelectric effect being that the photon is not completely absorbed but only inelastically scattered, giving rise to both a high energy electron and a high energy photon travelling in appropriate directions for the conservation of energy and momentum as shown in figure 1-2.
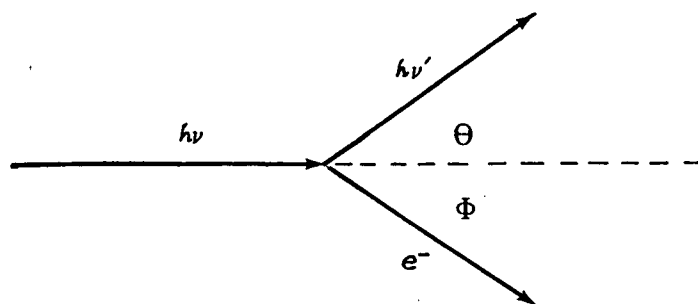
figure 1-2

The differential energy cross-sections for both photons and electrons have been evaluated theoretically using the Klein and Nishina cross-section (5) and these predictions have been experimentally verified in many different studies (6). Of principal interest to the radiation chemist is the fact that the average scattered electron energy is about one-half of the incident photon energy so that for a [60]Co γ-ray in water, the average Compton electron kinetic energy is ∿ 0.5 MeV. Furthermore, it should be noted that since the cross-section for γ-ray absorption of any kind is relatively low, once a Compton event has taken place the

scattered photon has a very low probability of further interaction with the medium, so that the analogy with the absorption of light cited at the beginning of this discussion still holds. Elastic scattering of γ-rays is also classified as Compton scattering. This effect must be separated out of the attenuation coefficient in order to get the true absorption cross-sections for the different energy loss mechanisms, and its contribution is shown dotted in figure 1-1(a) and 1-1(b).

(c) Pair Production

Above a γ-ray energy of 1.02 MeV a nuclear interaction called pair production, in which the photon is annihilated to give an electron positron pair whose total kinetic energy is the difference between the photon energy and the rest energy (1.02 MeV) of the two particles, becomes significant. Depending on its kinetic energy the positron either recombines with its sibling electron or escapes to combine with a medium electron, yielding two photons of energy one-half the sum of kinetic energy of the positron and the rest energy of the two particles. A similar electronic interaction, called triplet production with threshold energy 2.04 MeV, can also occur but it has a much lower cross-section.

Because of the high cross-section for the attenuation of fast electrons, the secondary electrons produced by the interaction of high energy photons with matter, rather than the few primary energy transfers by the high energy photons, are responsible for radiation-induced chemical change from γ-rays and X-rays. Thus equivalent radiation chemical effects can be achieved with either high energy photons or

electrons, the choice between the two based primarily on operational considerations.

(2) High Energy Electrons

Unlike high energy photons, a fast electron experiences a large number of elastic and inelastic interactions as it passed through matter. Furthermore, since the cross-sections for these processes are large, high energy electrons are rapidly attenuated depositing their energy directly into the medium along their track. Excluding electrons with energies greater than 10 MeV (not a limiting condition since processes taking place above 10 MeV are not directly significant to radiation chemistry) the important interactions are as follows:

(a) Coulomb scattering by the atomic nuclei:

(elastic scattering)

(b) Collisions with atomic electrons (inelastic scattering)

(c) Unrestricted losses in which no energy is deposited in the medium, such as Bremsstrahlung, Cerenkov radiation, transition radiation, etc.

(a) Elastic Scattering

The nuclear Coulomb scattering cross-section is predominantly in the forward direction, so that the electron experiences a large number of small angle deflections along its track. The experimentally measured angular distribution of scattered electrons from a thin target verifies the theoretical predictions (7,8) very well, in that the transmitted electrons form a sharply peaked Gaussian distribution about the forward direction with a very small tail towards large angles. In thick targets (0.5 electron range), Coulomb scattering cannot be

separated from inelastic scattering, however experimental data (9)
agrees well with theoretical simulations (9,10).

(b) Inelastic Collisions

In contrast to electron nuclear scattering, electron-electron
collisions can lead to the transfer of a substantial amount of energy
from the incident to the target electron. Although the cross-section
for electron scattering shows that most encounters involve small
losses (8), occasional hard collisions occur resulting in the
generation of secondary electrons called δ-rays, which branch off
the track of the primary electron (the primary electron being taken
as the higher energy particle following a collision). However, by means
of a statistical treatment over all possible energy transfers, it is
possible to obtain equations (in the continuous slowing down approximation,
csda) for the average rate of energy loss for high energy electrons.
Including relativistic effects, the complete quantum mechanical
expression for the average collisional energy loss of high energy
electrons is given by Bethe (11,12).

$$-\frac{dE}{dx} = \frac{2\pi N_o e^4 \rho Z}{m_o c^2 \beta^2 A} \left\{ \log \frac{m_o^2 c^4 \beta^2 (1-\sqrt{1-\beta^2}}{2I^2(1-\beta^2)^{3/2}} + (1-\beta^2)(\ln 2 + 9/8) - \sqrt{1-\beta^2}\,\frac{(1+2\ln 2)}{4} + \frac{1}{8} \right\}$$

$$(1-3)$$

where A = atomic weight of the absorber

Z = atomic number of the absorber

ρ = density of the absorber

N_o = Avogadro's number

e = the electron charge (statcoulombs)

m_o = the rest mass of the electron

c = velocity of light in vacuo

β = $\dfrac{v}{c}$, the ratio of the electron velocity to the speed of light. The electron kinetic energy and β are related by the following expression:

$$E = m_o c^2 \left(\frac{1}{\sqrt{1-\beta^2}} - 1 \right)$$ (1-4)

I = average excitation potential

Except for the average excitation potential I, all parameters in the Bethe equation are well known physical constants. This average excitation potential is an empirically measured atomic constant (only for H can it be calculated exactly) which is related to the total oscillator strength of the absorbing atoms. In molecules, I is calculated from an expression called the Bragg rule (13),

$$\log \langle I \rangle = \left\langle \frac{Z}{A} \right\rangle^{-1} \frac{1}{\rho} \Sigma_J \frac{Z_j}{A_j} \rho_j \cdot \log I_j$$ (1-5)

$$\left\langle \frac{Z}{A} \right\rangle = \frac{1}{\rho} \Sigma_J \frac{Z_j}{A_j} \rho_j$$ (1-6)

where the sum is taken over the j atomic constituents. Experimental measurements show that the Bragg rule holds very well (14), indicating that specific details of electronic structure in the absorber are not significant for high energy electron stopping.

In the plot of the Bethe equation given in figure 1-3, as the energy gets very large, the calculated energy loss is much greater than the
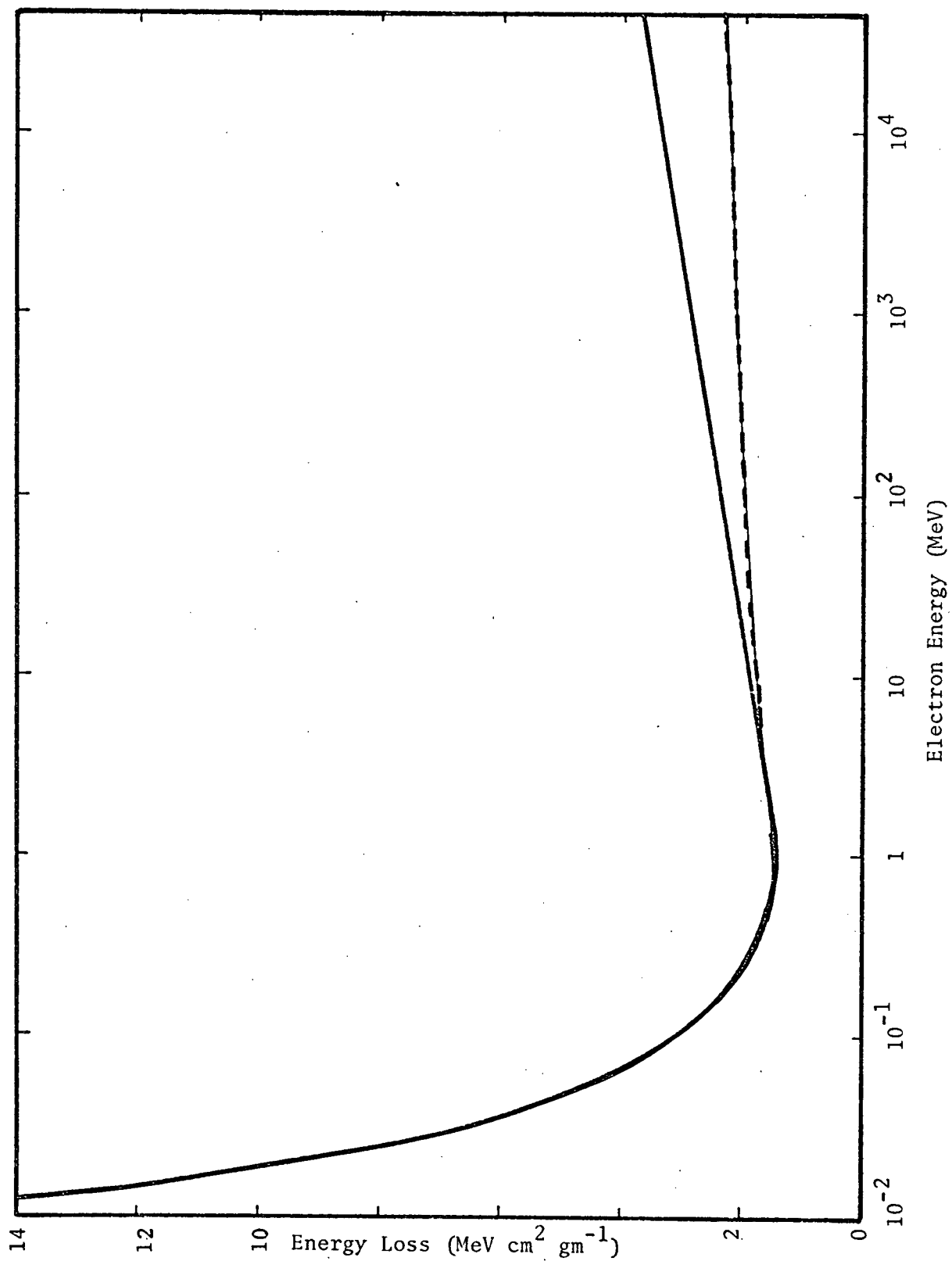
Figure 1-3. The average energy loss per unit pathlength in Aluminum from Bethe equation (solid line), and the correction due to the density effect (dotted line), versus electron energy.

experimentally observed value. This phenomenon is called the density effect

and is due to the reduction of the effective electric field of the

primary electron by the shielding effect of electron-induced polarization

of atoms or molecules adjacent to the electron track. Although the

density effect increases markedly in condensed media (hence its name),

it is negligible below 1 MeV in water and therefore, unimportant in

this work.

The Bethe equation is /vast oversimplification of the transport

of high energy electrons through matter, and in relatively thin absorbers

(~ 0.1 electron range) breaks down completely because it predicts an

explicit relationship between the electron kinetic energy and penetration.

This is untrue because electrons have a distribution of energy losses,

thus leading to energy straggling, which, compounded with a substantial

distribution of path lengths due to scattering, gives rise to a much

higher energy loss in a finite thickness absorber than that predicted

by the Bethe equation. For this reason, electrons do not show a well

defined range in absorbers; instead, as illustrated in both dose-depth

and transmission depth curves in figure 1-4(a) and 1-4(b), there is a long

tail approaching zero assymptotically at the maximum depth of penetration.

(c) Unrestricted Losses

Energy loss process are classified as unrestricted if the interaction

results in no energy deposition in the absorber. Although of no direct

significance to radiation chemistry a discussion of these phenomena is

important because of their primary relation to high energy electrons.

(i) Bremsstrahlung

An electron decelerated in nuclear Coulomb fields emits Bremsstrahlung
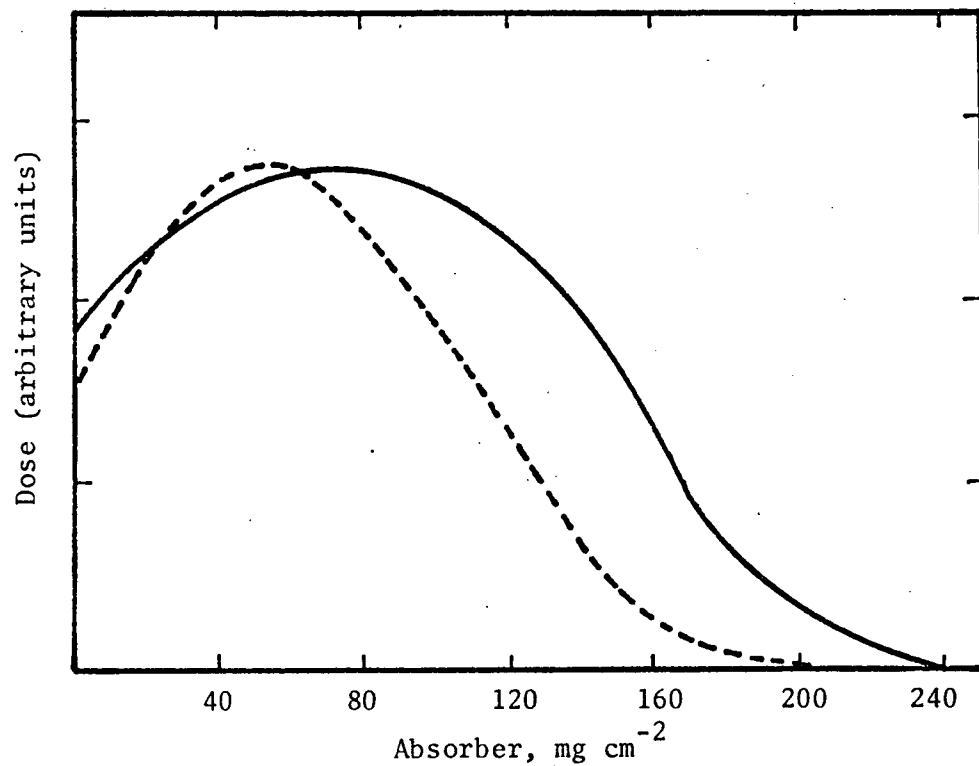
Fig. 1-4(a)
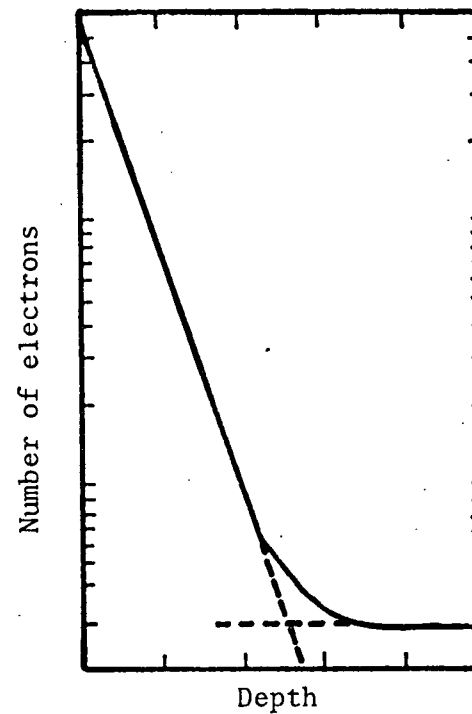
Fig. 1-4(b)

Figure 1-4(a)   Dose depth curves for 0.5 MeV electrons in water (solid line) and aluminum
(dotted line).   (b)   Typical transmission depth curve of high energy electron
through aluminum.

photons in order to conserve energy. Although theory predicts that these photons have a constant energy spectrum and thus extend into the visible region, because the low energy photon emission is masked by other light emission (see later) and does not contribute to significant energy loss, Bremsstrahlung is usually associated with X-ray production. The Bremsstrahlung cross-section increases with electron kinetic energy and the atomic number of the absorber, so that although unimportant for energies below 1 MeV in water, as shown by equation 1-5 (15), it becomes the dominant energy loss mechanism at high energies especially for the heavier elements.

$$X(E) = \frac{hZE}{1+hZE} \tag{1-5}$$

where $X(E)$ = the fraction of the incident electron kinetic energy converted to Brehmsstrahlung in the process of slowing down

$\quad h \quad = 3 \times 10^{-4}$

$\quad Z \quad =$ atomic number

$\quad E \quad =$ the electron kinetic energy (MeV)

However, because of the low cross-section for reabsorption of high energy photons, they have little ensuing radiation chemical effect compared to electrons.

(ii) Cerenkov Radiation

A high velocity charged particle will induce the emission of electromagnetic radiation from the area of its track due to the relaxation of electron induced polarization (recall the density effect) of the molecules immediately adjacent to this track. At

velocities less than the speed of light, there will be no observable
emission of photons since the radiated wavelets interfere destructively.
But when the velocity of the particle exceeds the phase velocity of
light in that medium, the wavelets along the track will be in phase,
so that photons will be observed emitted from the path of the charged
particle. The coherence condition (17) is illustrated by the Huygens
construction in figure 1-5.
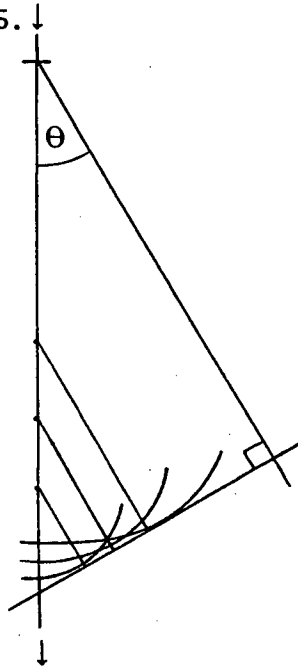
Figure 1-5

Using this simple geometrical argument, one can also show that
the Cerenkov radiation will be emitted at a specific angle to the track
of the charged particle, as given by equation (1-6).

$$\Theta = \cos^{-1}\frac{1}{\beta n} \qquad (1-6)$$

where β = v/c the ratio of the velocity of the
particle to the velocity of light

n = refractive index of the medium

Thus the Cerenkov emission will be emitted with azimuthal symmetry about the direction of the charged particle, the angle of emission a function of its kinetic energy. As well, the Cerenkov photons are linearly polarized with the electric vector E perpendicular to, and the magnetic vector H tangential to, the surface of the Cerenkov cone.

The first complete theoretical treatment of Cerenkov radiation was made by Frank and Tamm (18) in the framework of classical electrodynamics. Although subsequent work (19,20,21) has vastly expanded the theoretical basis of the Cerenkov effect, the results of Frank and Tamm have been left essentially unchanged for the purposes of this work. The fundamental Cerenkov equation for the energy radiated from the track of an electron travelling at a constant velocity in an unbounded, transparent, and isotropic dielectric is:

$$\frac{dW}{dl} = \frac{e^2}{c^2} \int_{\beta n > 1} \left(1 - \frac{1}{\beta^2 n^2} \right) \omega d\omega \qquad (1-7)$$

where $\frac{dW}{dl}$ = the energy loss due to Cerenkov emission, per unit path length

ω = the angular frequency of the emitted light

$\omega = \frac{2\pi c}{\lambda}$ (where λ = wavelength)

e = the electron charge

β = v/c, the ratio of the electron velocity to speed of light

n = the refractive index of the medium

In spite of the unrealizable physical conditions under which this equation was derived, agreement with experimental observations (16,17,22,23,24) on electrons in many different media is surprisingly good. By manipulating equation 1-7, changing from energy to photons, one may obtain the spectral dependence of the emitted radiation.

$$\frac{d^2N}{d\ell d\lambda} \propto \frac{1}{\lambda^2} \qquad (1-8)$$

where $\frac{d^2N}{d\ell d\lambda}$ = the number of photons per unit path and per unit wavelength interval

$\quad\quad\quad \lambda$ = wavelength

Thus, Cerenkov radiation has a continuous spectral distribution, rising sharply as the wavelength decreases, so that to the human eye Cerenkov radiation appears blue. Finally, by integrating equation (1-7) over all values of ω, one may estimate the contribution from Cerenkov radiation to the total energy loss of a fast ($\beta \sim 1$) electron. Using the approximate expression derived by Jelley (17), Cerenkov radiation comprises less than 0.1% of the total energy loss, so that even if Cerenkov photons cause photochemical effects in the medium, these effects would be negligible compared to excitations induced by a high energy electron.

(iii) Transition Radiation

When one considers a medium of finite extent in the theory of Cerenkov radiation, electromagnetic interactions at the boundary introduce a small contribution called Transition radiation to the

Cerenkov light emission (17). This effect arises whenever a charged particle traverses a region of dielectric inhomogeneity (either a sharp boundary or a continuous variation) and, although energy dependent, the emission intensity increases monotonically with energy; unlike Cerenkov radiation there is no energy threshold for Transition radiation. Because this is a very weak effect ($\sim$ 1 photon per 10^3 electrons) such emission has been observed (23,24,25) only in the most favourable conditions, such as the impact of electrons on metal foils in vacuum, where other competing effects are minimal. However, with the extremely high electron fluxes available from the Febetron accelerator (complete characteristics will be given later) Transition radiation could possibly be observable, since at the low electron energies in this work the angular distributions of Cerenkov radiation and Transition radiation are quite different.

(3) <u>Electron Penetration in Thick Absorbers</u>

The objective of transport theory calculations is the prediction of the electron flux distribution in an absorber as a function of space, energy and direction, starting from a monoenergetic electron beam of known geometry. From the distribution, one may then calculate the experimentally measurable dose-depth distribution in order to verify the proposed result. A theoretical description of the transport of high energy electrons in thick targets must simultaneously include contributions from all possible momentum changes and energy losses as the electron flux is attenuated in the absorber. There are two different approaches to this problem,

(i) the analytical formulation based on the Lewis

equation (26),

(ii) numerical Monte Carlo simulation (27).

Although the Monte Carlo technique can produce only numerical

data, it is superior to computations based on the Lewis equation

(29,30), simply because the Monte Carlo procedure can be readily

applied to real experimental conditions (28), where the analytical

formulation (i) breaks down because of the complex geometry. The

Monte Carlo method compares very well with experimental data, a

typical example (31) shown in figure 1-6, giving the transmitted

electron energy spectrum of 2.66 MeV electrons transmitted through a

0.254 g/cm^2 (0.15 electron range) aluminum target. In radiation

chemistry, and in particular pulse radiolysis, the spatial distribution

of absorbed dose is often inhomogeneous because of experimental

limitations (this is an acute problem in this work) and such effects

will affect the calculation of both yields and rate constants (second

order). These dose distributions, in many cases, are extremely

difficult to measure accurately, because they require in situ observation,

so that one must either change the experimental arrangement so that dose

homogeneity is achieved, or attempt to include an estimated inhomogeneity

in ones calculations. Hopefully, the high quality results now becoming

available from the Monte Carlo simulations using high speed computers

will assist such calculations.

(4) Heavy Particles

Although most radiation chemical studies use high energy

electrons and photons, other ionizing radiations, most commonly
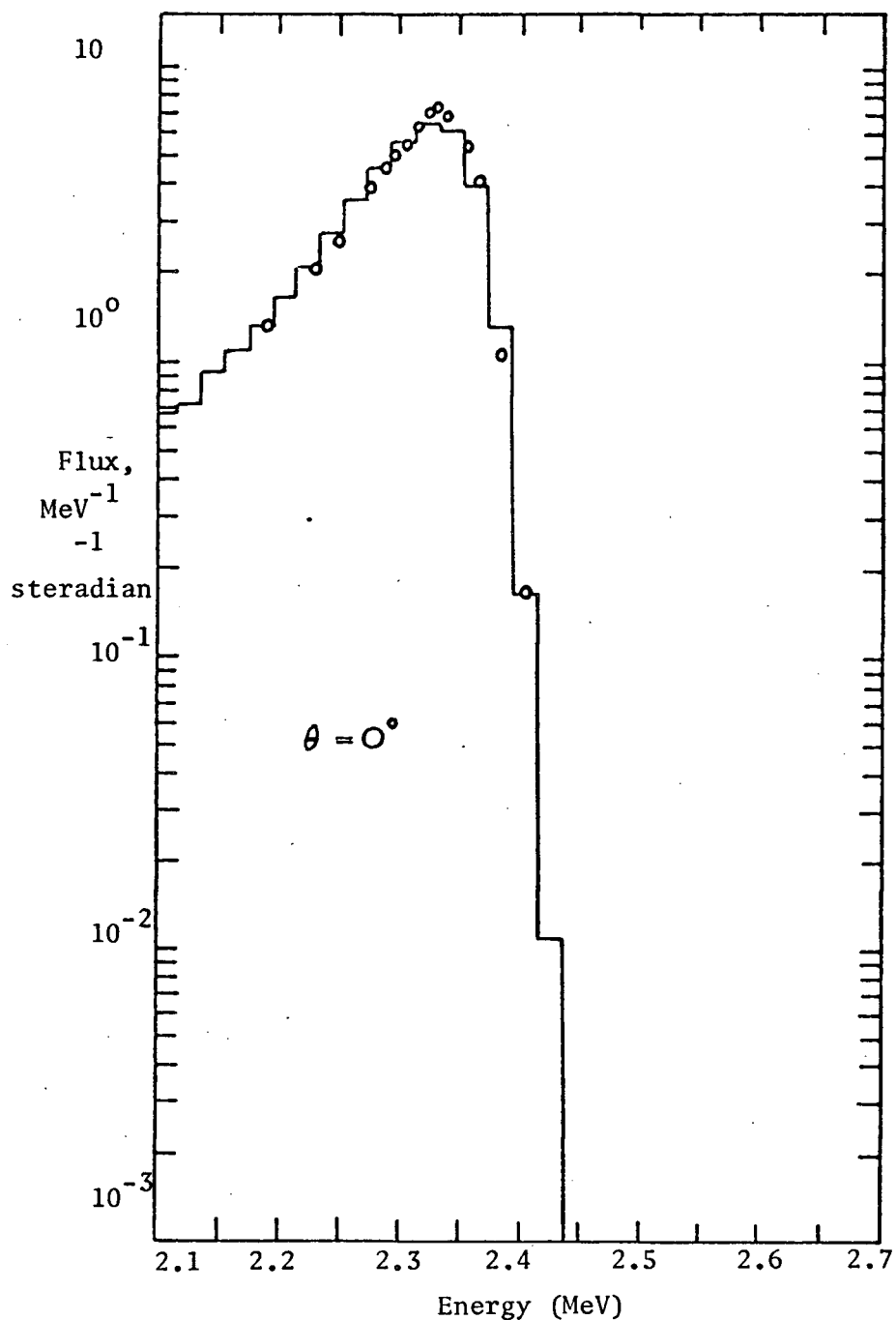
Fig. 1-6 Energy Spectrum of Transmitted Electrons (incident energy
2.66 MeV) emerging in the Forward Direction from Aluminum, 0.254 g cm
The points are experimentally measured and the histogram was
calculated from a Monte Carlo computer simulation.

α-particles, protons, and deuterons (but also including stripped nuclei and fission fragments), are sometimes employed because the very high rate of energy loss for these particles gives rise to a completely different spatial distribution of energy deposition. These effects are very important to a comprehensive theory of radiation chemistry, but are outside the scope of this work, so that a discussion of these generic effects will not be included.

(B) Early Events in Radiation Chemistry

So far, this discussion has centered around the macroscopic description of the energy loss mechanisms of the primary ionizing radiation as it is attenuated in matter, and the question of the effects of these energy losses on the absorber has been tacitly ignored. The dynamical details of this energy transfer on the molecular (or atomic) scale are the foundations of the theoretical framework of radiation chemistry. However, because these events have never been directly observed in situ, their characterization is consequently of a more qualitative nature. Nevertheless, such theories have been remarkably successful, within the scope of their validity, in predicting radiation chemical effects.

(1) Spatial Inhomogeneity

A high energy electron transfers its energy to an absorber in a series of random encounters with the electrons of the medium. Depending on the magnitude of this transfer, excitations or ionizations may occur, the area of this perturbation being called a spur. The cross-section for inelastic collisions predicts (32,33) that most of these energy losses will be greater than the molecular ionization potential (10-12 eV, although it is argued (34) that it could be as low

as 6 eV in condensed media for example water with an average energy
deposition of about 30 eV (36)). Thus within the time necessary for an
electronic transition ($\sim 10^{-16}$ seconds) molecules are ionized giving
positive ions and hot electrons in the region of the spur. These
ejected electrons range in kinetic energy from a few eV (the average
case) up to a significant fraction of the incident electron energy
for a hard collision. Such high energy secondary electrons are called
δ-rays and produce branch tracks along the path of the primary high
energy electron. The average spatial distribution of spurs along the
particle track can be estimated from the average rate of energy
loss of linear energy transfer (LET) of the incident electron, as
given by the Bethe equation. High energy electrons (0.5 MeV-50 MeV,
thus including ^{60}Co γ-rays) with an average energy loss of ~ 0.2 eV nm^{-1},
corresponding to a spur separation of ~ 100 nm, are classified as low
LET radiation, while in contrast high LET radiation such as 10 MeV
α-particles deposits ~ 100 eV nm^{-1}. However, as the high energy
electrons are slowed down, their LET also rises significantly (see
figure 1-3) so that for 10 keV electrons the LET is ~ 2 eV nm^{-1} (spur
separation ~ 10 nm), and at even lower energies, the spurs along the
track will completely overlap. Because of the considerably different
radiation chemical effects over this range of energy densities the
following categories of energy-dependent track entities have been
proposed (35).

 (a) Spurs are the product of small energy transfers,
   less than 100 eV, such that the ejected electrons
   have insufficient energy to cause further ionization.

(b) <u>Blobs</u> are extra large spurs which occur when a

secondary electron is produced with enough energy to

cause further ionization, but insufficient energy to

escape the region of its parent ion (100 eV < E < 500 eV).

(c) <u>Short tracks</u> result from secondary electrons which

are energetic enough to escape from the area of

their concomitant positive ion but whose LET is so

high that the spurs along its track overlap (500 eV

< E < 5000 eV).

Because of the different δ-ray spectra and LET for high and low

energy electrons, the relative energy partition between these

different track entities will be a function of the incident electron

energy. The calculated proportions (35) of these generic effects is

shown in figure 1-7 and illustrates the significant changes in the

spatial distribution of energy deposition between high and low

electron energies.

(2) The Physicochemical Stage

Having established the initial spatial inhomogeneity of primary

radiation chemical events, the next question is the fate of the

extremely unstable ionization products, free electrons of several

eV kinetic energy (called sub-excitation electrons, since their

energy is below electronic transition energies) and their concomitant

positive ions (such as H_2O^+ in water). The crux of this problem lies

in the ultimate probability of neutralization between these stationary

positive ions and free electrons, once the highly energetic sub-excitation

electrons have been sufficiently slowed down (to thermal energies
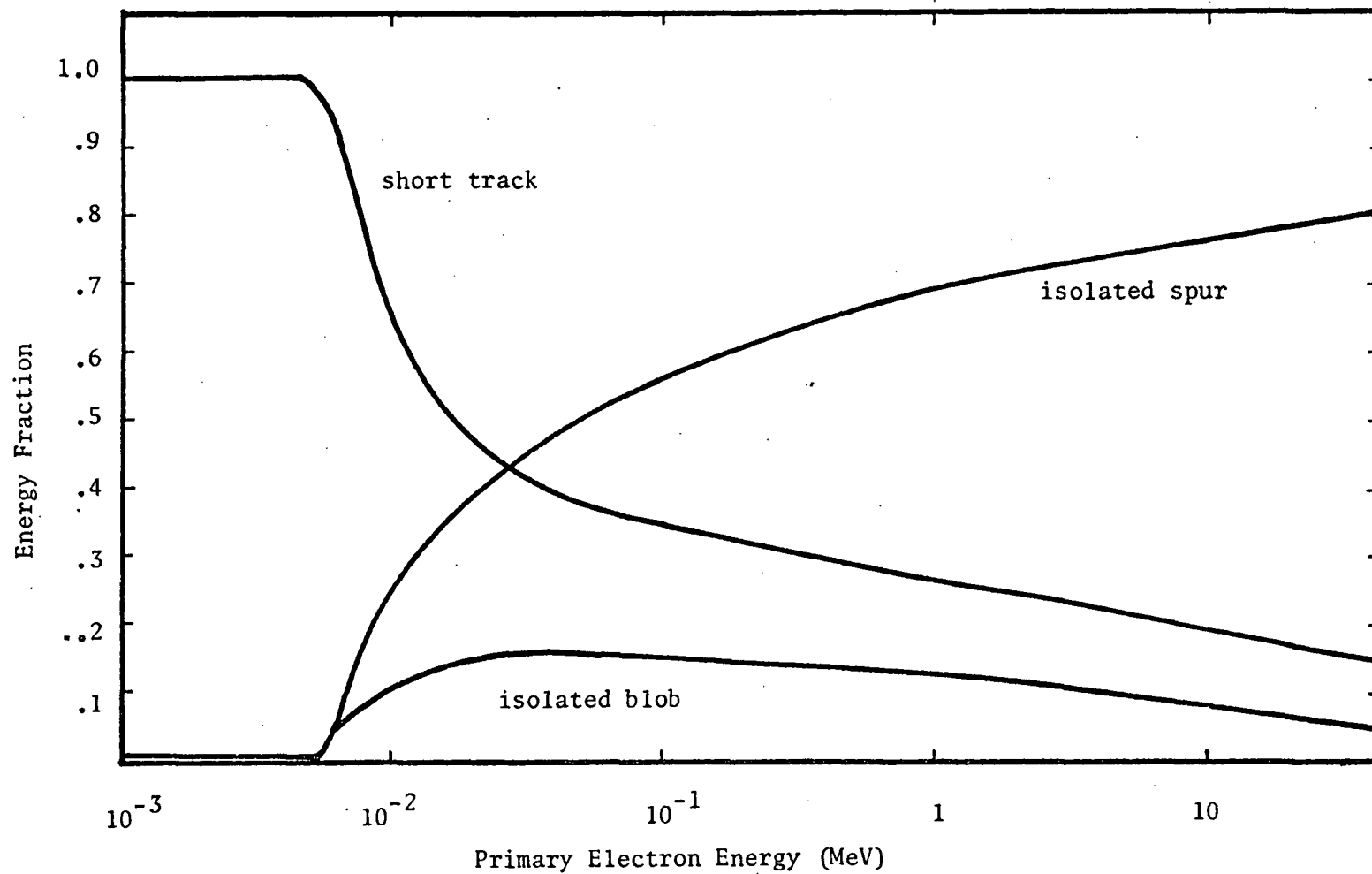
Figure 1-7 Relative energy deposition between spurs, blobs and short tracks as a function of primary electron energy.

$\sim$ 50 meV) by the medium so that they can react. Thus, the determining factor will be the relative magnitudes of the attractive Coulomb potential from positive ions (not necessarily the parent ion) compared to the kinetic energy of the sub-excitation electrons as they dissipate their excess energy in the medium. At this point, one must introduce some of the physical characteristics of the absorbing material.

In non-polar liquids, the sub-excitation electron at first rapidly loses energy ($\sim 10^{13}$ eV sec^{-1}) to intramolecular vibrations until its kinetic energy is ~ 0.5 eV. Further energy dissipation leading to thermalization is then thought to occur through intermolecular vibrations (37), resulting in a large displacement (~ 10 nm) from the positive ion because of the small cross-section for this type of energy loss. However in spite of the distance that these electrons travel, most of them are quickly recaptured by their parent ion, due to the high permittivity of these liquids. Those electrons that do escape geminate recombination will in the absence of other reactions also eventually recombine with a positive ion, the physical nature of these electrons and their kinetic behaviour being a matter of some conjecture (38).

In higher dielectric constant liquids (static dielectric constant $\varepsilon_o > 10$), once the sub-excitation electrons have been reduced to sub-vibrational energies, the final of pattern energy dissipation is completely different. Because of the dipolar nature of the medium, the sub-vibrational electrons continue to experience rapid energy loss through induced rotations of the solvent molecules, thus leading to fast thermalization of the electron ($\sim 10^{-13}$ seconds (39)). The average

distance the electron escapes from the positive ion during
thermalization is a matter of some considerable controversy; for water
this distance ranges from $\sim$ 2 nm for the Samuel-Magee model (40) to
$\sim$ 10 nm for the Lea-Gray-Platzman formulation, depending on how much
elastic scattering increases the path of the sub-vibrational electron.
Very few a priori estimates of electron thermalization and escape
parameters have been made for other liquids.

Before considering further events in the adventures of the
thermalized electron, one ought to return to the positive ion. Polar
aprotic liquids will be similar to non-polar solvents, in that on this
time scale, the positive ion is essentially an unreactive entity.
However, in polar solvents with labile protons, very rapid ion molecule
reactions of the form:

$$ROH^+ + ROH \longrightarrow ROH_2^+ + RO \cdot \tag{1}$$

that is for water,

$$H_2O^+ + H_2O \longrightarrow H_3O^+ + \cdot OH \tag{2}$$
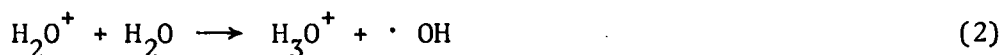
can take place in $\sim 10^{-14}$ sec (32). This type of transformation may
significantly affect the reactivity of the positive ion with respect
to the electron, because this positive ion has become a stable,
closed electron shell chemical species, whereas in non-polar and
polar aprotic solvents the positive ion remains a highly unstable
electrophilic ion.

In dielectric liquids the range of the coulombic potential from
the positive ion is significantly diminished by the low dielectric

permittivity of the medium. Thus in those compounds, a significant

fraction of the secondary electrons undergoing thermalization escape

geminate recombination to survive as free electrons. Simultaneously

with final thermalization, in polar compounds such as water or the

alcohols, these free electrons are rapidly stabilized ($\sim 10^{-12}$

seconds (4c)) in a self-induced potential well of solvent molecules,

to produce a stable chemical species of unit negative charge, called

the solvated electron. This solvation process occurs rather than

reaction with the solvent, because for these saturated molecules

the only reaction mechanism, dissociative attachment, requires a

significantly longer time scale than solvation. Polar aprotic

liquids, which might also be expected to solvate electrons, are not

completely understood in this regard. Some compounds, such as the

amines and hexamethylphosphoramide stabilize solvated electrons very

well, while other more polar unsaturated compounds such as formamide

(a subject of part of this investigation), dimethylsulphoxide, or

acetonitrile are still a quandary. In view of recent picosecond

time scale experiments (4d) solvated electrons are unlikely to be observed

in unsaturated compounds because of rapid solvent scavenging of the

thermalized electrons, a possible mechanism on this time scale since

these compounds have vacant low lying molecular orbitals in which

to accept the free electron.

The geminate recombination of free electrons and the primary

positive ions will produce excited molecules with substantial excess

energy. These species will likely rapidly decompose before they can

dissipate this energy to the medium, thus producing several neutral

radical fragments within the spur. In water, by analogy with vacuum U.V. gas phase data, these species (equation (3))

$$H_2O^* \rightarrow H \cdot + \cdot OH \tag{3}$$

will be a hydrogen atom and a hydroxyl radical. This effect is usually relatively minor in polar compounds, but in non-polar media where there is significant geminate recombination it will be an important process.

Throughout this discussion, the effects of larger extra-spur entities such as blobs and short tracks have been ignored. In these cases, due to a much higher density of energy deposition there will be regions of plural ionization and hence an even higher geminate recombination probability because of the multiple charged positive core of these areas. Thus, as the LET of the primary radiation increases (see fig. 1-7), the initial yield of neutral species from geminate recombination as compared to charged species from electron escape, also increases, resulting in significant variations in radiation chemical yields for different LET radiations.

(3) Chemical Stage

At this juncture, the primary chemical species have been formed in the spur, and sufficient time has elapsed ($\sim 10^{-12}$ seconds) so that diffusion can occur and therefore the chemical reactivity of these entities must now be considered. In liquid water (to which the ensuing discussion will be primarily directed because of its extensive study) the spatial distribution[*] of primary species in an average spur consists

_____

[*] This model is essentially of the Lea-Gray-Platzman type (39), modified to include a small hydrogen atom yield.

of two concentric regions, a small inner core (radius $\sim$ 1 nm) comprising hydronium ions, hydroxyl radicals, and possibly hydrogen atoms and beyond this hydrated electrons randomly distributed within an outer radius of $\sim$ 10 nm. The population and size of the spur will naturally depend on the magnitude of the primary energy deposition, so that in blobs and short tracks there will be extended regions of high initial radical density. The experimental determination of the average 100 eV yield of these primary species will give significantly different results depending on how it is carried out. That is, because of their initial close proximity and high reactiviy, a significant proportion of these spur entities will have diffused together and reacted within the experimental time resolution of one's measurement. Thus, data from microsecond pulse radiolysis and ^{60}Co γ-radiolysis experiments at low ($\sim$ 10^{-3} molar) scavenger concentrations, extrapolated to zero solute concentration gives the following results ((41), using the nomenclature (42) of a small g for primary yields and a capital G for observed product yields):

$$g(e_{aq}^-) = 2.7 \qquad g(H_3O^+) = 2.8$$
$$g(OH) = 2.75 \qquad g(OH^-) = 0.1$$
$$g(H) = 0.55$$

and will include the following products formed in rapid intraspur reactions (the molecular yield):

$$g(H_2O_2) = 0.7$$
$$g(H_2) = 0.45$$

In addition the rate constants for the reactions of these primary species, which are implicitly related to their experimentally measured yields, are summarized in Table II. In contrast, by using very high scavenger concentrations ($\sim$ 1 molar), in order to suppress intraspur reactions, one can, in principle, extrapolate to infinite solute concentrations and thus estimate the primary radiation chemical yield of electrons in the spur (43) g^o (e_{aq}) = 4.8, as compared to g (e_{aq}) = 2.7 (see above). These two very different yields reflect the inhomogeneous nature of energy deposition from ionizing radiation. The primary chemical species rapidly formed in the spur in physicochemical events, on the time scale of the chemical stage begin to diffuse (in random directions) resulting in a net flux of these reactive species into the bulk of the medium, some reacting with their sibling radicals (intraspur reactions) in the process, others escaping to survive into a final kinetically homogeneous (interspur overlap is now complete) process of mutual annihilation. The relative proportions of these inter- and intra-spur reactions will depend on the initial radical density. Therefore one would expect the radiation chemistry of high and low LET radiations to be significantly different. A quantitative discussion of these effects requires the use of phenomenological spur diffusion models, taking into account the initial radiation chemical yield and spatial distribution of the primary species of all generic entities (spurs, blobs, short tracks, etc.) combined with a mathematical formulation of their subsequent diffusion and reaction (with themselves or other solutes). Unfortunately all spur diffusion models are a posteriori calculations, in that they

Table II

Rate Constants for the Reaction of Primary Species in the Radiolysis of Water

	Reaction	pH	Rate Constant
(4)	$e_{aq}^- + e_{aq}^- \rightarrow H_2 + 2\,OH_{aq}^-$	> 14	$k = 5.5 \cdot 10^9\ M^{-1}\ sec^{-1}$
(5)	$e_{aq}^- + OH \rightarrow OH_{aq}^-$	10.5	$k = 3.0 \cdot 10^{10}\ M^{-1}\ sec^{-1}$
(6)	$e_{aq}^- + H \rightarrow H_2 + OH_{aq}^-$	10.5	$k = 2.5 \cdot 10^{10}\ M^{-1}\ sec^{-1}$
(7)	$e_{aq}^- + H_2O_2 \rightarrow OH + OH_{aq}^-$	7	$k = 1.23 \cdot 10^{10}\ M^{-1}\ sec^{-1}$
(8)	$e_{aq}^- + H_3O^+ \rightarrow H + H_2O$	4.5	$k = 2.32 \cdot 10^{10}\ M^{-1}\ sec^{-1}$
(9)	$H + H \rightarrow H_2$	2	$k = 1.0 \cdot 10^{10}\ M^{-1}\ sec^{-1}$
(10)	$H + OH \rightarrow H_2O$	acid	$k = 1.2 \cdot 10^{10}\ M^{-1}\ sec^{-1}$
		7	$= 7.0 \times 10^9\ M^{-1}\ sec^{-1}$
(11)	$OH + OH \rightarrow H_2O_2$	7	$k = 5.0 \cdot 10^9\ M^{-1}\ sec^{-1}$
(12)	$e_{aq}^- + H_2O \rightarrow H + OH^-$	8.4	$k = 16\ M^{-1}\ sec^{-1}$
(13)	$H + OH^- \rightarrow e_{aq}^-$	> 11	$k = 2.7 \times 10^7\ M^{-1}\ sec^{-1}$
(14)	$OH + H_2 \rightarrow H + H_2O$	7	$k = 6 \times 10^7\ M^{-1}\ sec^{-1}$
		13	$= 1.6 \times 10^8\ M^{-1}\ sec$

must use long time scale measurements to estimate the initial physico-chemical dimensions of the energy deposition; and in spite of their success (44) in rationalizing many radiation chemical observations they can never yield definitive conclusions about early events.

(C) The Chemical Scale of Events Following the Primary Transfer of Energy from Ionizing Radiation

Having formulated some general principles characterizing the primary energy deposition and the ensuing events leading to a radiation-induced chemical change, it remains to describe, for the specific media of interest to these studies, the chemical and physical properties of the species which survive the physicochemical stage, and thus account for experimentally observable radiation chemical effects.

(1) Water

The best understood and by far the most extensively documented radiation chemical investigations on polar liquids have been in water, the results of which serve both as a comprehensive test of radiation chemical theories, and as a basis for analogous interpretations of other polar systems. At the temporal stage where intraspur reactions are essentially complete, the net chemical change may be expressed by equation (15).

$$H_2O \rightsquigarrow e_{aq}^-, \; H_3O^+, \; OH, \; H, \; H_2O_2, \; H_2, \; OH_{aq}^- \tag{15}$$
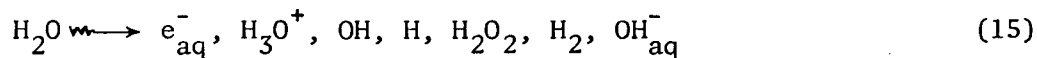
with the primary yields of these species (41)(as in previous section),

$$g(e_{aq}^{-}) = 2.7 \qquad\qquad g(OH) = 2.75$$

$$g(H) = 0.55$$

$$g(H_3O^+) = 2.8 \qquad\qquad g(OH^-) = 0.1$$

$$g(H_2O_2) = 0.7 \qquad\qquad g(H_2) = 0.45$$

and reaction rate constants summarized in Table II. These data are derived primarily from direct physical measurements using pulse radiolysis techniques as well as chemical product analysis where necessary (i.e. for the molecular yield of H_2O_2 and H_2). The concentrations normally achieved in radiation chemistry are quite low (10^{-9} M - 10^{-5} M in most cases), so that despite the high reactivity of the three radical entities (H, OH, e_{aq}^{-}) with themselves and the other primary products, their lifetimes are relatively long, and thus it has been possible to investigate their physical properties and chemical reactivity over a very extensive range, using a variety of physical techniques.

(a) The Hydrated Electron

The existence of an excess electron stabilized in a liquid medium, with all the properties of a normal solvated negative ion, is a rather difficult notion to accept on first sight. Yet the experimental evidence accumulated over the last decade rules definitively in favour of this concept. The hydrated electron is a very mobile species, the diffusion constant determined by pulse radiolysis conductivity experiments (45) being 4.5×10^{-5} cm^2 sec^{-1}, implying that the activation energy for its very fast reactions will be small $\sim 3 - 4$ kcal mole^{-1}, corresponding to the activation energy for the self-diffusion of water. Moreover, ionic strength effects on hydrated electron reaction rate constants show quite clearly that e_{aq}^{-} has unit negative charge (46,47). As well, the existence

of an unassociated free electron is unequivocably demonstrated
by electron paramagnetic resonance (EPR) measurement on liquid water
(48a), in which a single, very narrow (< 0.5 gauss) line is observed at
g = 2.002 ± .0002, confirming the assertion that the hydrated electron
exists as an unassociated species, its interaction with the surrounding
protons of the medium being of a very transitory nature so that no
hyperfine splitting is observed.

The hydrated electron (and solvated electrons in general) has a
very intense optical absorption spectrum ($\epsilon \sim 10^4$ M^{-1} cm^{-1} at the
wavelength of maximum absorption), extending from the near infrared to
the ultra-violet. The absorption spectrum has been the most useful
physical property for the investigation of its chemical reactivity,
because of the extremely low concentrations of hydrated electrons which
can be experimentally observed (as low as 10^{-9} M) with such a high
extinction coefficient. The physical mechanism giving rise to the
hydrated electron absorption spectrum is still a contentious subject,
since the explanation of its origin must be based on a structural model
for the species itself.

Qualitatively, the position of the absorption spectrum and its
modifications, to lower energies with increasing temperature (49) and
to higher energies with increasing pressure (50) and the addition of
certain solutes (51), can be readily explained in terms of an electron
trapped in a solvent cavity deriving its stability from self-induced

polarization of the surrounding medium. However, more detailed and quantitative formulations of electron stabilisation have not added as much to the physical understanding of important features of the absorption spectrum, or mobility and thermodynamic properties of e_{aq}^{-}, as one might have expected, although hydrated electrons in particular have enjoyed an ever increasing amount of theoretical interest from their first discovery.

The absorption spectrum of e_{aq}^{-} must arise from electronic (and other ?) transitions within the potential well, but to what extent the broad, structureless and energy-asymmetric band is governed by the nature of the transition, or the solvent molecules which constitute the physical trap, is still not clear. The transition at λ_{max} could be assigned to an excitation to a bound state, similar to the 2p ← 1s transition in the H atom case, or to non-bound states for instance an exciton continuum or possibly complete photoionisation. In addition, the typical broadness and asymmetry that typifies all e_{s}^{-} absorption bands could arise from statistical variations in the population of traps of a given depth depending on such variables as dielectric properties and liquid structure. The possible origins of the absorption spectrum have been discussed in these terms including thermodynamic considerations in references (52) and (53). Many attempts to incorporate these dependencies in quantum mechanical treatments of these species have now been published, the first comprehensive calculations being performed by Jortner (54) in 1964 who developed his ideas within the concept of a polaron in a continuous dielectric medium (55,56). These calculations, in which the e_{s}^{-} was treated as a charge delocalized in a spherical

cavity within a liquid dielectric continuum for ammonia and water, established
the tendency to regard the energy of λ_{max} as due to a 2p ← 1s type
transition, that is to a bound excited state. The results of these
calculations were impressive in the case of the ammoniated electron
but only moderately successful in predicting the λ_{max}, temperature
dependence, the oscillator strength and the cavity size of the hydrated
electron. Further theoretical studies along this approach for the
excess electrons in alcohols as well as e_{aq}^- (57)
have been reported with fair agreement between predicted and observed
values for the above mentioned variables. Later treatments of this
problem have envisaged the cavity as structured in terms of spherical
(58) or tetrahedral (59) order of solvent dipoles, while recent molecular
orbital calculations (60) have extended earlier notions of discrete
species such as H_2O^- or $(H_2O)_2^-$, (61). However all of these models suffer
from the deficiency in our understanding of the dynamical aspects of the
microscopic electron-solvent interactions giving rise to electron
stabilization.

It is noteworthy that in all of these calculations on the hydrated
electron absorption spectrum, the transition at λ_{max} is implicitly
assumed to be a 1s - 2p type transition that is to a bound excited
state, although there is no conclusive evidence for either a bound or
non-bound excited state, at the present time. Recently however, experiments
were reported (62) from which the lifetime of the excited state of
e_{aq}^- was calculated to be less than six picoseconds. From these
results it has been inferred that photoexcitation of e_{aq}^- is in fact
a photoionisation, presumably followed by rapid resolvation of the free

electron, although the possibility of very fast de-excitation to the lower state again can not be ruled out.   Since the experiments were performed at one wavelength only the question of the distribution of traps is still open, but any future experiments on this problem will inevitably be hampered by the limiting time scale.

The hydrated electron is the predominant reducing species produced in the radiolysis of liquid water, reacting rapidly by either direct attachment or dissociative attachment mechanisms with any solute containing an available low energy molecular orbital to accommodate it. Moreover, it is possible to correlate its nucleophilic reactivity with series of organic solutes, for instance carbonyl compounds, by means of the Taft σ^* parameter (63). The hydrogen atom and the hydrated electron are closely related chemically, in fact constituting a conjugate acid-base pair, the latter being the basic and more strongly reducing species, hence their chemical interconvertability by the following reactions:

$$H_3O^+ + e^-_{aq} \longrightarrow H + H_2O \tag{8}$$

$$H + OH^- \longrightarrow e^-_{aq} \tag{13}$$

$$k_8 = 2.3 \times 10^{10} \, M^{-1} \, sec^{-1}, \quad k_{13} = 2.7 \times 10^7 \, M^{-1} \, sec^{-1}$$

Therefore, by appropriate adjustment of the pH, either the hydrated electron or the hydrogen atom may be obtained as the dominant species.

(b) The Hydrogen Atom

Hydrogen atoms are also a primary reducing species produced in the radiolysis of water. Although EPR observations of H atoms in aqueous solution have been recently reported (48b), most studies of their yield and reactivity are of a less direct nature, since as yet no optical spectrum has been observed for this species in liquid water. The reactivity of the hydrogen atom is different from that of the hydrated electron although both are reducing species. As well as participating in reductive attachment reactions (in general with a lower rate constant than e_{aq}^{-}), the hydrogen atom reacts with saturated organic compounds by α - carbon hydrogen abstraction, thus demonstrating more typical radical characteristics than the hydrated electron.

(c) The Hydroxyl Radical

The hydroxyl radical is the concomitant primary oxidizing species in water resulting from the reaction of the unstable positive ion H_2O^+ with another water molecule to give $\cdot OH$ and H^+ (H_3O^+) as in reaction (2)

$$H_2O^+ + H_2O \longrightarrow H_3O^+ + \cdot OH \qquad (2)$$
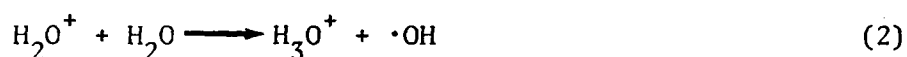
As well as exhibiting the typical electron transfer oxidation reactions, this radical also adds to unsaturated centers in organic molecules and participates in hydrogen atom abstraction reactions. Thus, reaction with H_2 converts OH to H (equation 14), which can be converted to solvated electrons by OH^- (equation (13)),

$$OH^{\cdot} + H_2 \longrightarrow H_2O + H \qquad (14)$$

$$H + OH^- \longrightarrow e_{aq}^- \qquad (13)$$

$k_{13} = 2.7 \times 10^7 \ M^{-1} \ sec^{-1} \qquad k_{14} \sim 10^8 \ M^{-1} \ sec^{-1}$

so that with suitable concentrations of H_2 and OH^- hydrated electrons may be obtained, to the exclusion of all other reactive radical species. A weak absorption due to the hydroxyl radical is observed in the ultraviolet between 200 nm and 300 nm (64). However direct physical measurements using this absorption are only possible under experimental conditions where the hydrated electron, which still has a significant absorbance at these wavelengths, is eliminated using a suitable scavenger.

(2) Alcohols

Although not nearly as fully documented as liquid water, the aliphatic alcohols (thus excluding allyl alcohol) show very similar radiation chemical effects. The solvated electron is formed with substantial yields g $(e^-_{solv}) \sim 1.0$ (65) and has an absorption spectrum spanning the visible and infra-red; the wavelengths of maximum absorption range from 500 nm to 900 nm. It is noteworthy that solvated electron rate constants are very similar to those observed in water, a comparison is shown in Table III (66).

Table III

Solvated Electron Rate Constants in Different Solvents at $23^{\circ}C$.

Reaction	(k x 10^{-10} M^{-1} sec^{-1})		
	H_2O	CH_3OH	C_2H_5OH
e^-_s + H^+	2.3 + 0.2	3.9 + 0.9	2.0 + 0.4
e^-_s + O_2	2.0 + 0.2	1.9 + 0.4	1.9 + 0.3
e^-_s + $C_6H_5CH_2Cl$	0.55 + 0.15	0.50 + 0.12	0.51 + 0.12
e^-_s + anthracene	0.54 + 0.15	–	0.54 + 0.05

The analogous species to the hydroxyl radical in water, the alkoxyl radical RO˙, has not been unambiguously identified, however a transient absorption in the near ultra-violet has been attributed to it, (67,68) but not studied in any detail. No complete mechanistic analysis of the radiolysis of alcohols similar to that available for water has yet been carried out. Nevertheless, apart from the discovery of a few more possible radical species, it is not expected that significant deviations from this framework will be revealed.

CHAPTER II

A PREVIEW OF THE PULSE RADIOLYSIS STUDIES

DESCRIBED IN THIS THESIS

The original objective of this work was the investigation of light emission from pulse irradiated liquids as a direct means of studying primary radiation chemical processes, with particular reference to the radiolysis of water. Along with the conclusion that in the liquid state of water any such luminescence is insignificant ($G \leqslant 10^{-3}$) came the observation of a very strong reabsorption of the Cerenkov radiation from the primary high energy electrons by the high concentrations of hydrated electrons which are produced at the enormous dose-rates (peak dose-rate $\sim 1.8 \times 10^{28}$ eV cm^{-2} sec^{-1}) used in this work. Although such reabsorption has been suggested previously to explain the deviation from the expected Cerenkov emission spectrum in high dose-rate pulse radiolysis studies (69), only at the very high dose rates used in this work does the intrinsic temporal capability of this type of observation become apparent. Such measurements, rather than being simply a technical innovation for pulse radiolysis studies using low energy electron accelerators, are an extension of pulse radiolysis time resolution to the subnanosecond time scale using nanosecond techniques. As an illustration of this subnanosecond capability, the hydrated electron absorption spectrum can be clearly observed in 2 molar HClO$_4$ (see figure 5-7),

where recent studies (4c) show a lifetime for this species in the order of 30 picoseconds. The quantitative evaluation of Cerenkov reabsorption may be made spectrographically or spectrophotometrically, the choice being based on experimental considerations. A critical factor in such measurements is the Cerenkov radiation intensity, which would be transmitted if there was no reabsorption by radiolytically produced species. Thus 100% transmittance of Cerenkov radiation, designated reference Cerenkov for brevity, can be readily obtained in the visible region either by chemical scavenging of the absorbing species or by extrapolation from a compound showing no reabsorption of the Cerenkov light. A complete theoretical analysis, in terms of the physical parameters determining the magnitude of the reabsorption, has been carried out, the experimentally observed absorbance showing the following functional relationship:

$$U = f(D_r(t), G, \epsilon, k_1) \qquad (2-1)$$

where   U = observed absorbance

$D_r(t)$ = the dose rate function

G = the 100 eV yield of absorbing species

ϵ = the extinction coefficient of the absorbing species

k_1 = a pseudo-first-order decay constant for the absorbing species.

Having demonstrated the validity of the Cerenkov reabsorption technique, a series of experiments along the lines of the recently reported picosecond pulse radiolysis (4c,4d), with the purpose of both comparison and further

extension of the short time scale effects observed in this work, were initiated. Although lacking the intrinsic time resolution and kinetic insight of the stroboscopic picosecond pulse radiolysis technique, these Cerenkov reabsorption measurements were entirely consistent with the previously reported results, demonstrating substantial quantitative agreement where comparisons could be made.

In summary, this thesis described the characterization and the experimental development of a novel pulse radiolysis technique, Cerenkov reabsorption spectroscopy, by which subnanosecond kinetic observations can be attained, using existing nanosecond pulse radiolysis technology. There is one experimental requirement for the previous statement which should be explicitly indicated. Without a sufficiently high dose-rate, this subnanosecond temporal scale cannot be achieved, because the magnitude of the reabsorption decreases very rapidly to an experimentally undetectable level for lower dose-rates. Thus, in practice, these studies are specifically limited to very high current electron accelerators such as the Febetron series (70), that operate on the field emission principle.

CHAPTER III

EXPERIMENTAL DETAILS

The pulse radiolysis equipment to be described in this chapter
constitutes a novel and somewhat radical departure from any other
pulse radiolysis apparatus in use at the beginning of this work. In
fact, such a statement is equally as valid at present, since no other
laboratories have reported the use of the 600 keV Febetron accelerator
for liquid phase pulse radiolysis. Consequently, a somewhat detailed
description of the techniques developed in this research will be given
here.

(A) The Febetron Accelerator

The heart of this pulse radiolysis facility is the Febetron
accelerator (Model 730/2667, manufactured by Field Emission Corporation,
McMinnville, Oregon). This accelerator produces an extremely short, high
intensity electron pulse of nominal energy $\sim$ 0.5 MeV. The machine
used in this work is unique, since it is a model 701 (pulse length
$\sim$ 30 nanoseconds) modified with the model 2667 pulse shortener to deliver
a 3 nanosecond pulse (Field Emission now produces a 3 nanosecond version
without the 30 nanosecond option as the model 706/2667). The very short,
high intensity pulse is generated in the following three steps:

(a) The discharge of a Marx Surge network to produce a

600 kV, 30 nanosecond pulse.

(b) Shortening of the 30 nanosecond pulse to 3 nanoseconds but maintaining $\sim$ 600 kV amplitude.

(c) Application of this $\sim$ 600 kV, 3 nanosecond pulse to the cathode of a field emission tube to produce the electron pulse. The total energy output in this pulse is 10 joules, with a peak beam current of 5000 amperes.

The accelerating pulse may be measured by substituting an impedance matched resistive load (containing a copper sulphate solution) for the electron tube and observing the voltage drop to ground as a function of time. A typical waveform (70) is shown in figure 3-1(a). Next, the actual electron flux as a function of time may be obtained using a Faraday cup. Particular care must be taken in Faraday cup design for measurements on this time scale, since the geometry of the charge collector influences the pulse shape observed. Best results were obtained using the model 1653 (Field Emission Corporation) Faraday cup, the design of which is shown in figure 3-1(b). It should be noted that no current viewing resistor is used, because, according to Field Emission engineers (71), the collector looks like 50Ω to the high energy electrons and therefore is attached directly to a 50Ω cable (RG9/U) terminated in 50Ω at the oscilloscope. Unfortunately, this design requires a small collection aperture (0.5 mm diameter), so that the current waveform shown in figure 3-1(c) can be used only as a measure of the pulse duration, and not the total charge output of the accelerator. Another Faraday cup with a wider aperture and cylindrical collector which could have been used to estimate the total charge output,

Fig. 3-1(a)

Tektronix 519   10 nanoseconds/div
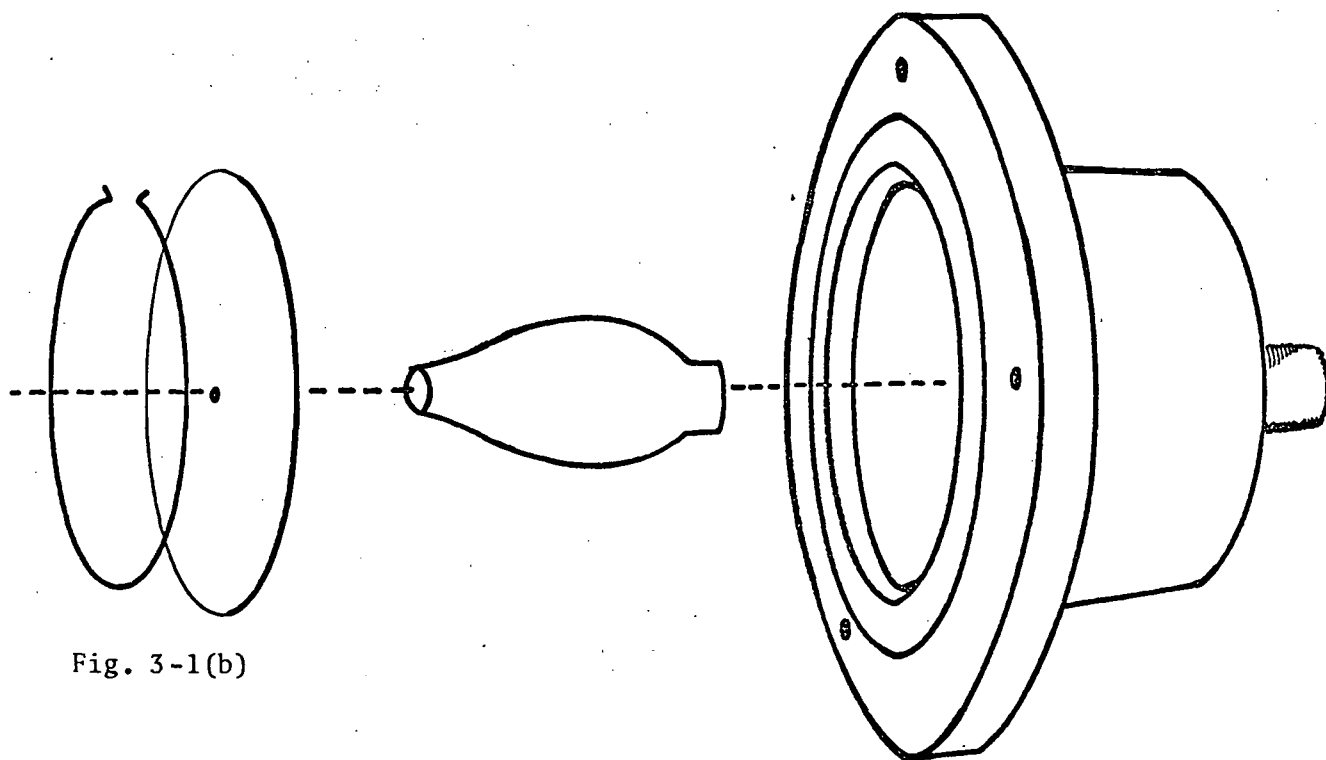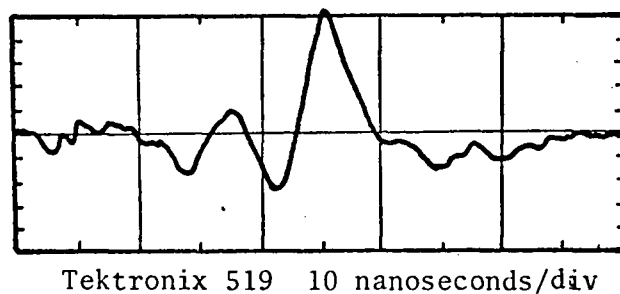
Fig. 3-1(b)

Hewlett Packard 183A
1 nanosecond/div
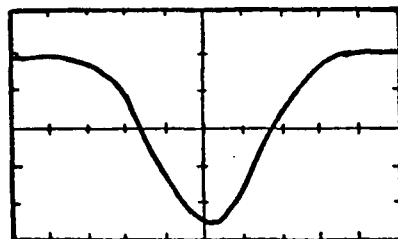
Tektronix 519
2 nanoseconds/div

Fig. 3-1(c)
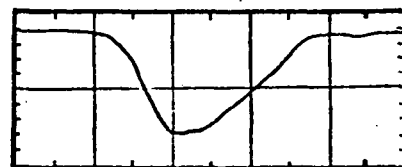
Figure 3-1(a)   Tracing of typical accelerating pulse from resistive load.
    3-1(b)   Diagram   of Model 1653 Faraday Cup, exploded view.
    3-1(c)   Tracings of Faraday Cup Waveforms.

yielded pulses of the order of 6 nanoseconds width at half height, far
in excess of those measured with the model 1653 Faraday cup, thus
illustrating the distortion which can occur.

From the shape of the accelerating pulse in 3-1(a), it is clear that
the Febetron does not produce a monoenergetic electron beam; however
to determine the exact form of the electron energy spectrum is a very
difficult proposition, since this waveform must be multiplied by the
time-dependent electron flux. Such an operation is impossible to perform,
because the superposition of figures 3-1(a) and 3-1(c) is uncertain.
A better approach is to make use of the fact that the field emission tube
is thought (2) to show constant impedance during the pulse.
This means that:

$$E(t) = I(t).Z$$

where Z = impedance of the tube

$I(t)$ = the electron flux as measured by the Faraday cup

$E(t)$ = the accelerating waveform

Thus one may obtain the approximate energy spectrum shown in
figure 3-2, by plotting the product of the mean electron energy in
a given time interval and the total charge in that interval.
Although there are significant numbers of low energy electrons,
the effective beam energy is approximately 0.5 MeV. The same number
is published (70) by Field Emission Corporation, estimated from both
the extrapolated electron range of depth dose profiles in aluminum,
as shown in figure 3-3 and from the mean electron energy obtained
by dividing the total dose per pulse (from calorimetric measurements)
by the total charge per pulse.
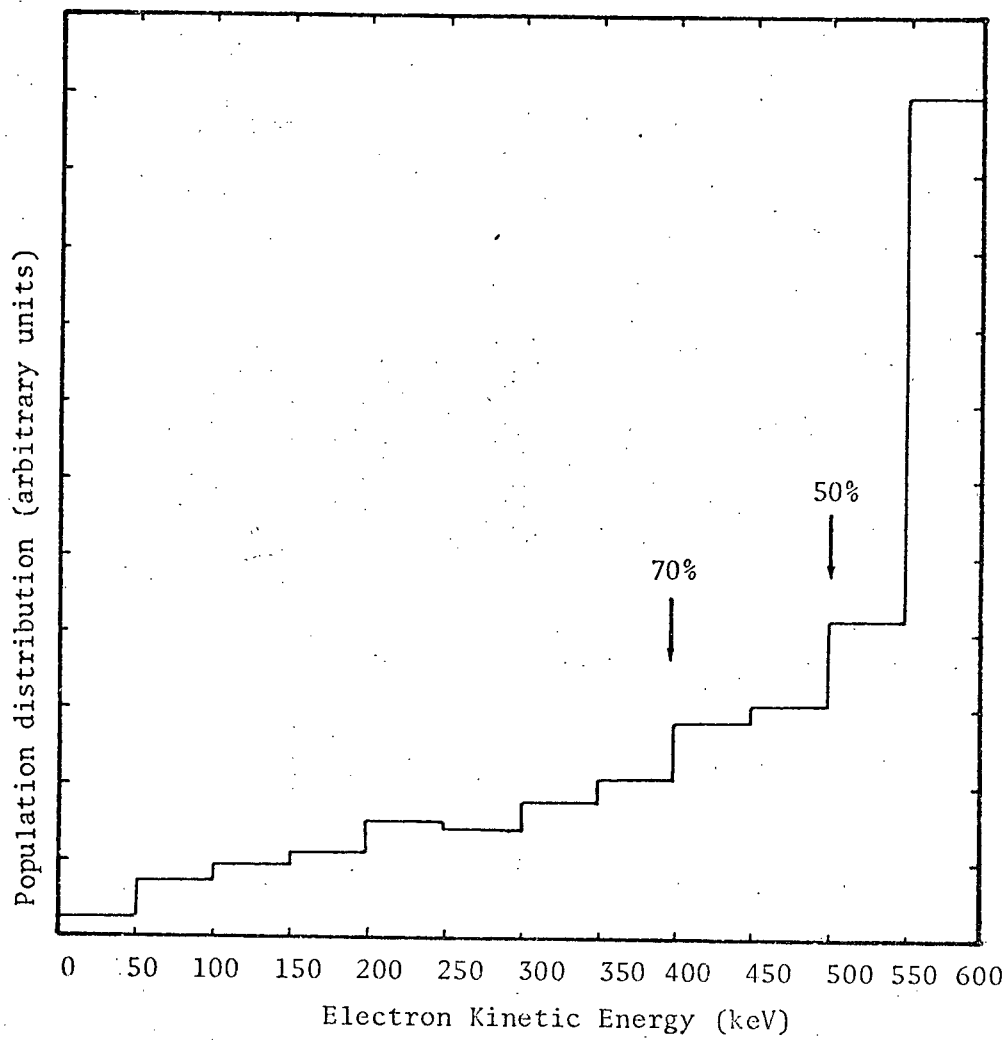
Figure 3-2   The approximate kinetic energy spectrum of the electron pulse from the 5515 tube.
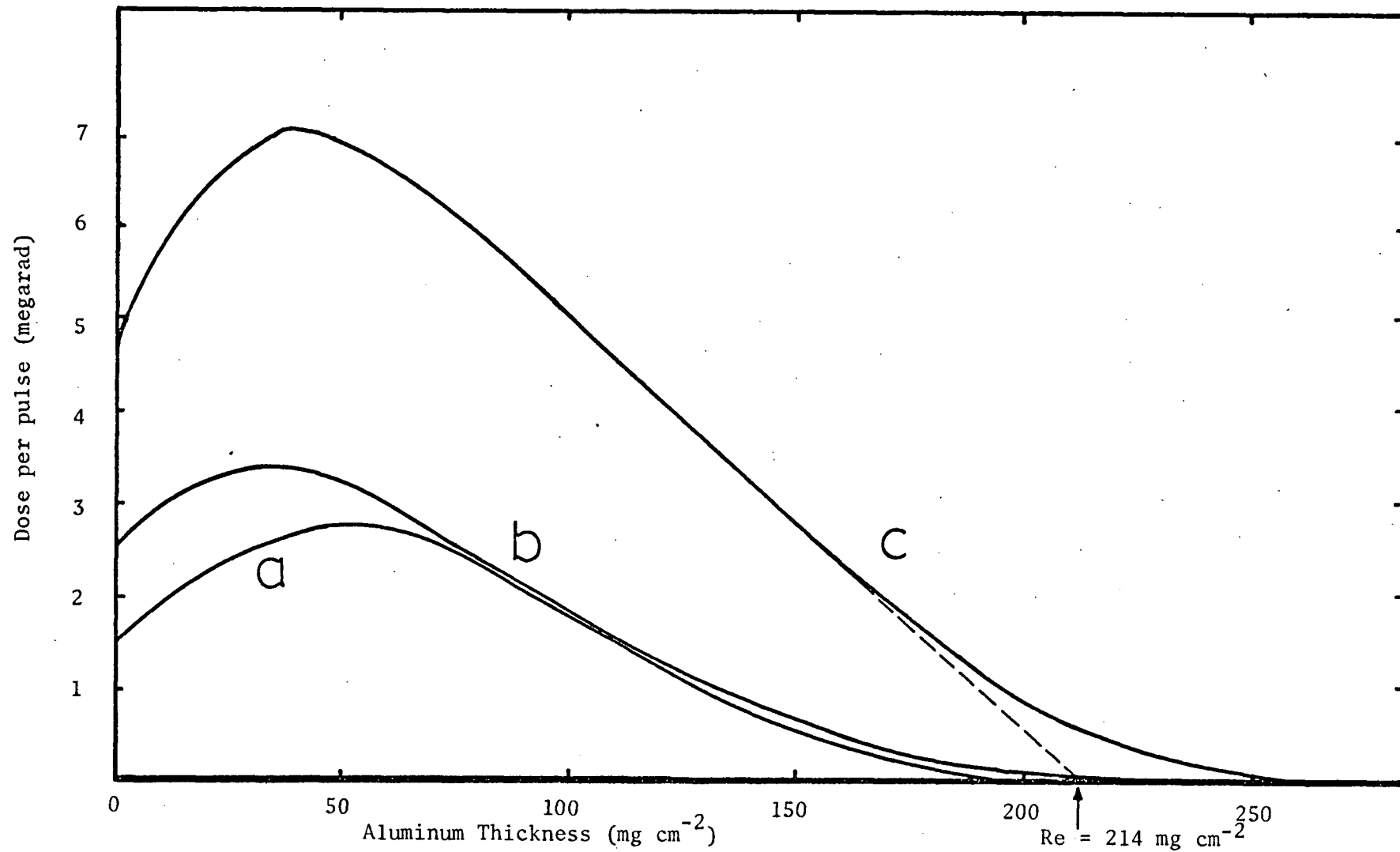
Figure 3-3 Dose-depth distributions in aluminum, for 5510 (b) and 5515 (c) electron tubes. The previously measured dose-depth curve for 500 keV electrons is shown for comparison (a).

Finally, the product of E(t) and I(t) gives the dose rate. This is, from equation (3-1),

$$D(t) = E(t).I(t) = I^2(t).Z \qquad (3-2)$$

where $D(t)$ = dose flux as a function of time

and the result is shown normalized to the current pulse in figure 3-4(a). The fact is that the dose pulse, which is the most meaningful accelerator characteristic to quote, has a width at half-height of about 2.5 nanoseconds for this Febetron. Other evidence reinforcing this conclusion comes from the observation of the Cerenkov radiation pulse emitted from a concentrated solution of H_2O_2 in water, measured with a fast silicon photodiode. The oscilloscope trace in figure 3-4(b) has a width at half height of $\sim$ 2.7 nanoseconds, significantly shorter than the Faraday cup current waveform.

The average electron energy of the Febetron accelerator depends primarily on the charging voltage of the capacitors in the Marx Surge circuit, therefore it is possible to obtain electrons in the energy range $\sim$ 200 to $\sim$ 500 keV. Unfortunately as the charging voltage is decreased the total energy stored in the capacitors also is diminished, so that the output current is decreased. Unless otherwise explicitly stated, all experiments were carried out under conditions of maximum beam energy and current; that is, mean electron energy $\sim$ 0.5 MeV, peak beam current $\sim$ 5000 amperes, and total energy $\sim$ 10 joules.

As well, there are two quite different beam energy density configurations which may be obtained by using the models 5510 or 5515 electron tubes. Both tubes have the same total energy output
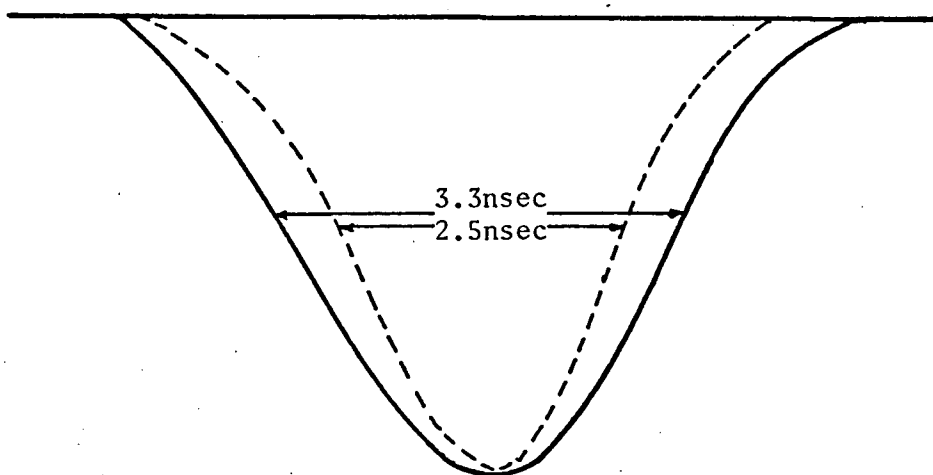
Figure 3-4(a)   Current-time profile (solid line) and dose-time profile
                 (dotted line) measured for the 5515 electron tube using
                 model 1653 Faraday cup and Hewlett Packard 183A oscilloscope.
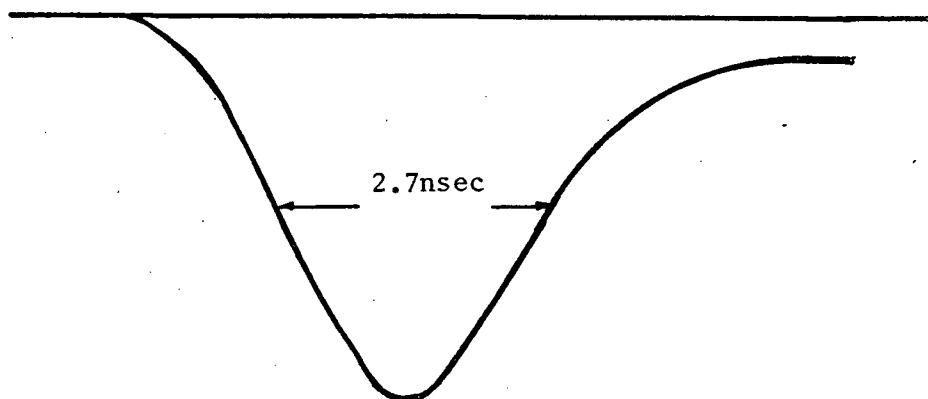
Figure 3-4(b)   Cerenkov pulse shape from 3 molar H_2O_2 in water,
                 observed using a Hewlett Packard 4203 photodiode and
                 183A oscilloscope.

($\sim$ 10 joules) and approximately the same peak electron energy (the
5515 tube has a peak electron energy of $\sim$ 600 keV, while the 5510 tube
has a peak electron energy of $\sim$ 500 keV), however, as shown in figures
3-3, 3-5(a) and 3-5(b), the 5515 tube gives a much higher energy
density than the 5510 tube. The 5515 tube was used for most of this
work, and reference will be made to the 5510 tube where it was
employed.

The pulse-to-pulse reproducibility of the accelerator output
can be defined in several ways, depending on the criterion used.
If one considers the total beam energy (that is, 10J), then the r.m.s.
deviation is about ± 4%. However, if one measures the on-axis dose over
a small area corresponding to the geometry of the radiation cell in
question, then the r.m.s. deviation approaches ± 6%. Investigating
further, it was observed using a Faraday cup, that pulse widths can vary
in the range 2.8 to 3.3 nanoseconds, and that the pulse heights have
an r.m.s. deviation of $\sim$ ± 7%. One may conclude from these facts that
the variation in dose-rate for the Febetron accelerator is much higher
than that quoted by the manufacturers for the total dose output. As
will be clear later a reproducible dose-rate is very important to this
work. The source of this variation is the pulse shortening adapter,
which relies on the reproducible dielectric breakdown of high pressure
air ($\sim$ 240 psi). The pulse width is extremely sensitive to variations
in the dielectric properties of the air in the pulse shortener switch
chamber and therefore for day-to-day operation great care was taken

3-5(a)
Iso-dose curves
for 5510
electron tube
in air,
J cm.$^{-2}$

3-5(a)

Distance from tube axis (cm)
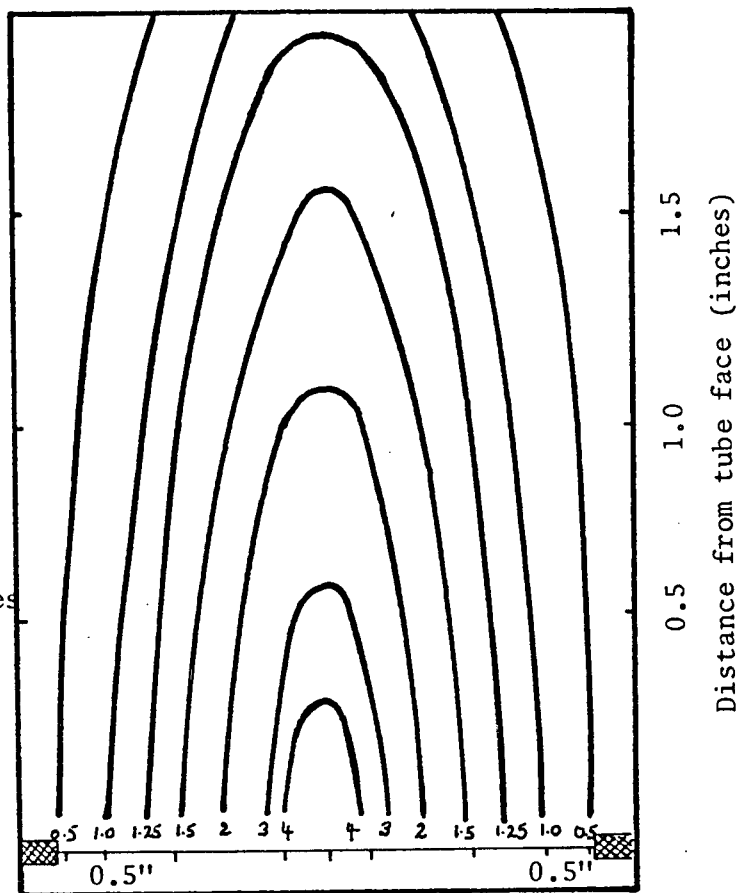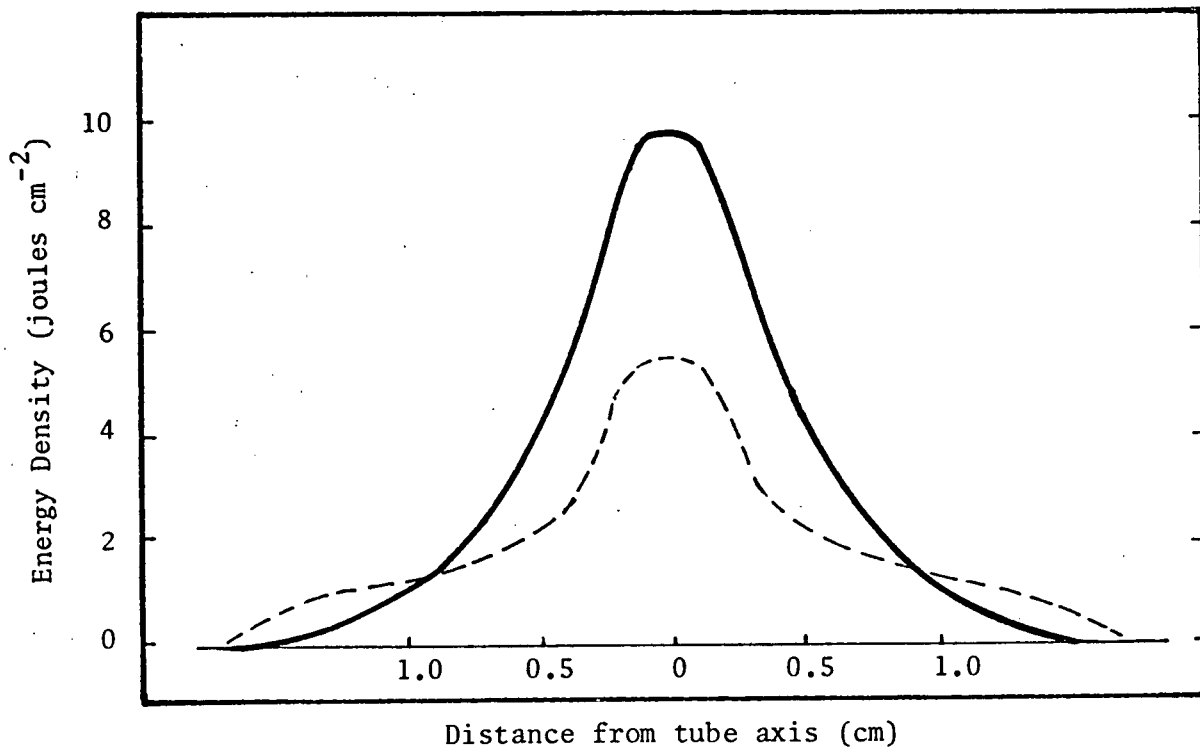
3-5 (b) Comparison of beam energy density for 5510 tube (dotted line)
and 5515 tube (solid line), 1/8" from tube face.

to ensure that exactly the same equilibrium pressure was maintained. As well, frequent purgings (every 50 pulses) were necessary in order to remove the ozone generated by the high voltage discharge. These precautions help to minimize reproducibility problems, however they are no substitute for a regular annual accelerator disassembly and overhaul program.

(B)   Experimental Arrangements for Light Emission Studies

(1)   Radiation Cell

The radiation cell used in all of these experiments is shown in figure 3-6. It consists of an annular stainless steel portion (A), which on one side was screwed onto an aluminum flange (B), thus tautening a .025 millimeter stainless steel electron window against it like a drum head, and on the other side held a quartz optical window. Stainless steel fittings (including stainless steel to glass seals instead of Kovar seals) were used to attach this cell to an all glass He pressurized flow system, in order that relatively corrosive materials such as concentrated H_2O_2 and acids could be handled without contamination. A tight fitting aluminum cap fastened over the quartz window, functioning both as an iris and an electrical interference noise shield, completed the cell assembly.

(2)   Optical Layout and Equipment

The complete experimental arrangement is shown in figure 3-7. The quartz optical light train was designed to provide maximum light collection efficiency for the two spectrographs and the spectrophotometric detection equipment. In all cases the light was condensed to a parallel
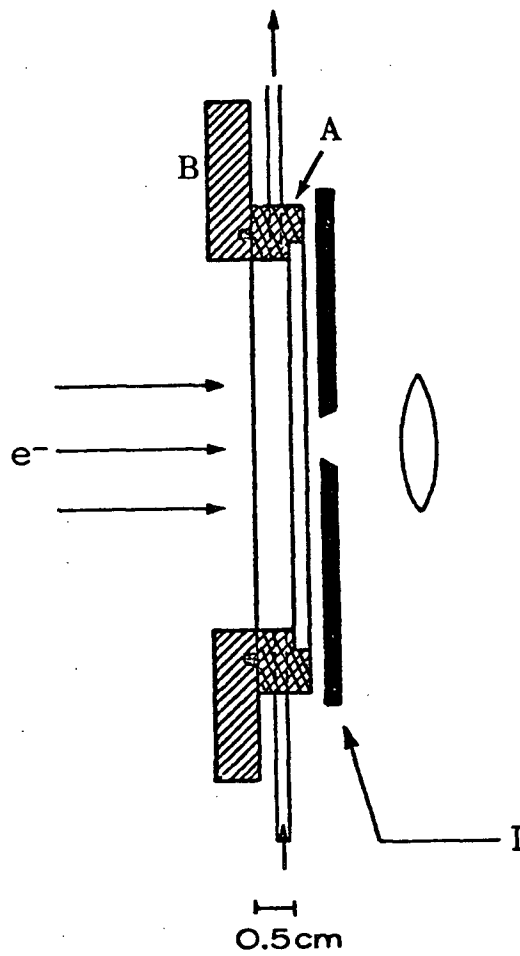
Figure 3-6   Radiation cell, showing light restricting iris (I) and the first light collection lens. The filling and emptying ports are indicated by vertical arrows.
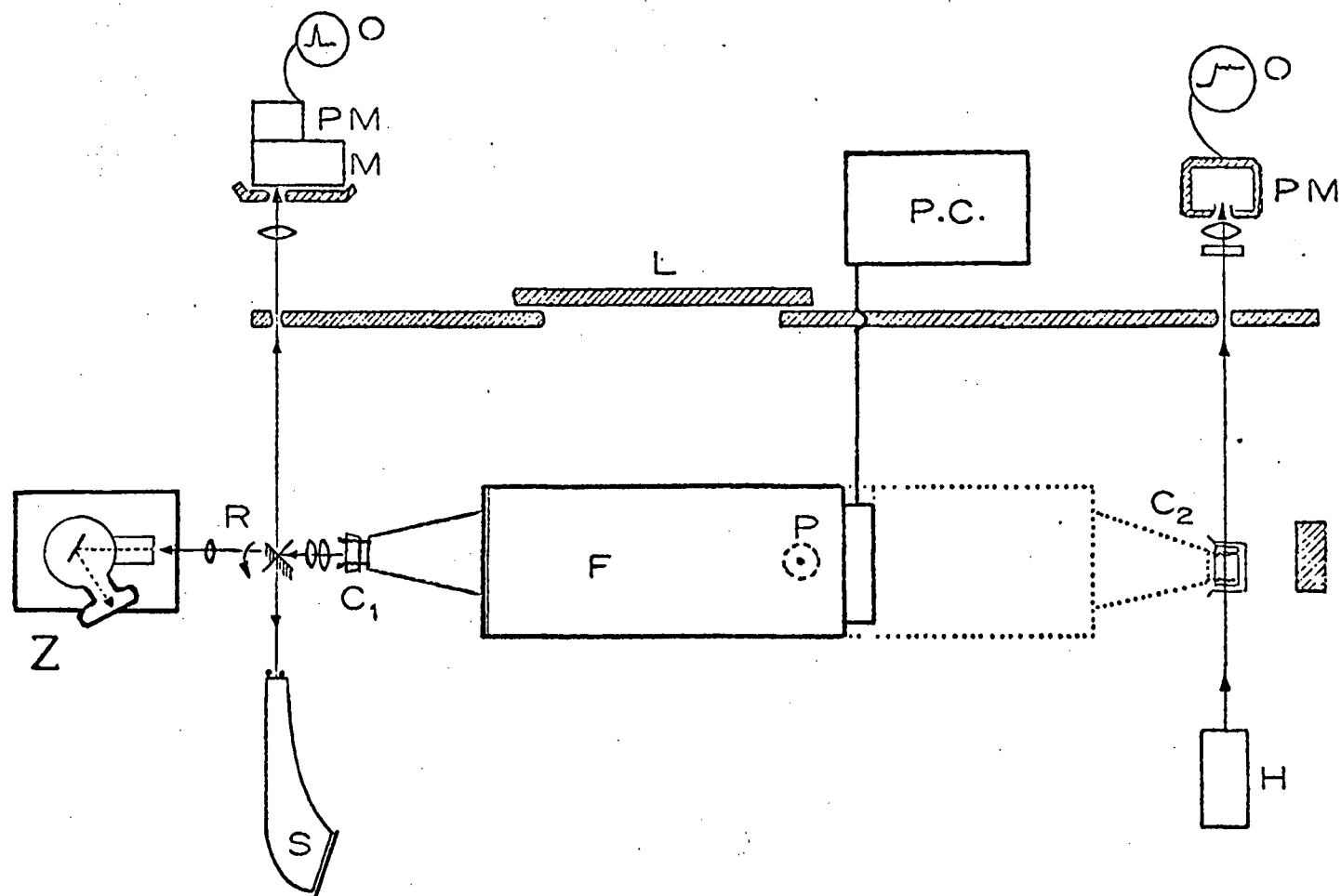
Figure 3-7 Experimental Arrangement; the Febetron (F) is shown in position C_1, for use with the emission apparatus; Z is the Bass-Kessler spectrograph, S is the small Hilger spectrograph and M is the monochromator in front of the photomultiplier (PM) and oscilloscope (0). Position C_2 is for kinetic laser photometry; H is the He-Ne laser and PM the shielded photomultiplier coupled to the oscilloscope (0). P.C. is the power console for the Febetron; P, the pivot allowing the accelerator to move from C_1 to C_2 and R is a rotable mirror.   L marks the $\frac{1}{4}$" lead shields.

light beam with an f/1.0 lens and then reflected by plane mirrors
to be focused onto the slits of the following:

(a)   A small Hilger and Watts quartz prism spectrograph,

        which was used for spectroscopic measurements in

        the ultraviolet and visible.

(b)   A low dispersion grating spectrograph, on the design

        of Bass and Kessler (72), which was used for visible

        and near infrared experiments. This instrument is

        rather unusual, since it is designed for high aperture

        (f/3.5) and high resolution (600 lines per mm on the

        grating), but with a low dispersion at the film of only

        $\sim$ 60 nm per mm in first order. Because of these features,

        it has a remarkable light gathering efficiency,

        and is ideally suited for experiments using infrared

        sensitive film.

(c)   A 0.25 meter f/3.6 Jarrel Ash grating monochromator

        with interchangeable gratings blazed at 300 nm and

        600 nm. The resolution of this instrument was rather

        more than required for this work, being 0.2 nm and 0.5 nm

        with 25 and 100 micron slits respectively.

Corning colour glass filters were always employed in conjunction with
the Bass-Kessler spectrograph for wavelength selection, and to separate
orders, and also with the Jarrell Ash monochromator to eliminate any
possibility of scattered light.

Wavelength calibrations were obtained in the ultraviolet using a low pressure Hg lamp and in the visible and near infrared with a Ne lamp; the latter wavelengths were taken from tables by Lofthus. For the Hilger spectrograph interpolation between Hg lines (where necessary) was carried out using a simple formula of the following form:

$$\lambda = \lambda_o + \frac{c}{d_o - d} \qquad\qquad (4\text{-}3)$$

where λ_o, c d_o are constants and λ and d

are respectively the wavelength and

displacement on the film

The Bass-Kessler spectrograph was used in first order where the dispersion is 57.9 nm per mm and linear within experimental error.

Where spectral sensitivities were required a quartz iodine standard lamp of known emissivity was available. This lamp is calibrated against the U.S. National Bureau of Standards secondary standard and manufactured by Electron Optics Associates (type P117).

(C) Spectrographic Detection Techniques

Because of extreme reciprocity law failure of photographic emulsions to high intensity nanosecond light pulses, it was necessary to investigate a wide range of combinations of film, developer and processing techniques in order to achieve the highest emulsion sensitivity consistent with acceptable sensitometric characteristics (that is, minimum fog and grain size). The results are as follows:

(a) for the near U.V. and visible (300 nm < λ < 680 nm),

Kodak 2475 recording film developed for 5 minutes in Diafine

developer (Acufine Inc.,), baths A and B, at 80°F.

(b) for the near infrared (500 nm < λ < 860 nm), Kodak

     High Speed Infrared film (Estar base), developed for

     7 minutes in D19 (Kodak) at 75°F.

Film densities were recorded with a Joyce Loebel Mark 2 dual beam

microdensitometer. Great care was taken to standardize film processing

and the ensuing film density measurements so that a consistent set of

data would result. The actual theoretical treatment of the film

densities will be discussed later.

(D) Electronic Detection Equipment

The spectrophotometric detection systems described in this section

have been developed with the ultimate goal of observing an undistorted

Cerenkov light pulse induced by the high energy electrons from the

Febetron. This objective has been materially achieved so that some of

the measurements reported in this thesis could be made spectrophotometrically.

(1) Photomultipliers

The advantage of a photomultiplier is that it provides its own

relatively fast and efficient amplification system, so that

comparatively low light levels can be easily detected, even with a low

resistance anode load necessary for high frequency response. Observations

made with an RCA 1P28 photomultiplier (with a linear dynode chain and a

50Ω load) and a Tektronix 454 oscilloscope (rise time < 2.4 nanoseconds)

gave a Cerenkov light pulse from the Febetron about 7 nanoseconds width

at half height and some 15 nanoseconds in duration. Such distortion is of

course unacceptable if one wishes to obtain the area under the time

photon-flux curve in order to determine the total number of photons

per pulse. The following modifications have significantly improved

the frequency response of the detection system so that a typical

waveform has a width at half height of $\sim$ 3 nanoseconds and the

pronounced tailing of the pulse which was observed earlier has been

minimized.

(a) A Phillips type B non-linear dynode chain as shown

in figure 3-8(a) was constructed. Two watt, high

quality carbon resistors of relatively low resistance

were used so that a large dynode current ($\sim$ 15 ma at

1000 V D.C.) was passed.

(b) No load resistance was used; instead, the center

conductor of a RG9/U cable (exactly 50Ω impedance)

was attached to the anode, and the signal terminated

in 50Ω at the oscilloscope input.

(c) The photomultiplier was cooled to dry ice temperature

so that it could be operated at $\sim$ 1000 volts without

extreme noise problems from random thermonic emission

of electrons pulled off the photocathode and the first

dynode by the high potential.

(d) A higher frequency oscilloscope, the Hewlett Packard

183A with a rise time of < 1.5 nanoseconds was employed

in the latter part of this work and has demonstrated its

significant advantage over the Tektronix 454 in high

frequency waveform measurements.

Time (nanoseconds)

0 1 2 3 4 5 6 7 8 9

Millivolts

0
10
20
30
40

Figure 3-8(b). Actual trace of a typical absorbed
Cerenkov emission pulse, measured using the photomultiplier
(as illustrated below) and oscilloscope (HP 183A)
combination described in the text.

H.V.
Supply

R_1 = 12.0 kΩ

R_2 = 6.8 kΩ

R_3-R_7 = 4.7 kΩ

R_8-R_{10} = 6.8 kΩ

R_9 = 12.0 kΩ

R_1 R_2 R_3 R_4 R_5 R_6 R_7 R_8 R_9 R_{10}

Anode

Cathode D_1 D_2 D_3 D_4 D_5 D_6 D_7 D_8 D_9
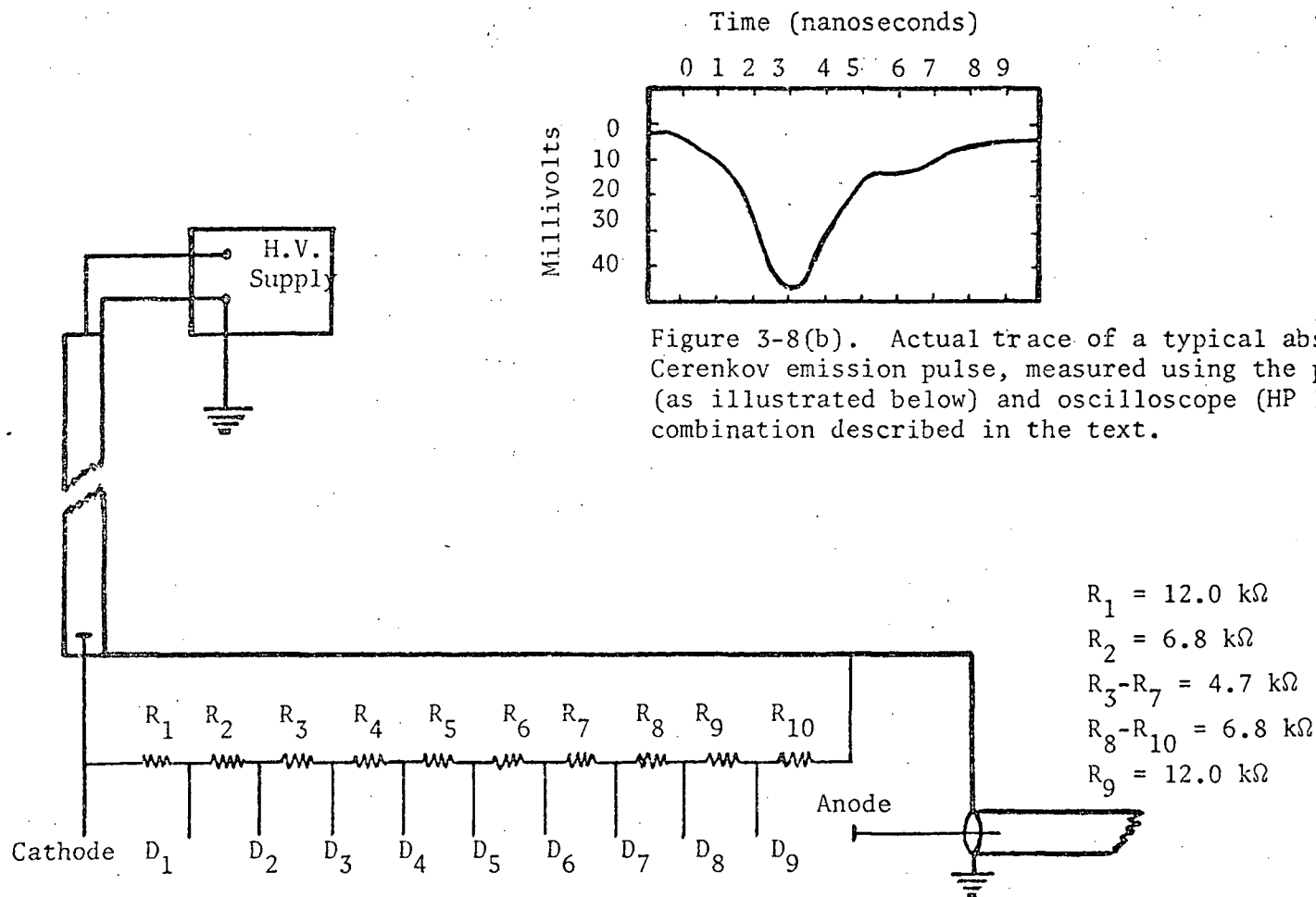
Figure 3-8(a)   Phillips type B dynode chain used in conjunction with a RCA 1P28 photomultiplier and a
Hewlett Packard 183A oscilloscope to obtain the pulse shape in figure 4-8(b).

A typical waveform is shown in figure 3-8(b). It is suggested that this improvement in time resolution is due to the reduction of the electron transit time in the photomultiplier and the improvement of the frequency response of the oscilloscope. The peak photomultiplier current can be shown to be linear up to $\sim$ 3 ma by using neutral density filters; however in normal practice, the peak current drawn was always less than 1 ma.

A Hamamatsu R213 photomultiplier, identical in configuration to a 1P28, but with a more red sensitive photocathode, was also tested. However, it was found that accompanying the increased red sensitivity there was a much higher thermionic noise level and poorer frequency response compared to the 1P28; so that only a few experiments were carried out with this particular tube.

The high operating voltage for the photomultipliers was provided by a Fluke model 412B power supply (0-2100 volts and 0-30 ma), supplying a D.C. voltage stabilized to 0.005 % per hour or 0.02 % over a day's duration.

(2) Photodiode

Compared to a photomultiplier, a pin photodiode is extremely insensitive, but it is also an intrinsically faster detector because of the negligible electron transit time. With this in mind a Hewlett Packard 4203 silicon photodiode was used to monitor the total polychromatic Cerenkov light pulse from an irradiated aqueous H_2O_2 solution (chosen because of no self-absorption). Adequate response could easily be achieved by placing the diode in the unfocused light beam from the

first collecting lens. The simple circuitry required is shown in

figure 3-9. Again, no load resistor was used, the anode being attached

directly to the coaxial cable and a 50Ω terminator acting as the anode

load. The diode was biased at 60 V, slightly higher than the normal

Hewlett Packard specifications, in order to improve the frequency

response (73). It is estimated that the rise time of this detector is

∿ 0.3 nanoseconds. Although the sensitivity of this detector was not

high enough so that it could be used as a substitute for the photo-

multiplier in conjunction with the monochromator, it probably would

be possible to use it with some wider band pass monochromator such

as a continuous line filter, and thus extend measurements into the

infrared, to about 1,100 nm.

(E) Electromagnetic Interference from the Febetron

At the commencement of this work, great difficulties were

encountered with high frequency noise pickup from the Febetron when

it discharged. In retrospect, this problem has been solved relatively

simply, although the path to the solution was rather tortuous and

frustrating. There are two major factors in this interference.

(a) The firing system of the accelerator generated

enormous noise from the pulse-transformer and the

discharge of the thyratron.

(b) The passage of large currents of high energy electrons

through any non-conducting material (either air or

one's sample) induces huge oscillatory signals in

the detection equipment.
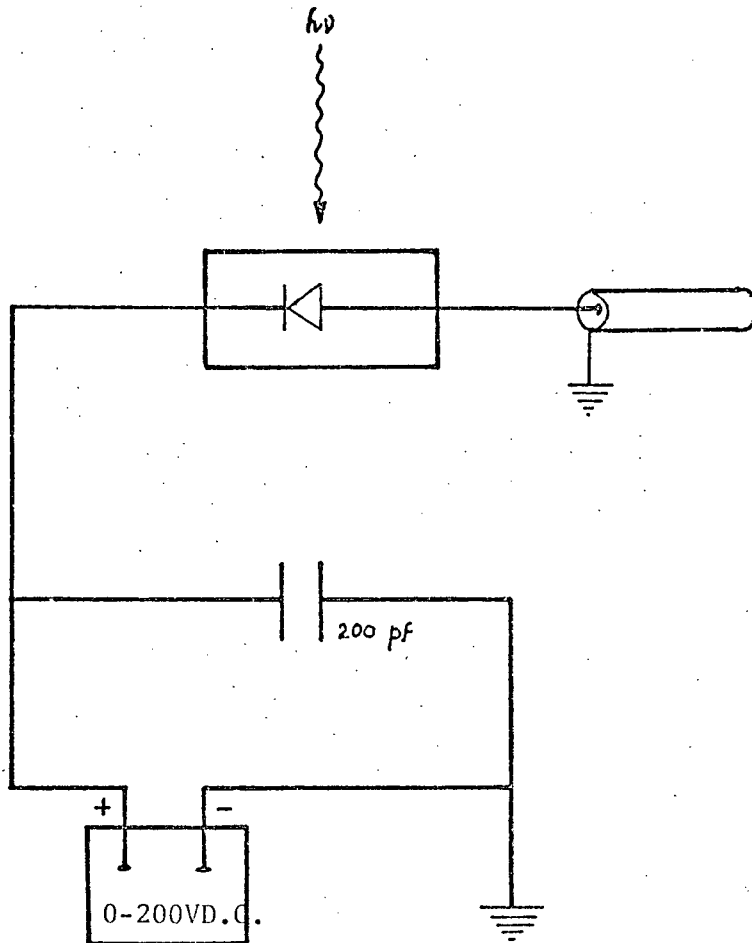
Figure 3-9 Circuitry for the Hewlett Packard 4203
photodiode.

The first problem was solved by Field Emission Corporation, with the introduction of the optional Low Noise Trigger Amplifier Assembly. With this modification all components of the firing system, except for a small trigger initiation source, are mounted on the end of the Febetron immediately behind the Marx Surge capacitor bank, and inside a special noise shield made of cross spun metal yarn. With the elimination of this source of noise the interference from the electron beam became more clearly apparent. Experience has shown that the complete enclosure of the electron beam and any non-conducting material in which it is stopped with tight fitting metal components (normally aluminum) and finally the enclosure of the total assembly with a thick wrapping of tight fitting aluminum foil effectively attenuated all of this noise.

Having shielded the interference at its source, relatively little other screening was necessary. However, because of earlier experiences, the photomultiplier was mounted in a thick brass and lead case and all coaxial cables were of the doubly shielded type. Furthermore, the accelerator was completely isolated, and grounded separately from the building mains to a large copper stake driven into the earth outside the laboratory (fortunately the laboratory is on the ground floor), in order to prevent pickup coming back to the detection equipment through the mains ground.

(F) Radiation Shielding

The accelerator was separated from the operator and all electronic detection equipment by a 1/4 inch lead shielding wall. The shields are

present primarily to protect the operator from stray X-rays generated by the high energy electrons. The X-ray production was usually minimal, because low atomic number target materials were always used. Light passed through holes in the lead shielding to the appropriate photometric detection equipment, which in most cases did not detect X-rays. In the spectrographic experiments, a thick lead shield was always placed around the camera in order to prevent any possibility of X-ray induced exposure of the film.

(G) Dosimetry

Because of the enormous dose and dose-rate from the Febetron, adiabatic calorimetry is the only technique capable of measuring the energy deposited by the electron beam. One simply measures the temperature rise of a thermally insulated target material after the delivery of a single electron pulse. In this work the target was a pure aluminum disc (> 99.5% purity) and the temperature rise was measured with a thermocouple. The transient voltage change ΔV induced by the electron beam is related to the total energy deposited in the calorimeter as follows:

$$\Delta V = \frac{\omega W}{\sigma m}$$

where ω = sensitivity of the thermocouple (V $^\circ C^{-1}$)

W = total energy deposited (joules)

σ = specific heat of the calorimeter (joules g^{-1} $^\circ C^{-1}$)

m = mass of the calorimeter (grams)

Aluminum was always used as the target material; although other metals such as platinum and tantalum have a much smaller value of σ and

therefore a higher sensitivity for equivalent surface density the uncertainty in applying a back-scatter correction ($\sim$ 35% for Pt) compared to aluminum ($\sim$ 4%) more than negates any increased thermal sensitivity from these materials.

As can be seen from figures 3-5(a) and 3-5(b) there is a pronounced spatial non-uniformity of the electron beam. Therefore in order to measure the dose deposited in the very small volume of the radiation cell (from which light for these experiments was extracted) it was necessary to construct the micro-calorimeter shown in figure 3-10, which could be placed in an exactly equivalent irradiation configuration as the radiation cell. It consists of a pure aluminum disc 1 mm thick and 4 mm in diameter held in a Teflon mount. This disc presses against a small diameter thermocouple (.05 mm diameter, manufactured by Omega Engineering Corporation, Stanford, Connecticut) chosen so that its mass would be negligible compared to that of the aluminum calorimeter disc and for its inherently fast rise time.[*] Since only temperature differences are required, no cold junction was used, and the thermocouple was attached directly to a Westronics model S11E/U recording micro-voltmeter. A typical result is shown in figure 3-11(a) The rate of cooling was so fast that it was not possible to accurately follow the time temperature curves on the strip chart recorder. For this reason a small operational amplifier was constructed[**] and its

[*] Thermocouple rise times are proportional to the diameter of the wire used, so that a .05 mm diameter thermocouple has a rise time $\sim$ 1 millisecond.

[**] The author wishes to thank Mr. H. Takagi of the Department of Chemistry Electronics Workshop for the construction of this amplifier.
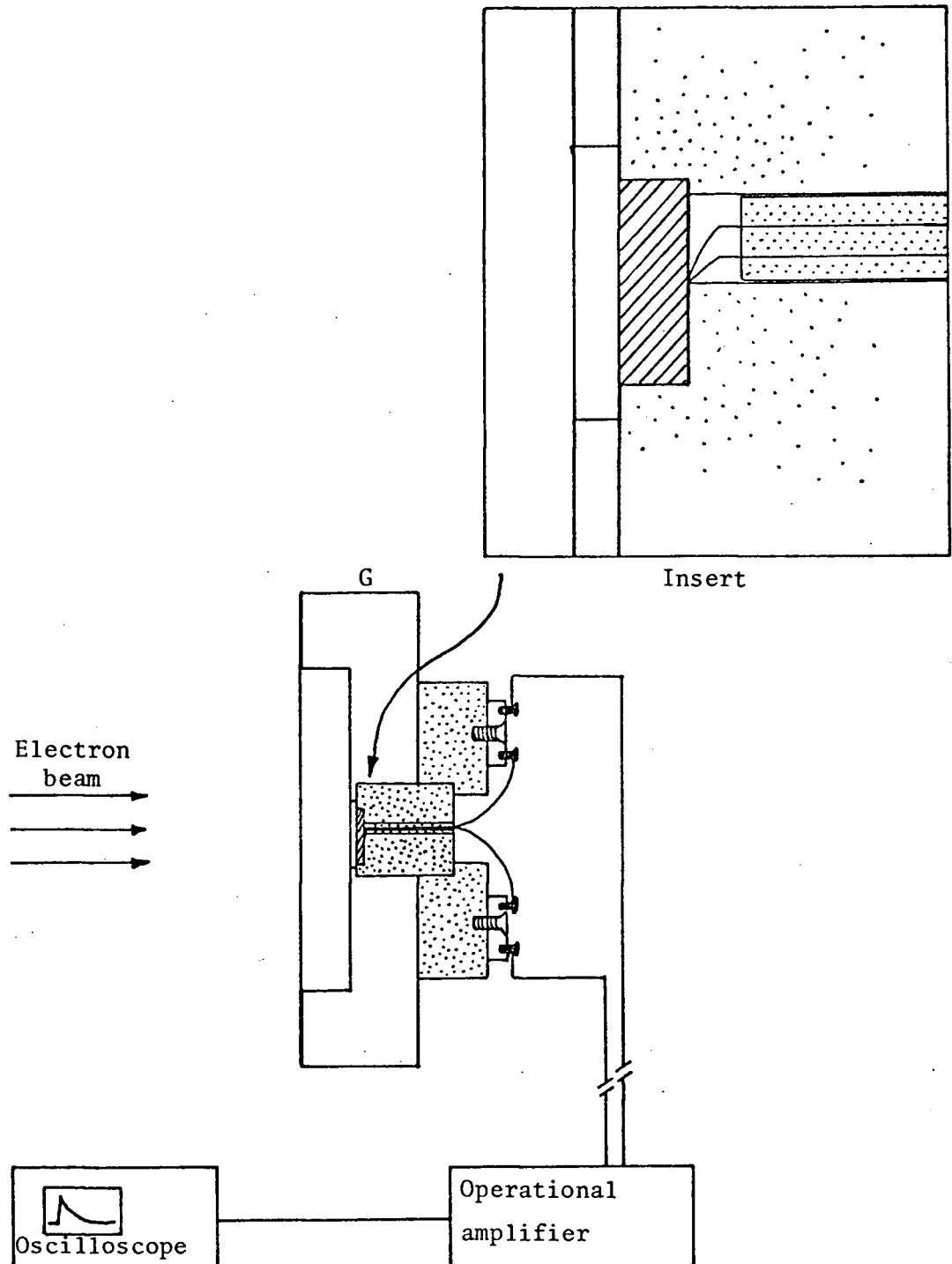
Figure 3-10   Calorimeter assembly and detail of mount (insert). The
              aluminum disc   D, is set off by cross-hatching in contrast to
              the surrounding Teflon insulating mount. This assembly fits
              into an aluminum housing G.

—— Observed temperature time dependence

---- Extrapolation to zero time, using
Newton's Law of Cooling

1 mv

10 sec
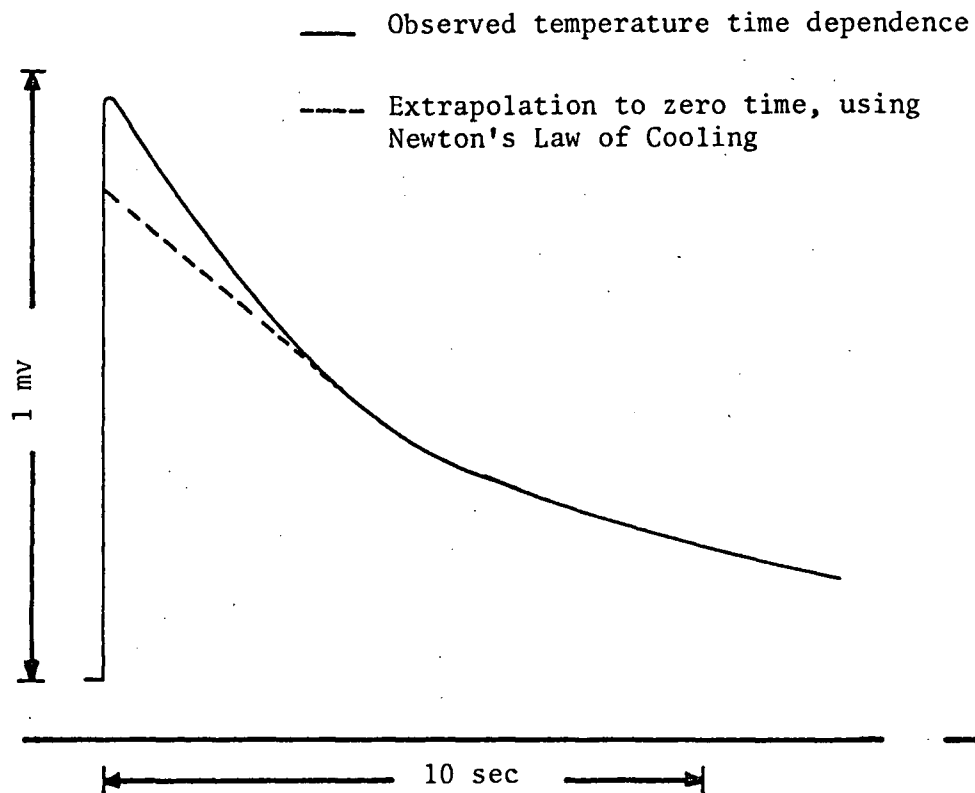
Figure 3-11(b) Oscilloscope tracing of the amplified
thermocouple output.
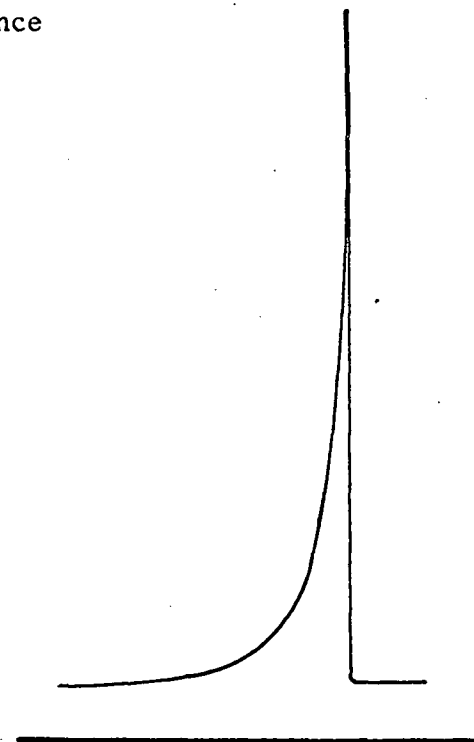
Figure 3-11 (a) A tracing of the output
from the millivolt
recorder.

Figure 3-11 Thermocouple output from the calorimeter disc.

output displayed on the Tektronix 454 oscilloscope. Traces were photographed on Polaroid film for analysis and a typical waveform is shown in figure 3-11(b). Their time temperature curves obeyed Newton's law of cooling for times greater than $\sim$ 4 seconds, so that a small extrapolated correction (shown dotted) was made to zero time in order to obtain the true temperature rise and thus the real dose deposited.

(H) Kinetic Laser Photometry

Some experiments were carried out using the nanosecond absorption pulse radiolysis techniques developed in this laboratory. As a complete description of this apparatus has been given elsewhere (74) only a few relevant details will be mentioned here. The apparatus followed the lines of normal pulse radiolysis equipment except that an He-Ne gas laser was incorporated as a light source, so that only rate constants rather than spectra could be determined. Because of the weak penetration of $\sim$ 0.5 MeV electrons a specially designed radiation cell had to be used. In these experiments the dose was estimated from the initial hydrated electron concentration in pure water.

(I) Experimental Materials

(1) Water

Laboratory distilled water was redistilled from acidified potassium dichromate in a continuously recirculating still. This doubly distilled water was used in the final cleaning stage of all glassware and in the preparation of all aqueous solutions.

(2) Formamide

Reagent formamide from Fisher was first neutralized (75) with NaOH

pellets (using bromothymol blue as an indicator) and then pumped on
for several days with slow heating. Only when the formamide remained
neutral upon heating was the distillation commenced. The middle
fraction (boiling at $\sim 65^{\circ}C$, at a pressure < 1 mm Hg) was slowly collected
over a period of 16 hours over which time the solution remained neutral.
The distillate had a significantly lower U.V. cutoff than the
starting material, and the physical constants such as refractive index
and density were very close to the Chemical Rubber Handbood values
(n_D = 1.4453, obs., 1.4448; ρ = 1.13420, obs. 1.13).

(3) Other materials

All other chemicals used were high quality grades equivalent to
or better than Fisher Certified. These materials were used without
further purification.

Solutions were degassed for about 30 minutes in a closed system
using high purity helium bubbled from a gas dispension stick. Although
early experiments demonstrated that O_2 in its atmospheric equilibrium
concentration ($\sim 10^{-3}$ M) would not reduce the absorption of, for instance
the hydrated electron, on this time scale, the solutions were purged in
order to eliminate CO_2, since its reaction with electrons produces a
species which absorbs relatively strongly in the visible, and might
interfere with the measurement of weak spectra.

All experiments were carried out at a room temperature of 20 ± $2^{\circ}C$.
No further temperature control was necessary.

CHAPTER IV

THE DERIVATION OF THEORETICAL RELATIONSHIPS AS A BASIS FOR THE

INTERPRETATION OF EXPERIMENTAL OBSERVATIONS

(A)   ELECTRON CERENKOV SELF-ABSORPTION (ECSA)

Because of the complicated spatio temporal properties of the

Cerenkov radiation emitted from the irradiated solutions in these

experiments, observed optical densities cannot be simply equated to the

$G\varepsilon$ product for the absorbing species. The following theoretical

treatment attempts to obtain expressions relating experimental

observables to short time scale spectra and primary chemical yields, as

well as giving an insight into the effects which result in this self-

absorption.

(1)   Spectrographic Detection

In these spectrographic experiments, the photographic emulsion

measures the total number of incident photons per pulse. Therefore the

absorbance U may be obtained directly from the density of the film,

$$U = \log_{10} I_o/I_t \qquad (4-1)$$

where I_o = total light per pulse with no self-absorption, and

$\quad I_t$ = total light per pulse with self-absorption.

These quantities are as follows:

$$I_o = \int_o^{\tau_p} I_o(t)dt \qquad (4-2)$$

$$I_t = \int_o^{\tau_p} I_t(t)dt \qquad (4-3)$$

where $I_o(t)$ and $I_t(t)$ are the photon fluxes as a function of time and τ_p is the pulse length.

Then,

$$U = \log_{10} \frac{\int_o^{\tau_p} I_o(t)dt}{\int_o^{\tau_p} I_t(t)dt} \qquad (4-4)$$

and in general

$$U \neq \int_o^{\tau_p} \log_{10} \frac{I_o(t)dt}{I_t(t)} \qquad (4-5)$$

Since $I_t(t)$ will be a function of the product $G\epsilon$ for the absorbing species the goal of these calculations is the evaluation of equation (4-4) to obtain an explicit expression for U as a function of $G\epsilon$.

The starting point for these calculations will be the 'monoenergetic approximation', which is as follows:

All high energy electrons from the Febetron 701/2667 are assumed to be of the same energy, so that the rate of Cerenkov light emission and the rate of dose deposition will be directly proportional to the electron flux at any time during the pulse.

The implications of this approximation will be discussed later, along with other approximations to be introduced as this treatment is developed, when numerical comparison can be made.

Beginning with the zeroth order approach, designated approximation
a, one postulates further that all Cerenkov radiation is produced in an
infinitely thin layer at the front edge of the irradiation cell as
shown in figure 4-1.

Cerenkov radiation produced here

and absorbed here

a_d is the maximum depth of

energy deposition.
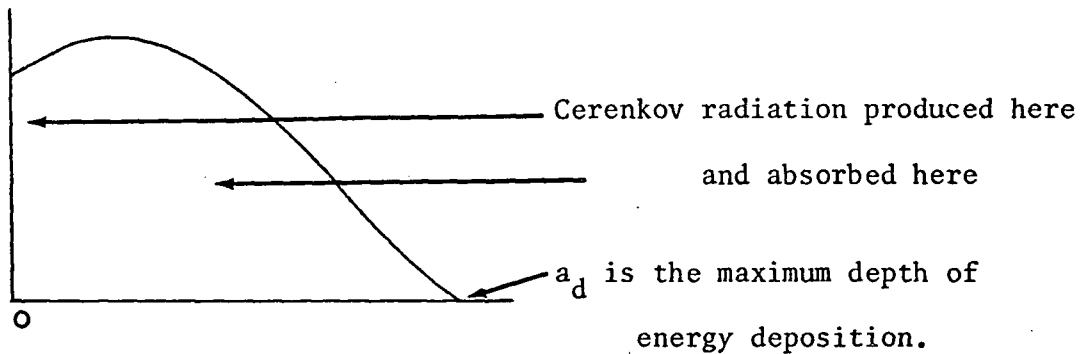
figure 4-1

For equation (4-4) one requires $I_o(t)$ and $I_t(t)$, so first what is $I_o(t)$?

$$I_o(t) = \lambda \xi_n g(t) \qquad (4-6)$$

where λ = constant in units of photons per electron in a specified
wavelength range $\Delta\lambda$,

$\xi_n g(t)$ = the number of electrons per unit time as a function of time
which is equivalent to the electron flux in units of electrons per second.

  $g(t)$ = a function of time, to be chosen later. The general case will
be derived so that any $g(t)$ may be used.

Secondly, what is $I_t(t)$? Equivalent forms of Beer's Law are:

$$OD = \log_{10} \frac{I_o}{I_t} = \epsilon c \ell \qquad (4-7)$$

or $\quad\quad I_t = I_o \exp \{- \alpha c \ell\}$ $\quad\quad\quad\quad$ (4-8)

where $\quad \alpha = 2.303 \, \varepsilon$ $\quad\quad\quad\quad\quad\quad$ (4-9)

However, for the sake of convenience in calculation, equation (4-10) will be used throughout, giving

$$I_t = I_o \exp \{-2.303 \, OD\} \quad\quad\quad\quad (4-10)$$

Thus, without being explicit about the form of OD(t), the time dependence may be included directly as:

$$I_t(t) = I_o(t) \exp \{-2.303 \, OD(t)\} \quad\quad\quad\quad (4-11)$$

The calculation of OD(t) is now made in order to substitute into equation (4-11); first, in order to simplify the calculation, one replaces the nonhomogeneous concentration illustrated in figure 1 by $\bar{c}$, an average concentration within $0 \longrightarrow a_d$.

$$\bar{c} = \frac{1}{a_d} \int_o^{a_d} c(x) dx \quad\quad\quad\quad (4-12)$$

where a_d is the furthest depth of energy deposition and c(x) is the concentration of absorbing species as a function of the depth, x. Then, neglecting the time dependence of c,

$$OD = \varepsilon \bar{c} a_d = \varepsilon \left[\frac{1}{a_d} \int_o^{a_d} c(x) dx \right] \cdot a_d \quad\quad\quad\quad (4-13)$$

$$= \varepsilon \int_o^{a_d} c(x) dx$$

Thus including a time dependence one has,

$$OD(t) = \varepsilon \int_0^{a_d} c(x,t)dx \qquad (4-14)$$

and upon substitution back into equation (4-11),

$$I_t(t) = I_0(t) \exp\{-2.303 \, \varepsilon \int_0^{a_d} c(x,t)dx\}. \qquad (4-15)$$

One must now derive an expression for $c(x,t)$ or alternatively the integral $\int_0^{a_d} c(x,t)$. At this point the lifetime of the absorbing species relative to the duration of the electron pulse must be considered. There are three cases:

(i)   lifetime $\gg \tau_p$

(ii)   lifetime $\sim \tau_p$ where τ_p is the

(iii)   lifetime $\ll \tau_p$ pulse duration.

a(i)   Lifetime of the absorbing species $\gg \tau_p$.

The rate of increase in concentration as a function of time (for a primary species) is as follows:

$$\frac{\partial c(x,t)}{\partial t} = \xi \, D(x,t) \qquad (4-16)$$

where $D(x,t)$ is the dose as a function of depth and time and ξ is a constant relating dose to concentration. By the monoenergetic approximation one may write down an expression for $D(x,t)$,

$$\xi \cdot D(x,t) = \xi_d \, D(x) \cdot \xi_n g(t) \qquad (4-17)$$

where $D(x)$ is the dose as a function of depth for $\underline{one}$ electron in eV gm^{-1}, ξ_d is a constant converting $D(x)$ eV gm^{-1} to concentration (molar) and

$\xi_n g(t)$ is the high energy electron flux as a function of time.

At this stage it will be convenient to introduce several symbols which will be required in later equations. For simplicity let

$$E_o = \frac{1}{a} \int_o^{a_d} D(x)dx = \text{total dose deposited per electron,} \quad \text{eV g}^{-1} \quad (4\text{-}18)$$

Define

$$D^* = \int_o^{a_d} D(x)dx \quad (4\text{-}19)$$

Thus

$$D^* = E_o \cdot a_d \quad (4\text{-}20)$$

The reason for this diversion will be apparent in subsequent pages.

If one combines equations (4-16) and (4-17), where

$$\xi = \xi_d \cdot \xi_n, \quad \frac{\partial c(x,t)}{\partial t} = \xi_d D(x) \cdot \xi_n g(t). \quad (4\text{-}21)$$

The monoenergetic approximation implies that

$$c(x,t) = c(x) \cdot c(t) \quad (4\text{-}22)$$

since compared to the length of the pulse the time taken for an electron to travel from $0 \longrightarrow a_d$ is negligible, and diffusion of chemical species in a few nanoseconds is small (this of course also assumes that the species is a primary product of the radiation and formed within a few picoseconds). Thus, one may write

$$c(x)\frac{dc(t)}{dt} = \xi_d D(x) \cdot \xi_n g(t) \quad (4\text{-}23)$$

and make the identifications,

$$c(x) = \xi_d D(x) \quad (4\text{-}24)$$

$$\frac{dc(t)}{dt} = \xi_n g(t) \quad (4\text{-}25)$$

Therefore from equation (4-25)

$$c(t) = \int_{o}^{t} \xi_n \, g(t')dt' \qquad (4\text{-}26)$$

while from equation (4-22),

$$c(x,t) = \xi_d \, D(x) \int_{o}^{t} \xi_n \, g(t')dt' \qquad (4\text{-}27)$$

One recalls from equation (4-14) that,

$$OD(t) = \epsilon \int_{o}^{a_d} c(x,t)dx \qquad (4\text{-}14)$$

therefore substituting (4-27) into (4-14)

$$OD(t) = \epsilon \int_{o}^{a_d} \left\{ \xi_d D(x) \int_{o}^{t} \xi_n \, g(t')dt' \right\} dx \qquad (4\text{-}28)$$

$$OD(t) = \epsilon c(t) \int_{o}^{a_d} \xi_d \, D(x)dx \qquad (4\text{-}29)$$

From equations (4-19) and (4-20),

$$\int_{o}^{a_d} D(x)dx = E_o \cdot a_d \qquad (4\text{-}30)$$

thus substituting equation (4-30) into (4-29)

$$OD(t) = \epsilon \, E_o \, a_d \, \xi_d \cdot c(t) \qquad (4\text{-}31)$$

and finally, incorporating $c(t)$ from equation (4-26),

$$OD(t) = \epsilon \, E_o \, a_d \, \xi_d \int_{o}^{t} \xi_n \, g(t')dt'. \qquad (4\text{-}32)$$

One must next equate the constants E_o, a_d, ξ_d and ξ_n to physical

quantities which may be determined experimentally.

The function $\xi_n g(t)$ which will be chosen later to approximate the dose pulse, must satisfy the condition that:

$$\int_o^{\tau_p} \xi_n g(t)dt = \text{total number of electrons per pulse} \qquad (4\text{-}33)$$

$$\text{Let } Q = \int_o^{\tau_p} g(t)dt \qquad (4\text{-}34)$$

and I_q be the total number of electrons per pulse.

Then

$$\xi_n = \frac{I_q}{Q} = \frac{\text{Total number of electrons per pulse}}{\int_o^{\tau_p} g(t)dt} \qquad (4\text{-}35)$$

If equation (4-35) is now substituted into (4-32),

$$OD(t) = \varepsilon \, E_o \, I_q \, a_d \, \xi_d \, \frac{1}{Q} \int_o^t g(t')dt' \qquad (4\text{-}36)$$

In the above expression the product $E_o I_q$ is in fact the total dose

per pulse: $\quad E_o I_q = \dfrac{\text{dose eV g}^{-1}}{\text{electron}} \quad \dfrac{\text{number of electrons}}{\text{pulse}}$

$$\qquad (4\text{-}37)$$

$$= \frac{\text{total dose}}{\text{pulse}} \text{ eV g}^{-1}$$

The total dose per pulse deposited in the volume of sample in which

the absorbing species are produced is measured by adiabatic calorimetry,

and is equal to:

$$E_o I_q = \frac{D_A}{a_d \cdot \rho} \quad \text{where } D_A = \frac{\text{Dosecal}}{\text{Arcal}} \qquad (4\text{-}38)$$

The term Dosecal refers to the total amount of energy absorbed by a given

calorimeter, and its value is independent of the mass of the calorimeter providing all the electrons are stopped; Arcal is the area of the calorimeter, this value is chosen to be sufficiently small such that the value of the energy density obtained is the same as that for the irradiated sample volume. Thus D_A is the surface dose from the electron beam. As noted earlier, a_d is the maximum depth of energy deposition in the material of interest, and ρ is the density of the latter.

The function ξ_d, converting $eV.g^{-1}$ to moles. $litre^{-1}$ may be written as

$$\xi_d = \frac{10\rho G}{N_o} \qquad (4-39)$$

where G is the 100 eV yield of the absorbing species and N_o is Avagadro's number. Substituting for ξ_d and $E_o I_q$ in equation (4-36) one obtains:

$$OD(t) = \varepsilon \frac{D_A}{a_d.\rho} \quad a_d \frac{10\rho G}{N_o} \quad \frac{1}{Q} \int_o^t g(t')dt' \qquad (4-40)$$

$$= G \, \varepsilon \, 10 \, \frac{D_A}{N_o} \, \frac{1}{Q} \int_o^t g(t')dt'$$

Following from equation (4-11),

$$I_t(t) = I_o(t) \exp \left\{-2.303 \, (G\varepsilon) \, 10 \, \frac{D_A}{N_o} \, \frac{1}{Q} \int_o^t g(t')dt'\right\} \qquad (4-41)$$

Equation (4-41) is the generalised expression for $I_t(t)$ into which it is necessary to substitute the following variables,

    (a) $g(t)$, a function proportional to the pulse shape,

    (b) the energy density of the electron beam,

    (c) $G\varepsilon$, the product of the yield and extinction coefficient of the absorbing species.

One must now choose a suitable function for $\xi_n\, g(t)$; there are two

suitable choices.

$$\text{Case I}\quad \xi_n\, g(t) = \xi_n \sin \frac{\pi}{b} t, \text{ where } b = \tau_p. \tag{4-42}$$

$$\text{Case II}\quad \xi_n\, g(t) = \xi_n t \qquad , \quad 0 \leqslant t \leqslant \frac{b}{2} \tag{4-43}$$

$$= \xi_n(b-t) \qquad , \quad \frac{b}{2} \leqslant t \leqslant b \tag{4-44}$$

Case I will be examined first for the condition that the lifetime of the

absorbing species is much greater than the duration of the pulse.

Case I, a(i).

One requires $\dfrac{1}{Q}$ and $\displaystyle\int g(t')dt'$:

$$\xi_n\, g(t) = \xi_n \sin \frac{\pi}{b} t \tag{4-42}$$

Thus

$$Q = \int_o^b \sin \frac{\pi}{b} t\, dt = \frac{b}{\pi}\left[\{-\cos \frac{\pi}{b} t\}\right]_o^b = \frac{2b}{\pi} \tag{4-43}$$

$$\text{and } \frac{1}{Q} = \frac{\pi}{2b} \; .$$

$$\int_o^t \sin \frac{\pi}{b} (t')dt' = \frac{b}{\pi}\left[\{-\cos \frac{\pi}{b} t'\}\right]_o^t = \frac{b}{\pi}$$

$$= \frac{b}{\pi} (1 - \cos \frac{\pi}{b} t) \tag{4-44}$$

Equations (4-43) and (4-44) may be substituted into equation (4-40) to

obtain,

$$OD(t) = G\ \epsilon.\left(\frac{10\ D_A}{N_o}\right) \cdot \frac{\pi}{2b} \frac{b}{\pi} (1 - \cos \frac{\pi}{b} t)$$

$$= G\ \epsilon. \frac{5D_A}{N_o} \cdot (1 - \cos \frac{\pi}{b} t) \tag{4-45}$$

Letting $S_o = G \, \epsilon. \, \frac{S}{N_o} D_A$ so that (4-46)

$$OD(t) = S_o (1 - \cos \frac{\pi}{b} t) \qquad (4\text{-}47)$$

and making the further substitution in equation (4-11):

$$I_t(t) = I_o(t) \exp \{-2.303 \, S_o (1 - \cos \frac{\pi}{b} t)\} \qquad (4\text{-}48)$$

It has already been established that $I_o(t) = \lambda \xi_n \, g(t)$ (4-6)

so for this case, $I_o(t) = \lambda \xi_n \, \sin \frac{\pi}{b} t$ (4-49)

Therefore, substituting (49) into (48), one has

$$I_t(t) = \lambda \xi_n \, \sin\frac{\pi}{b} t . \exp \{-2.303 \, S_o (1 - \cos \frac{\pi}{b} t)\} \qquad (4\text{-}50)$$

and finally from equation (4-4)

$$U = \log_{10} \frac{\int_o^{\tau_p} I_o(t) dt}{\int_o^{\tau_p} I_t(t) dt} \qquad (4\text{-}4)$$

for case Ia(i)

$$U = \log_{10} \frac{\int_o^b \lambda \xi_n \, \sin \frac{\pi}{b} t \, dt}{\int_o^b \lambda \xi_n \, \sin \frac{\pi}{b} t . \exp \{-2.303 \, S_o (1 - \cos \frac{\pi}{b} t)\} \, dt} \qquad (4\text{-}51)$$

The evaluation of equation (4-51) is given in Appendix A; the result is

$$U = \log_{10} (4.61 \, S_o)$$

$$= \log_{10} (23.0 \, G \, \epsilon \, \frac{D_A}{N_o}) \qquad (4\text{-}52)$$

Before discussing the significance of this equation the same result will

be derived for a different pulse shape, represented by Case II.

Case II,a(i).

Here one is concerned with a triangular pulse shape

$$\xi_n g(t) = \xi_n t \qquad 0 \leqslant t \leqslant \frac{b}{2} \qquad (4\text{-}43)$$

$$= \xi_n(b - t), \frac{b}{2} \leqslant t \leqslant b \qquad (4\text{-}44)$$

time
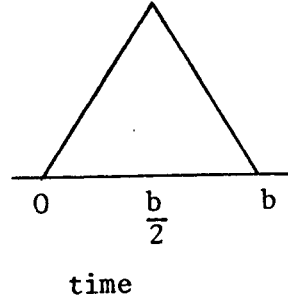
Once again, Q must be evaluated first:

$$Q = \int_0^{b/2} t \, dt + \int_{b/2}^{b} (b - t) dt \qquad (4\text{-}54)$$

$$= \frac{t^2}{2} \Big|_0^{b/2} + \left(bt - \frac{t^2}{2}\right)\Big|_{b/2}^{b} \qquad (4\text{-}55)$$

$$Q = \frac{b^2}{4} \qquad (4\text{-}56)$$

and

$$\frac{1}{Q} = \frac{4}{b^2} \qquad (4\text{-}57)$$

Next, the integral of g(t) is calculated.

$$\int_0^t g(t')dt' = \int_0^t t' dt', \qquad 0 \leqslant t \leqslant \frac{b}{2} \qquad (4\text{-}58)$$

or,

$$= \frac{b^2}{8} + \int_{b/2}^{t} (b - t')dt', \frac{b}{2} \leqslant t \leqslant b. \qquad (4\text{-}59)$$

Integrating,

$$\int_0^t t' dt' = \frac{t^2}{2} \qquad (4\text{-}60)$$

$$\int_{b/2}^{t} (b - t')dt' = bt' - \frac{t'^2}{2} \Big|_{b/2}^{t} \qquad (4\text{-}61)$$

Now, substituting (4-60) and (4-61) into equations (4-58) and (4-59),

$$\int_0^t g(t')\,dt' = \frac{t^2}{2} \quad \text{for} \quad 0 \leqslant t \leqslant \frac{b}{2} \tag{4-62}$$

$$= \frac{-t^2}{2} + bt - \frac{b^2}{4} \quad \text{for} \quad \frac{b}{2} \leqslant t \leqslant b \tag{4-63}$$

Letting

$$t^2 = J_1(t) \qquad 0 \leqslant t \leqslant \frac{b}{2} \tag{4-64}$$

$$-t^2 + 2bt - \frac{b^2}{2} = J_2(t), \quad \frac{b}{2} \leqslant t \leqslant b \tag{4-65}$$

Consequently,

$$OD(t) = G\,\epsilon\,10\,\frac{Dosecal}{Arcal.N_o}\,\frac{4}{b^2}\,\frac{1}{2}\,J_1(t)\,, \quad 0 \leqslant t \leqslant \frac{b}{2} \tag{4-66}$$

or,

$$= G\,\epsilon\,\frac{Dosecal}{Arcal.N_o}\,\frac{4}{b^2}\,\frac{1}{2}\,J_2(t), \quad \frac{b}{2} \leqslant t \leqslant b \tag{4-67}$$

Let

$$T_o = \frac{20\,G\,\epsilon\,Dosecal}{Arcal\,N_o b^2}$$

So that

$$OD(t) = T_o J_i(t), \quad i = 1, 0 \leqslant t \leqslant \frac{b}{2} \tag{4-69}$$

$$i = 2, \frac{b}{2} \leqslant t \leqslant b$$

One may now substitute in equation (4-11)

$$I_t(t) = I_o(t)\,\exp\,\{-2.303\,OD(t)\} \tag{4-11}$$

$$I_t(t) = I_o(t)\,\exp\,\{-2.303\,T_o J_1(t)\} \quad 0 \leqslant t \leqslant \frac{b}{2}$$

$$= I_o(t)\,\exp\,\{-2.303\,T_o\,t^2\} \tag{4-70}$$

and,

$$I_t(t) = I_o(t)\,\exp\,\{-2.303\,T_o J_2(t)\} \quad \frac{b}{2} \leqslant t \leqslant b$$

$$= I_o(t)\,\exp\,\{-2.303\,T_o(-t^2 + 2bt - \frac{b^2}{2})\} \tag{4-71}$$

recalling, $I_o(t) = \lambda \xi_n t \quad , \quad 0 \leqslant t \leqslant \dfrac{b}{2}$ \hfill (4-72)

$\qquad\qquad = \lambda \xi_n (b-t), \quad \dfrac{b}{2} \leqslant t \leqslant b$ \hfill (4-73)

Therefore substituting into equations (4-70) and (4-71)

$$I_t(t) = \lambda \xi_n t \, \exp\{-2.303 \, T_o t^2\} \quad 0 \leqslant t \leqslant \frac{b}{2} \tag{4-74}$$

$$I_t(t) = \lambda \xi_n (b - t) \, \{\exp \, -2.303 \, T_o \, (-t^2 + 2 \, bt - \frac{b^2}{2})\} \tag{4-75}$$

$$\frac{b}{2} \leqslant t \leqslant b$$

Equations (4-74) and (4-75) are finally substituted into equation (4-4):

$$U = \log_{10} \frac{\displaystyle\int_o^b I_o(t)dt}{\displaystyle\int_o^b I_t(t)dt} \tag{4-4}$$

$$U = \log_{10}\left[\frac{\displaystyle\int_o^{b/2} \lambda \xi_n \, t \, dt + \int_{b/2}^b \lambda \xi_n (b-t)dt}{\displaystyle\int_o^{b/2} dt \, \lambda \xi_n t \, \exp \, (-2.303 \, T_o t^2) + \int_{b/2}^b dt \, \lambda \xi_n (b-t) \cdot}\right.$$

$$\exp \, \{-2.303 \, T_o(-t^2 + 2bt - \frac{b^2}{2}$$

$$\tag{4-76}$$

Equation (4-76) is evaluated in Appendix B, and the result is the same as in Case Ia(i),

$$U = \log_{10} \, (23.0 \, \frac{G \, \epsilon}{N_o} \, D_A) \tag{4-52}$$

Exactly the same expression has been obtained as with the sine function. The reason for this result is that because the decay of the absorbing species is not considered, the absorbance is independent of the pulse shape.

The following series of calculations allow for the decay of the absorbing species during the pulse.

a(ii) Lifetime of the absorbing species $\sim \tau_p$.

Returning to equation (4-16), one may add a term $- k_1 c(x,t)$ expressing a first order decay of the absorbing species. This choice reflects the experimental conditions in which species decay via predominantly pseudo-first order kinetics.

$$\frac{\partial c(x,t)}{\partial t} = \xi D(x,t) - k_1 c(x,t) \tag{4-77}$$

or

$$\frac{\partial c(x,t)}{\partial t} + k_1 c(x,t) = \xi D(x,t) = \xi_d D(x) . \xi_n g(t) \tag{4-78}$$

Since $D(x,t) = \xi_d D(x) . \xi_n g(t)$ by the monoenergetic approximation equation (4-78) shows directly that one may write:

$$c(x) . \frac{dc(t)}{dt} + c(x) k_1 c(t) = \xi_d D(x) . \xi_n g(t) \tag{4-79}$$

Because equation (4-78) shows that $c(x,t) = c(x) . c(t)$, one may again make the identification that

$$c(x) = \xi_d D(x) \tag{4-24}$$

to give finally, $\dfrac{dc}{dt} + k_1 c = \xi_n g(t)$. $\hspace{2cm}$ (4-80)

This is a differential equation of the form

$$\frac{dc}{dt} + p(t)c = q(t) \qquad (4-81)$$

where $p(t) = k_1$ $\qquad (4-82)$

$$q(t) = \xi_n g(t) \qquad (4-83)$$

and has the solution,

$$c = \frac{\int \mu(t) \ q(t) \ dt + c'}{\mu(t)} \qquad (4-84)$$

where the integrating factor $\mu(t) = \exp\{\int p(t) \ dt\}$. $\qquad (4-85)$

In this case, $p(t) = k_1$, therefore

$$\mu(t) = \exp \{ \int k_1 dt \} = e^{k_1 t} \qquad (4-86)$$

and consequently,

$$c(t) = \frac{\int e^{k_1 t} \ q(t) \ dt + c'}{e^{k_1 t}} \qquad (4-87)$$

The two different pulse shapes will now be considered.

Case I, a(ii).

For $q(t) = \xi_n g(t)$ choose $\xi_n g(t) = \xi_n \sin \frac{\pi}{b} t$, and $\qquad (4-42)$

then

$$c(t) = \frac{\int e^{k_1 t} \ \xi_n \ \sin \frac{\pi}{b} \ dt + c'}{e^{k_1 t}} \qquad (4-88)$$

Integration by parts gives,

$$\int \sin \frac{\pi}{b} t \ e^{k_1 t} \ dt = \frac{e^{k_1 t} (k_1 \sin \frac{\pi}{b} t - \frac{\pi}{b} \cos \frac{\pi}{b} t)}{k_1^2 + \{\frac{\pi}{b}\}^2} \qquad (4-89)$$

so that

$$c(t) = \left\{ \frac{\xi_n e^{k_1 t} (k_1 \sin \frac{\pi}{b} t - \frac{\pi}{b} \cos \frac{\pi}{b} t)}{k_1^2 + \{\frac{\pi}{b}\}^2} + c' \right\} e^{-k_1 t} \qquad (4\text{-}90)$$

When $t = 0$, $c = 0$ since $D(t) = 0$ at $t = 0$, therefore

$$0 = \frac{-\frac{\pi}{b} \xi_n}{k_1^2 + \{\frac{\pi}{b}\}^2} + c' \quad \text{and} \qquad (4\text{-}91)$$

$$c' = \frac{\xi_n \frac{\pi}{b}}{k_1^2 + \{\frac{\pi}{b}\}^2} \qquad (4\text{-}92)$$

Combining equations (4-92) and (4-90)

$$c(t) = \frac{\xi_n}{k_1^2 + \{\frac{\pi}{b}\}^2} \left\{ k_1 \sin \frac{\pi}{b} t - \frac{\pi}{b} t - \frac{\pi}{b} \cos \frac{\pi}{b} t + \frac{\pi}{b} e^{-k_1 t} \right\} (4\text{-}93)$$

Since $c(x,t) = c(x) \cdot c(t)$, $\qquad\qquad\qquad (4\text{-}22)$

$$c(x,t) = \frac{\xi_n \xi_d D(x)}{k_1^2 + \{\frac{\pi}{b}\}^2} \left\{ k_1 \sin \frac{\pi}{b} t - \frac{\pi}{b} \cos \frac{\pi}{b} t + \frac{\pi}{b} e^{-k_1 t} \right\} \qquad (4\text{-}94)$$

Returning to equation (4-14),

$$OD(t) = \epsilon \int_o^{a_d} c(x,t) \, dx \qquad (4\text{-}14)$$

and substituting into (4-94)

$$OD(t) = \left\{ \frac{\epsilon \xi_n \xi_d}{k_1^2 + \{\frac{\pi}{b}\}^2} \right\} \left\{ k_1 \sin \frac{\pi}{b} t - \frac{\pi}{b} \cos \frac{\pi}{b} t + \frac{\pi}{b} e^{-k_1 t} \right\} \int_o^{a_d} D(x) \, dx \ (4\text{-}95)$$

For purposes of brevity define

$$F(t) = \frac{1}{k_1^2 + \left\{\frac{\pi}{b}\right\}^2} \left\{k_1 \sin \frac{\pi}{b} t - \frac{\pi}{b} \cos \frac{\pi}{b} t + \frac{\pi}{b} e^{-k_1 t}\right\} \qquad (4\text{-}96)$$

so that

$$OD(t) = \varepsilon\, \xi_n\, F(t)\, \xi_d \int_0^{a_d} D(x)\, dx \qquad (4\text{-}97)$$

From equation (4-30),

$$\int_0^{a_d} D(x)\, dx = E_o \cdot a_d, \text{ therefore} \qquad (4\text{-}30)$$

$$OD(t) = \varepsilon\, \xi_n\, \xi_d\, E_o \cdot a_d\, F(t) \qquad (4\text{-}98)$$

As in case I, a(i) $\quad \xi_n = I_q/Q$ $\hspace{3cm}$ (4-35)

$$OD(t) = \varepsilon\, \xi_d\, E_o \cdot a_d\, \frac{I_q}{Q}\, F(t) \qquad (4\text{-}99)$$

and $\quad E_o\, I_q = \dfrac{D_A}{a_d \cdot \rho}$ $\hspace{4cm}$ (4-38)

$$\xi_d = \frac{10\rho G}{N_o} \qquad (4\text{-}39)$$

so that

$$OD(t) = \frac{\varepsilon\ 10\ \rho\ G\ D_A}{N_o\ a_d \cdot \rho} \quad a_d \quad \frac{F(t)}{2b}$$

$$= 10\ \frac{G\ \varepsilon}{N_o}\ (D_A)\left(\frac{\pi}{2b}\right)\ F(t) \qquad (4\text{-}100)$$

$$OD(t) = \frac{10\ G\ \varepsilon}{N_o}\ (D_A)\frac{\pi}{2b} \left\{\frac{1}{k_1^2 + \left\{\frac{\pi}{b}\right\}^2}\right\} \left\{k_1 \sin \frac{\pi}{b} t - \frac{\pi}{b} \cos \frac{\pi}{b} t + \frac{\pi}{b} e^{-k_1 t}\right\}$$

$$(4\text{-}101)$$

Define $\quad \Phi_o = \dfrac{10\,G\,\epsilon}{N_o}\,(D_A)$ (4-102)

$B = \left(\dfrac{\pi}{2b}\right)\dfrac{1}{k_1^2 + \left\{\dfrac{\pi}{b}\right\}^2}$ (4-103)

$G(t) = k_1\,\sin\dfrac{\pi}{b}\,t - \dfrac{\pi}{b}\cos\dfrac{\pi}{b}\,t + \dfrac{\pi}{b}\,e^{-k_1 t}$ (4-104)

Recalling that one requires $I_t(t)$, substituting (4-102), (4-103) and (4-104) into equation (4-11),

$I_t(t) = I_o(t)\,\exp\,\{-2.303\,\Phi_o\,B\,G(t)\}$ (4-105)

as in the Case I, a(i)

$I_o(t) = \xi_n\,g(t) = \xi_n\,\sin\dfrac{\pi}{b}\,t$ (4-49)

so that

$I_t(t) = \xi_n\,g(t)\,\exp\,\{-2.303\,\Phi_o\,B\,(k_1\,\sin\dfrac{\pi}{b}\,t - \dfrac{\pi}{b}\cos\dfrac{\pi}{b}\,t + \dfrac{\pi}{b}\,e^{-k_1 t}\,)\}$

(4-106)

Equations (4-106) and (4-49) are then substituted into (4)

$U = \log_{10}\dfrac{\displaystyle\int_o^{\tau_p} I_o(t)\,dt}{\displaystyle\int_o^{\tau_p} I_t(t)\,dt}$ (4-4)

to yield

$U = \log_{10}\left[\dfrac{\displaystyle\int_o^{b} \xi_n\,\sin\dfrac{\pi}{b}\,t\,dt}{\displaystyle\int_o^{b} \xi_n\,\sin\dfrac{\pi}{b}\,t\,\exp\,\{-\,\Phi_o\,B\,(k_1\,\sin\dfrac{\pi}{b}\,t - \dfrac{\pi}{b}\cos\dfrac{\pi}{b}\,t + \dfrac{\pi}{b}\,e^{-k_1 t}\,)\}dt}\right]$

(4-107)

in which Φ_o and B are defined as above so that

$$\Phi_o B = \left(\frac{23.03 \, D_A}{N_o}\right)\left(\frac{\pi}{2b}\right)\left\{\frac{1}{k_1^2 + \left\{\frac{\pi}{b}\right\}^2}\right\} G \epsilon \qquad (4\text{-}108)$$

This equation cannot be reduced to an explicit expression for $G \epsilon$, because of the integral in the denominator. Before proceeding with further approximations or numerical integration of equation (107), the triangular pulse shape (Case II) will be studied in the hope that it might yield a more tractable expression.

Case II, a(ii)

Choose $q(t) = \xi_n t \qquad\qquad 0 \leqslant t \leqslant \frac{b}{2} \qquad (4\text{-}109)$

$\qquad\qquad = \xi_n(b - t) \qquad\qquad \frac{b}{2} \leqslant t \leqslant b \qquad (4\text{-}110)$

then for $0 \leqslant t \leqslant \frac{b}{2}$ one has from equation (4-87)

$$c_1(t) = \frac{\int e^{k_1 t} \, \xi_n t \, dt + c'}{e^{k_1 t}} \quad, \; 0 \leqslant t \leqslant \frac{b}{2} \qquad (4\text{-}111)$$

alternatively

$$c_2(t) = \frac{\int e^{k_1 t} \, \xi_n (b - t) \, dt + c''}{e^{k_1 t}} \quad, \; \frac{b}{2} \leqslant t \leqslant b \qquad (4\text{-}112)$$

where $c_2\left(\frac{b}{2}\right) = c_1\left(\frac{b}{2}\right)$ and $c_1(0) = 0$, since $D(0) = 0$.

Treating (4-111) first, integration by parts gives

$$\xi_n \int t \, e^{k_1 t} \, dt = \frac{\xi_n}{k_1^2} (k_1 t - 1) \, e^{k_1 t} \qquad (4\text{-}113)$$

Therefore

$$c_I(t) = \frac{\frac{\xi_n}{k_1^2}(k_1 t - 1)e^{k_1 t} + c'}{e^{k_1 t}} \qquad 0 \leqslant t \leqslant \frac{b}{2} \qquad (4\text{-}114)$$

When $t = 0$, $c(t) = 0$ since $D(t) = 0$ at $t = 0$,

$$0 = \frac{\xi_n}{k_1^2}(-1) + c' \qquad (4\text{-}115)$$

so that finally one has:

$$c_1(t) = \frac{\xi_n}{k_1^2}(k_1 t - 1 + e^{-k_1 t}) \qquad 0 \leqslant t \leqslant \frac{b}{2} \qquad (4\text{-}116)$$

Considering equation (4-112) next (i.e. $\frac{b}{2} \leqslant t \leqslant b$),

$$c_2(t) = \left\{ \xi_n\left[\frac{b}{k_1}e^{-k_1 t} - \frac{1}{k_1^2}(k_1 t - 1)e^{k_1 t}\right] + c'' \right\} e^{-k_1 t} \qquad (4\text{-}117)$$

In order to evaluate c'', one makes use of the fact that when $t = \frac{b}{2}$ equations (4-115) and (4-117) must be equal:

$$c_1\left(\frac{b}{2}\right) = c_2\left(\frac{b}{2}\right) \qquad (4\text{-}118)$$

$$c_1\left(\frac{b}{2}\right) = \frac{\xi_n}{k_1^2}(k_1\frac{b}{2} - 1 + e^{-k_1\frac{b}{2}}) \qquad (4\text{-}119)$$

$$c_2\left(\frac{b}{2}\right) = \left\{ \xi_n\left[\frac{b}{k_1}e^{k_1\frac{b}{2}} - \frac{1}{k_1^2}(k_1\frac{b}{2} - 1)e^{k_1\frac{b}{2}}\right] + c'' \right\} e^{-k_1\frac{b}{2}}$$

$$= \frac{\xi_n}{k_1}\left[b - \frac{1}{k_1}(k_1\frac{b}{2} - 1)\right] + c'' e^{-k_1\frac{b}{2}} \qquad (4\text{-}120)$$

Combining equations (4-118) and (4-117), one has that

$$\frac{\xi_n}{k_1^2} \left(k_1 \frac{b}{2} - 1 + e^{-k_1 \frac{b}{2}}\right) = \frac{\xi_n}{k_1} \left[b - \frac{1}{k_1} \left(k_1 \frac{b}{2} - 1\right)\right] + c'' \, e^{-k_1 \frac{b}{2}} \qquad (4\text{-}121)$$

$$\frac{\xi_n}{k_1} \frac{b}{2} - \frac{\xi_n}{k_1^2} + \frac{\xi_n}{k_1^2} e^{-k_1 \frac{b}{2}} - \frac{\xi_n}{k_1} b + \frac{\xi_n}{k_1} \frac{b}{2} - \frac{\xi_n}{k_1^2} = c'' \, e^{-k_1 \frac{b}{2}} \qquad (4\text{-}122)$$

Thus, $$\frac{\xi_n}{k_1^2} \left(e^{-k_1 \frac{b}{2}} - 2\right) = c'' \, e^{-k_1 \frac{b}{2}} \qquad (4\text{-}123)$$

$$c'' = \frac{\xi_n}{k_1^2} \left(1 - 2 e^{k_1 \frac{b}{2}}\right) \qquad (4\text{-}124)$$

On substituting equation (4-124) into (4-117),

$$c_2(t) = \frac{\xi_n}{k_1} \left\{ \left(b - t + \frac{1}{k_1}\right) + \frac{1}{k_1} \left(1 - 2 e^{k_1 \frac{b}{2}}\right) e^{-k_1 t} \right\} \qquad (4\text{-}125)$$

$$c_1(t) = \frac{\xi_n}{k_1} \left\{ t - \frac{1}{k_1} + \frac{1}{k_1} e^{-k_1 t} \right\} \qquad (4\text{-}116)$$

since $c(x,t) = c(x) \cdot c(t)$, $\qquad\qquad (4\text{-}22)$

$$c(x,t) = \frac{\xi_n \, \xi_d}{k_1} D(x) \left\{ \left(b - t + \frac{1}{k_1}\right) + \frac{1}{k_1} \left(1 - 2 e^{k_1 \frac{b}{2}}\right) e^{-k_1 t} \right\} \qquad (4\text{-}126)$$

$$\text{for } \frac{b}{2} \leqslant t \leqslant b;$$

and $$= \frac{\xi_n \, \xi_d}{k_1} D(x) \left\{ \left(t - \frac{1}{k_1} + \frac{1}{k_1} e^{-k_1 t}\right) \right\} \text{ for } 0 \leqslant t \leqslant \frac{b}{2} \qquad (4\text{-}127)$$

Define $c_1(t) \cdot \dfrac{k_1}{\xi_n} = f_1(t)$ (4-128)

$c_2(t) \cdot \dfrac{k_1}{\xi_n} = f_2(t)$ (4-129)

Then, $c(x,t) = \xi_n \xi_d \dfrac{D(x)}{k_1} f_i(t)$, $i = 1$ for $0 \leqslant t \leqslant \dfrac{b}{2}$

$i = 2$ for $\dfrac{b}{2} \leqslant t \leqslant b$. (4-130)

Returning to equation (4-14)

$$OD(t) = \varepsilon \int_o^{a_d} c(x,t)dx$$ (4-14)

and substituting equation (4-128)

$$OD(t) = \dfrac{\xi_n}{k_1} \varepsilon f_i(t) \int_o^{a_d} \xi_d D(x)dx$$ (4-131)

since:

$$\int_o^{a_d} D(x) \, dx = E_o \cdot a_d$$ (4-30)

$$OD(t) = \xi_n \dfrac{\xi_d}{k_1} \varepsilon E_o \cdot a_d f_i(t)$$ (4-132)

Once again, as in Case II, a(i), $\xi_n = I_q/Q$ therefore, (4-35)

$$OD(t) = \varepsilon \dfrac{\xi_d}{k_1} E_o \cdot a_d \dfrac{I_q}{Q} f_i(t)$$ (4-133)

Making the further substitutions $E_o I_q = D_A/a_d \cdot \rho$ and $\xi_d = 10 \rho G/N_o$, from equations (4-38) and (4-39) respectively, one obtains:

$$OD(t) = \frac{\varepsilon}{k_1} \, 10 \, \frac{\rho \, G}{N_o} \, (D_A \frac{1}{a_d \cdot \rho}) \, a_d \frac{4}{b^2} \, f_i(t) \qquad (4\text{-}134)$$

Let $\quad 40 \, \dfrac{G \, \varepsilon \, D_A}{N_o} = T_1 \qquad\qquad (4\text{-}135)$

Then,

$$OD(t) = \frac{T_1}{k_1 b^2} \, (t - \frac{1}{k_1} + \frac{1}{k_1} e^{-k_1 t}) \; , \quad 0 \leqslant t \leqslant \frac{b}{2} \qquad (4\text{-}136)$$

$$= \frac{T_1}{k_1 b^2} \, (b - t + \frac{1}{k_1}) + \frac{1}{k_1} (1 - 2 \, e^{k_1 \frac{b}{2}}) \, e^{-k_1 t} \qquad (4\text{-}137)$$

$$\text{for } \frac{b}{2} \leqslant t \leqslant b$$

Now, one requires $\displaystyle\int_o^b I_t(t) dt$,

$$\int_o^b I_t(t) dt = I_t(0 \leqslant t \leqslant \frac{b}{2}) + I_t(\frac{b}{2} \leqslant t \leqslant b) \qquad (4\text{-}138)$$

recalling that,

$$I_t(t) = I_o(t) \, \exp \, (-2.303 \, OD(t)) \qquad (4\text{-}11)$$

consider the contribution from $I_t(1)$ for $0 \leqslant t \leqslant \frac{b}{2}$ first:

$$I_t(1) = \int_o^{\frac{b}{2}} \lambda \, \xi_n \, t \, \exp \, \frac{(-2.303 \, T_1 \, f_1(t))}{k_1 b^2} \, dt \qquad (4\text{-}139)$$

while that from $I_t(2)$ for $\frac{b}{2} \leqslant t \leqslant b$,

$$I_t(2) = \int_{\frac{b}{2}}^{b} \lambda \, \xi_n \, (b - t) \, \exp \frac{(-2.303 \, T_1 \, f_2(t))}{k_1 b^2} dt \qquad (4\text{-}140)$$

Thus substituting into equation (4-4)

$$U = \log_{10} \frac{\int_{o}^{b} I_o(t)dt}{\int_{o}^{b} I_t(t)dt} \quad , \quad = \qquad (4\text{-}4)$$

$$\log_{10} \frac{\int_{o}^{\frac{b}{2}} \lambda \, \xi_n \, t \, dt + \int_{\frac{b}{2}}^{b} \lambda \, \xi_n \, (b - t)dt}{\int_{o}^{\frac{b}{2}} \lambda \, \xi_n \, t \, \exp \left(\frac{-2.303 \, T_1}{k_1 b^2} f_1(t) \right)dt + \int_{\frac{b}{2}}^{b} \lambda \, \xi_n (b - t) \, \exp \left(\frac{-2.303 \, T_1}{k_1 b^2} f_2(t) \right)dt} \qquad (4\text{-}141)$$

Finally substituting for $f_1(t)$ and $f_2(t)$ one obtains for the absorbance U

$$U = \log_{10} \left[\frac{\lambda \, \xi_n \left\{ \int_{o}^{\frac{b}{2}} t \, dt + \int_{\frac{b}{2}}^{b} (b - t)dt \right\}}{\lambda \, \xi_n \left\{ \int_{o}^{\frac{b}{2}} t \, \exp \left(-2.303 \, T_1 \left\{ t - \frac{1}{k_1} + \frac{1}{k_1} e^{-k_1 t} \right\} \right)dt + \int_{\frac{b}{2}}^{b} (b - t) \right.} \right. \qquad (4\text{-}142)$$

$$\left. \exp \left(\frac{-2.303 \, T_1}{k_1 b^2} \left\{ b - t + \frac{1}{k_1} + \frac{1}{k_1} (1 - 2e^{k_1 \frac{b}{2}}) e^{-k_1 t} \right\} \right) \right.$$

Again one is faced with the problem of the intractable integrals in the denominator, for which an analytical evaluation seems impossible. There are two choices, approximation or numerical integration. The latter is quite straight forward, so that the expression from equation (4-107) was numerically integrated by Simpson's rule on the IBM Duplex 360/67 computer for a range of k_1. The critical parameter in this calculation is the pulse width b, as shown in fig. 4-2, especially for high values of $k_1 > 10^9$ sec^{-1}.

The best measurement of the pulse shape comes from the Faraday cup waveform (see fig. 3-1(c)), which is proportional to the electron flux as a function of time. As mentioned previously*, from this measurement one may obtain the energy-time function and the dose rate function (see figs. 3-1(c) and 3-3(a), respectively). Under the monoenergetic approximation, the electron flux and thus the Cerenkov light flux is directly proportional to the current function, but in these calculations it is worth compensating for some of the inadequacies in the monoenergetic approximation by taking the value for the pulse duration b as 4 nanoseconds, based on the observed dose rate function (figure 3-3(a)), rather than on the wider (6 nanoseconds) current waveform (fig. 3-1(c)). This is the most logical choice under the circumstances since the Cerenkov light pulse is significantly narrower than the current pulse because of the Cerenkov threshold energy in water at 265 KeV.

The next step is to consider a dose rate pulse and a Cerenkov radiation pulse of different durations. Using the same dose function as Case II, a(ii),

$$q(t) = \xi_n \sin \frac{\pi}{b} t \qquad (4-42)$$

---

* see page 51
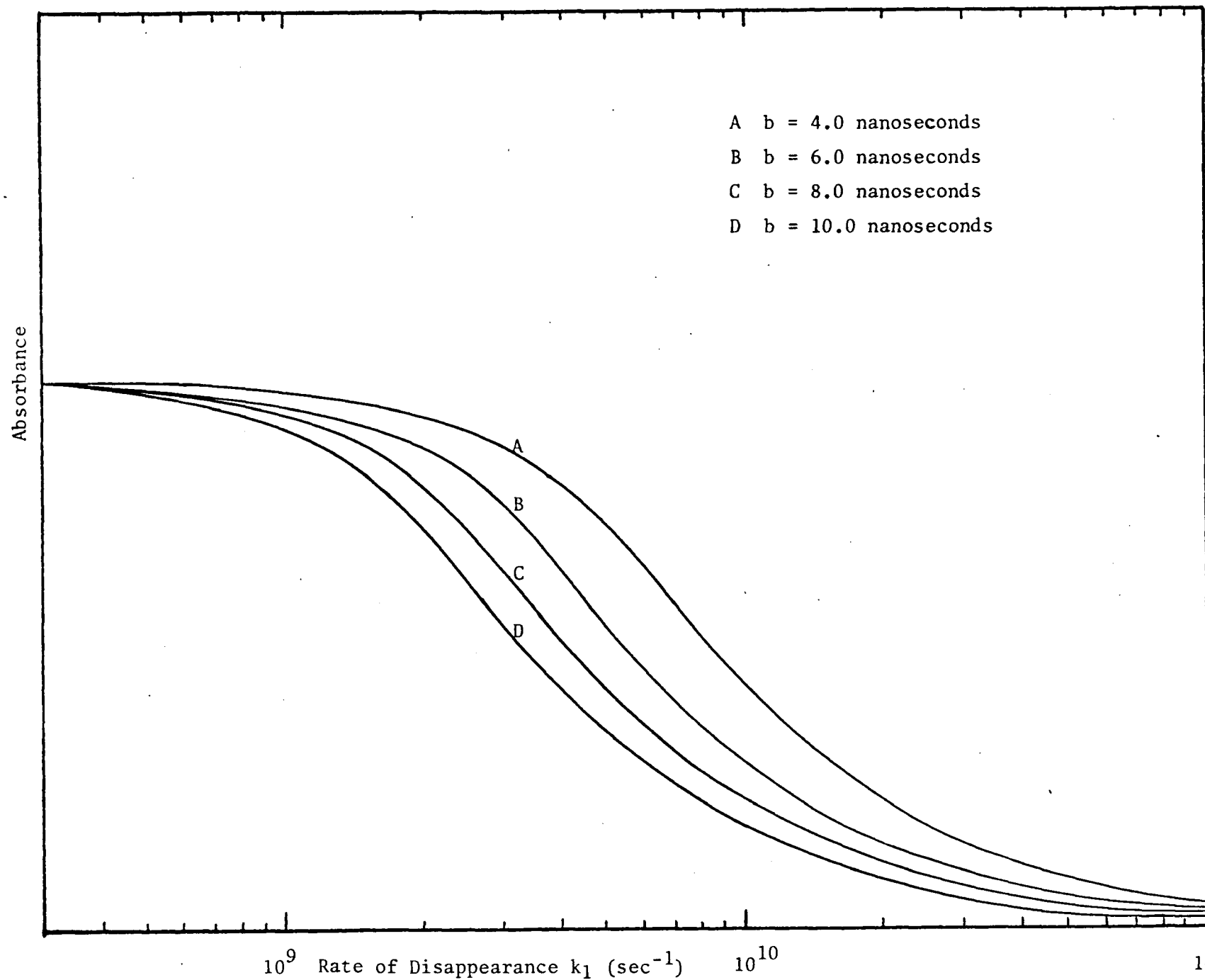
Figure 4-2   The effect of differing electron pulse lengths on the absorbance, calculated from the "monoenergetic" approximation.

one has already that:

$$OD(t) = \frac{10\ G\ \epsilon}{N_o}\ D_A\ \left(\frac{\pi}{2b}\right)\ \left(\frac{1}{(k_1^{\ 2} + \{\frac{\pi}{b}\}^2)}\right)\ \left\{ k_1 \sin \frac{\pi}{b}\ t - \frac{\pi}{b} \cos \frac{\pi}{b}\ t + \frac{\pi}{b}\ e^{-k_1 t} \right\} \quad (4\text{-}101)$$

Then, defining a Cerenkov pulse function $P(t')$,

$$P(t') = \Lambda\ \sin \frac{\pi}{c}\ t' \quad\quad\quad (4\text{-}143)$$

where c is the pulse duration and Λ is a constant. One has the following relationship between the two times t and t'

$$t = t' + \frac{b}{2} - \frac{c}{2}$$

so that substituting into (4-101)

$$I_t(t') = \Lambda \sin \frac{\pi}{c}\ t'\ \exp \left\{ -2.303\ \Phi\ B\{ k_1 \sin \frac{\pi}{b}\ (t' + \frac{b}{2} - \frac{c}{2}) - \frac{\pi}{b} \cos \frac{\pi}{b}\ (t' + \frac{b}{2} - \frac{c}{2}) \right.$$

$$\left. + \frac{\pi}{b}\ e^{-k_1(t' + \frac{b}{2} - \frac{c}{2})} \}\right\} \quad\quad (4\text{-}145)$$

and with $I_o(t') = \Lambda \sin \frac{\pi}{c}\ t'$, one has

$$U = \log_{10} \frac{\displaystyle\int_o^c \Lambda \sin \frac{\pi}{c}\ t'\ dt'}{\displaystyle\int_o^c \Lambda \sin \frac{\pi}{c}\ t'\ \exp (\quad)\ dt'} \quad\quad (4\text{-}146)$$

where the term in brackets ( ) is

$$(\quad) = \left\{ -2.303\ \Phi\ B\{ k_1 \sin \frac{\pi}{b}\ (t' + \frac{b}{2} - \frac{c}{2}) - \frac{\pi}{b} \cos \frac{\pi}{b}\ (t' + \frac{b}{2} - \frac{c}{2}) + \frac{\pi}{b}\ e^{-k_1(t' + \frac{b}{2} -} \right.$$

$$(4\text{-}147)$$

Finally the case is considered for species with very short lifetimes.

(iii) Lifetime of absorbing species very much less than pulse length, $\tau \ll \tau_p$. Case II, a(iii) for the triangular pulse shape.

One has already derived an expression for $I_t(t)$ in Case II, a(ii);

$$I_t(t) = \lambda \, \xi_n t \, \exp \, \{-\frac{2.303 \, T_1}{k_1 b^2}(t - \frac{1}{k_1} + \frac{1}{k_1} e^{-k_1 t})\}, \; 0 \leqslant t \leqslant \frac{b}{2} \qquad (4\text{-}139)$$

$$\text{and} \quad I_t(t) = \lambda \, \xi_n (b - t) \, \exp \, \{-\frac{2.303 \, T_1}{k_1 b^2}(b - t + \frac{1}{k_1}) + \frac{1}{k_1}(1 - 2 \, e^{k_1 \frac{b}{2}}) \, e^{-k_1 t}\}$$

$$\text{for } \frac{b}{2} \leqslant t \leqslant b. \qquad (4\text{-}140)$$

As k_1 gets very large, of the order 5×10^{10} sec^{-1}, these expressions reduce to the following:

$$I_t(t) = \lambda \, \xi_n \, t \, \exp \, \{-\frac{2.303 \, T_1}{k_1 b^2} \, t\} \qquad 0 \leqslant t \leqslant \frac{b}{2} \qquad (4\text{-}148)$$

$$I_t(t) = \lambda \, \xi_n \, (b - t) \, \exp \, \{-\frac{2.303 \, T_1}{k_1 b^2} \, (b - t)\}, \frac{b}{2} \leqslant t \leqslant b \qquad (4\text{-}149)$$

These equations are consistent with a steady state condition, in that at these fast decay rates there is no growth of absorption. Consequently

$$c(t) \propto \frac{\text{Dose rate}}{k_1} \qquad \text{and thus} \qquad (4\text{-}150)$$

$$OD(t) \propto \frac{\text{Dose rate}}{k_1} \qquad (4\text{-}151)$$

Substituting equation (4-148) and (4-149) into equation (4-4)

$$U = \log_{10} \frac{\displaystyle\int_o^b I_o(t)\ dt}{\displaystyle\int_o^b I_t(t)\ dt} \qquad\qquad (4-4)$$

results in the final expression,

$$U = \log_{10} \frac{\lambda\ \xi_n \left[\displaystyle\int_o^{\frac{b}{2}} t\ dt + \int_{\frac{b}{2}}^b (b-t)\ dt\right]}{\lambda\ \xi_n \left[\displaystyle\int_o^{\frac{b}{2}} t\ \exp\ \{\frac{-2.303}{k_1 b^2}\ T_1\ t\}\ dt + \int_{\frac{b}{2}}^b (b-t)\ \exp\ \{\frac{-2.303}{k_1 b^2}\ T_1\ (b-t)\}\ dt\right]} \qquad (4-152)$$

This equation is evaluated in Appendix C, and the result is:

$$U = \log_{10} \left\{ \frac{46.06\ G\ \epsilon\ D_A}{k_1\ b\ N_o} \left(1 - \exp\ \left\{\frac{-46.06\ G\ \epsilon\ D_A}{k_1\ b\ N_o}\right\}\right)^{-1} \right\} \qquad (4-153)$$

for $k_1 \geqslant 5 \times 10^{10}\ \text{sec}^{-1}$

A similar treatment of the sine function pulse shape may be made as follows.

Case I, a(iii).

From equation (4-107) one has for $I_t(t)$:

$$I_t(t) = \lambda\ \xi_n\ \sin\frac{\pi}{b}\ t\ \exp\ \{- \Phi\ \frac{\pi}{2b}\ (\frac{1}{k_1^2 + \{\frac{\pi}{b}\}^2}\ [k_1\ \sin\frac{\pi}{b}\ t - \frac{\pi}{b}\ \cos\frac{\pi}{b}\ t + \frac{\pi}{b}\ e^{-k_1 t}\ ]\}$$

$$\qquad (4-107)$$

As k_1 increases, the dominant term in the exponential is $k_1 \sin \frac{\pi}{b} t$ since for $k_1 > 10^{10}$, k_1 is much larger than $\frac{\pi}{b}$. This yields

$$I_t(t) = \lambda \, \xi_n \sin \frac{\pi}{b} t \, \exp \left\{ - \phi \, \frac{\pi}{2b} \, \frac{1}{k_1} \, \sin \frac{\pi}{b} t \right\} \tag{4-154}$$

However, since $\sin t \exp (a \sin t)$ is not an integrable function this treatment could not be pursued.

(2) Spectrophotometric Detection.

In contrast to spectrographic measurements, spectrophotometric detection techniques yield data which are directly proportional to the incident light flux. With a sufficiently high frequency spectrophotometric detector it is possible to make comparisons of such dynamic variables as relative peak heights, thus eliminating some of the experimental problems of measuring the total integrated light emission per Cerenkov pulse. The following discussion assumes that all pulse measurements are made with adequately fast spectrophotometric equipment, so that effects due to pulse distortion can be omitted from the calculations. Such a drastic step is necessary because of uncertainities in both the measurements of experimental frequency response and the ensuing calculation of real pulse shapes from this data. Thus a qualitative estimate of the range of validity of these kind of measurements can only be made in conjunction with later experimental results.

(a) Relative Peak Areas.

Because of the linear response of these photometric techniques the direct comparison of peak areas may be made. However, all necessary

equations have been derived in section (1) from which only the

logarithm need be removed. Thus one may define:

$$S = \frac{I_o}{I_t} \qquad \text{where} \qquad \text{(4-155)}$$

$$I_o = \int_o^{\tau_p} I_o(t) \, dt \qquad \text{(4-2)}$$

$$I_t = \int_o^{\tau_p} I_t(t) \, dt \qquad \text{(4-3)}$$

The results for the three temporal categories are:

    (i) For Cases I a(i) and II a(i) the sinusoidal and triangular

pulse shapes, the lifetime of the absorbing species being very much

longer than the duration of the pulse, one obtains from

$$U = \log_{10} \left(23.0 \, \frac{G \, \epsilon \, D_A}{N_o}\right) \qquad \text{that} \qquad \text{(4-52)}$$

$$S = 23.0 \, \frac{G \, \epsilon \, D_A}{N_o} \qquad \text{(4-156)}$$

    (ii) Since removal of the logarithm does not result in any

improvement regarding the insoluble equations for U in Case Ia(ii) and

II a(ii) where the lifetime of the absorbing species and the pulse

duration are similar, there is no point in rewriting equations (4-107)

and (4-142) which must be evaluated numerically.

(iii) Finally, when the lifetime of the absorbing species is very much less than the electron pulse duration, one has from equation (4-153), Case II a(iii).

$$ S = \left(\frac{46.1 \ G\epsilon \ D_A}{b \ k_1 \ N_o} \right) \cdot \left(1 - \exp\left\{ \frac{46.1 \ G\epsilon \ D_A}{k_1 \ b \ N_o} \right\} \right)^{-1} \quad (4\text{-}15 $$

(b)   Relative Peak Heights

Since spectrophotometric measurements give the complete Cerenkov light pulse shape, a further experimental observable will be the ratio of the peak heights with and without Cerenkov reabsorption. This ratio can be calculated analytically directly from the equations for $I_o(t)$ and $I_t(t)$ in section 1. The following treatment will only consider Case II, the triangular pulse shape, because the sinusoidal pulse shape of Case I inevitably leads to insoluble equations for the value of t for which $I_t(t)$ is a maximum.

(i) The lifetime of the absorbing species is very much greater than the electron pulse length τ_p.

The expressions for $I_o(t)$ and $I_t(t)$ are from section 1:

$$ I_o(t) = \lambda \ \xi_n \ t \qquad\qquad 0 < t < \frac{b}{2} \qquad\qquad (4\text{-}72) $$

$$ I_t(t) = \lambda \ \xi_n \ t \exp(-2.303 \ T_o \ t^2), \ 0 < t < \frac{b}{2} \qquad (4\text{-}70) $$

The unabsorbed Cerenkov light clearly has its maximum at $t = \frac{b}{2}$, $I_o\left(\frac{b}{2}\right) = \lambda \ \xi_n \ b$, so that $I_t(t)$ must have its maximum for $t < \frac{b}{2}$.

Thus only the expression for $I_t(t)$ in the range $0 < t < \frac{b}{2}$ is required. The function $I_t(t)$ will be maximised for t such that $\frac{d}{dt}(I_t(t)) = 0$.

$$\frac{d}{dt} I_t(t) = (\lambda \, \xi_n \, t)(\exp \, \{-2.303 \, T_o t^2\})(-4.606 \, T_o t) + \exp \, \{-2.303 \, T_o t^2\} \, \lambda \, \xi_n \tag{4-158}$$

Then equating $\frac{dI}{dt} = 0$ and simplifying one has

$$-4.606 \, T_o t^2 + 1 = 0 \tag{4-159}$$

$$t^2 = \frac{1}{4.606 \, T_o} \quad \text{or} \quad t = (4.606 \, T_o)^{-\frac{1}{2}} \tag{4-160}$$

Finally substituting into equation (4-70),

$$I_t(t_{max}) = \lambda \, \xi_n \, (4.606 \, T_o)^{-\frac{1}{2}} \exp \, \{-2.303 \, T_o \, (\frac{1}{4.606 \, T_o})\}$$

$$= \lambda \, \xi_n \, (4.606 \, T_o)^{-\frac{1}{2}} e^{-\frac{1}{2}} \tag{4-161}$$

Then defining H as the ratio of peak heights for I_o and I_t,

$$H = \frac{I_o(t_{max})}{I_t(t_{max})} \tag{4-162}$$

and substituting for T_o in equation (4-160)

$$T_o = \frac{4}{b^2} \, (\frac{5 \, G \, \epsilon \, D_A}{N_o}) \tag{4-68}$$

$$H = 1.649 \, \left\{ \frac{23.03 \, G \, \epsilon}{N_o} \, D_A \right\}^{\frac{1}{2}} \tag{4-163}$$

(ii) The lifetime of the absorbing species, τ, is short enough for significant numbers to disappear during the electron pulse τ_p.

The relevant expressions for $I_o(t)$ and $I_t(t)$ are:

$$I_o(t) = \lambda \, \xi_n \, t \qquad\qquad 0 \leqslant t \leqslant \frac{b}{2} \tag{4-72}$$

$$I_t(t) = \lambda \, \xi_n \, t \, \exp \, \left\{ \frac{-2.303}{k_1 b^2} \, T_1 \, (t - \frac{1}{k_1} + \frac{1}{k_1} e^{-k_1 t}) \right\} \tag{4-136}$$

Then, differentiating equation (4-136) and setting it equal to zero, one has:

$$-2.303 \, T_1 \, t(1 - e^{-k_1 t}) + 1 = 0 \tag{4-164}$$

so that

$$t(1 - e^{-k_1 t}) = \frac{k_1 b^2}{2.303 \, T_1} \tag{4-165}$$

This equation is insoluble unless $e^{-k_1 t} \ll 1$, so that for $k_1 > 10^{11}$ sec^{-1}

and,

$$t_{max} \sim \frac{k_1 b^2}{2.303 \, T_1} . \tag{4-166}$$

Substituting this value of t into equation (4-136) and considering only significant terms, one obtains:

$$H = \left\{ \frac{\lambda \, \xi_n \, \frac{b}{2}}{\frac{\lambda \, \xi_n k_1 b^2 \, e^{-1}}{2.303 \, T_1}} \right\} \qquad \text{where } T_1 = \frac{40 \, G \, \varepsilon \, D_A}{N_o}$$

$$= 46.06 \left\{ \frac{G \, \varepsilon}{N_o} \, D_A \, \frac{e}{b \, k_1} \right\} \tag{4-167}$$

However this result really belongs in category (iii), that is the case where the decay of the absorbing species is so fast that there is no concentration build-up during the electron pulse, but rather a small steady state concentration only because of the magnitude of k_1.

(iii) The lifetime of the absorbing species is very much less that

the duration of the electron pulse τ_p.

For a pseudo first-order rate constant of $k_1 > 5 \times 10^{10} \; sec^{-1}$,

equation (4-136) simplifies to:

$$I_t(t) = \lambda \, \xi_n \, \exp \left\{ \frac{-2.303 \; T_1}{k_1 b^2} \, t \right\} \qquad (4-148)$$

so that setting $\frac{d}{dt} I_t(t) = 0$ one obtains

$$t = \frac{k_1 b^2}{2.303 \; T_1} \qquad (4-166)$$

and, as in the previous section for $k_1 > 5 \times 10^{10} \; sec^{-1}$

$$H = 46.06 \left\{ \frac{G \, \varepsilon}{N_o} D_A \quad \frac{e}{b \; k_1} \right\} \qquad (4-167)$$

(3)   Corrections for the Spatial Distribution of Cerenkov Radiation.

A complete treatment of Cerenkov reabsorption must include the

spatial distribution of Cerenkov emission in the irradiated medium. This

is an extremely difficult undertaking, not only because of the complications

it adds to the model described in sections one and two, but also because

of the uncertainty in estimating the Cerenkov depth distribution function

itself. Although the theoretical framework for a complete calculation

of electron flux distributions and hence the Cerenkov emission as a

function of depth, exists within the Monte Carlo simulation method, because

of the complexities of such a calculation a much simpler (and less

satisfactory) procedure based on the Bethe equation was used. The results

of this calculation, superimposed on the measured depth-dose for 0.5 MeV

electrons in water (76) in fig. 4-3 illustrate the approximate magnitude

of the effect. A crude first order correction (designated approximation $\underline{b}$)

to approximation $\underline{a}$ used in section one and two, may be made by reducing

the energy density D_A by a factor δ related to the mean Cerenkov emission

depth $\bar{x}$ as follows:

$$\delta = 1 - \frac{\int_o^{\bar{x}} D(x)\ dx}{\int_o^{a_d} D(x)\ dx} \tag{4-168}$$

$$\text{where } \bar{x} = \frac{\int_o^{a_d} x\ N(x)\ dx}{\int_o^{a_d} N(x)\ dx} \tag{4-169}$$

and $N(x)$ = the Cerenkov depth distribution function.

This now accounts for the fact that not all Cerenkov radiation is

emitted at $x = 0$. Unfortunately because of the $\underline{ad\ hoc}$ nature of this

correction it is difficult to estimate its exact range of validity,

however, on qualitative arguments alone it should significantly

improve the calculation of the $G\ \epsilon$ product.

Finally, the spatial dependence of Cerenkov emission and dose

deposition will be explicitly included in the calculation (described

as approximation $\underline{c}$). In this case I will be a function of both x and t,

so that

$$I_t(x,t) = I_o(x,t)\ \exp\ \{-2.303 \int_x^{a_d} \epsilon\ c(x,t)\ dx\} \tag{4-170}$$
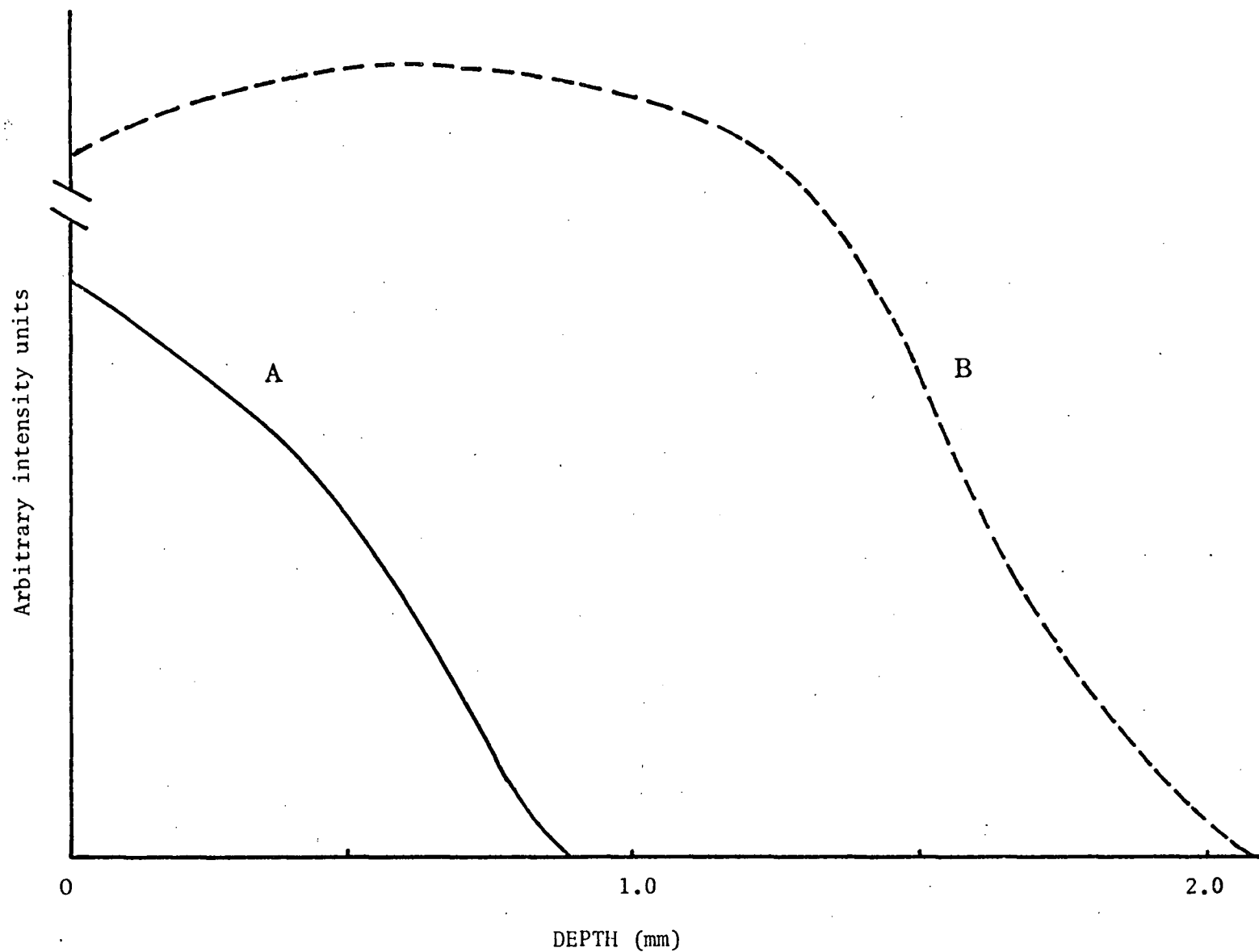
Figure 4-3 Approximate those depth and Cerenkov depth distributions in water obtained using the Febetron and the 5510 tube.

and

$$I_t(t) = \frac{1}{a_c} \int_0^{a_c} I_0(x,t) \ \exp \ \{-2.303 \int_x^{a_d} \varepsilon \ c(x,t) \ dx \ dx\} \qquad (4\text{-}171)$$

$$I_t = \int_0^{\tau_p} \frac{1}{a_c} \int_0^{a_c} I_0(x,t) \ \exp \ \{-2.303 \int_x^{a_d} \varepsilon \ c(x,t) \ dx\} \ dt \qquad (4\text{-}172)$$

$$I_0 = \int_0^{\tau_p} \frac{1}{a_c} \int_0^{a_c} I_0(x,t) \ dx \ dt \qquad (4\text{-}173)$$

and finally substituting into equation (4-4) for the absorbance U,

$$U = \log_{10} \left[\frac{\displaystyle\int_0^{\tau_p} \int_0^{a_c} I_0(x,t) \ dx \ dt}{\displaystyle\int_0^{\tau_p} \int_0^{a_c} I_0(x,t) \ \exp \ \{-\varepsilon \int c(x,t) \ dx\} \ dx \ dt} \right] \qquad (4\text{-}174)$$

First, what is c(k,t)?

Applying the monoenergetic approximation, and using the sinusoidal pulse shape, case I, including absorber decay by a first order reaction, one has already that

$$c(x,t) = \frac{\xi_n \xi_d \ D(x)}{k_1^2 + \{\frac{\pi}{b}\}^2} \left\{ k_1 \ \sin \frac{\pi}{b} t - \frac{\pi}{b} \cos \frac{\pi}{b} t + \frac{\pi}{b} e^{-k,t} \right\} \qquad (4\text{-}94)$$

However $D(x)$ must now be specified, since one requires an explicit expression for $\int_x^{a_d} c(x,t) \ dx$ in equation (4-174).

but $D(x) = D^*(x)$ (4-175)

where $D^*(x)$ is an empirical dose depth distribution function such that

$$\frac{1}{a_d} \int_o^{a_d} D^*(x)\, dx = \text{the total dose deposited by a single high}$$

$$\text{energy electron (eV g}^{-1})$$ (4-176)

recalling that

$$\xi_n = \frac{\pi}{2b} \text{ (no. of } e^- \text{ per pulse)} \qquad \xi_d = 10\,\frac{DG}{N_o}$$

the constants in (4-94) are equal to

$$\frac{10\,DG}{N_o} \quad \frac{\pi}{2b} \text{ (no. of } e^- \text{ per pulse)(} \frac{\text{total dose per } e^-}{\displaystyle\int_o^{a_d} D^*(x)\, dx}) a_d \quad \frac{1}{k_1^{\,2} + \{\frac{\pi}{b}\}^2}$$

where (no. of e^- per pulse) (total dose per e^-) $= \dfrac{DA}{a_d\,\rho}$ (4-38)

so that

$$c(x,t) = \frac{10\,G}{N_o} D_A \left\{ \frac{\pi}{2b} \right\} \left\{ \frac{1}{k_1^{\,2} + \{\frac{\pi}{b}\}^2} \right\} \left\{ \frac{1}{\displaystyle\int_o^{a_d} D^*(x)\, dx} \right\} D^*(x)\, \ell(t)$$ (4-177)

where $\ell(t) = k_1 \sin \frac{\pi}{b} t - \frac{\pi}{b} \cos \frac{\pi}{b} t + \frac{\pi}{b} e^{-k_1 t}$ (4-178)

Next choose as a function for $D^*(x)$ to agree with the empirical dose

depth data for water,

$$D^*(x) = c_1 \exp(-c_2 x) + c_3 \sin \frac{\pi}{c_4} (x + c_5)$$ (4-179)

$c_1 - c_5$ are constants

thus

$$\int_x^{a_d} D^*(x') \, dx' = \frac{c_1}{c_2} \left\{ e^{-c_2 x} - e^{-c_2 a_d} \right\} + \frac{c_3 c_4}{\pi} \left\{ \cos \frac{\pi}{c_4} (x + c_5) - \cos \frac{\pi}{c_4} (a_d + c_5) \right\}$$

(4-180)

which will be designated v(x), and the expression below designated v.

$$\int_0^{a_d} D^*(x) \, dx = \frac{c_1}{c_2} \left\{ 1 - e^{-c_2 a_d} \right\} + \frac{c_3 c_4}{\pi} \left\{ \cos \frac{c_5}{c_4} \pi - \cos \frac{\pi}{c_4} (a_d + c_5) \right\}$$ (4-181)

Then substituting into equation (170)

$$I_t(x,t) = I_o(x,t) \exp \left\{ -23.03 \frac{G \, \varepsilon \, D_A}{v \, N_o} \left\{ \frac{\pi}{2b} \right\} \left\{ \frac{1}{k_1^2 + \left\{ \frac{\pi}{b} \right\}^2} \right\} v(x) \cdot \ell(t) \right\}$$ (4-182)

and $X = \left(\frac{23.03 \, G \, \varepsilon \, D_A}{v \, N_o} \right)$

One requires an expression for $I_o(x,t)$,

$$I_o(x,t) = \lambda \, c(x) \cdot \xi_n \, g(t)$$

where

$c(x) = \cos \frac{\pi}{2a_c} x$, the Cerenkov depth distribution function

$g(t) = \sin \frac{\pi}{b} t$, the Cerenkov emission as a function of time.

Thus, substituting finally into equation (4-4),

$$U = \log_{10} \frac{\displaystyle\int_o^b \int_o^{a_c} \lambda\, \xi_n \sin\frac{\pi}{b} t \cos\frac{\pi}{2a_c} x\; dxdt}{\displaystyle\int_o^b \int_o^{a_c} \lambda\, \xi_n \sin\frac{\pi}{b} t \cos\frac{\pi}{2a_c} x \exp\left\{-X\frac{\pi}{2b}\right\}\left\{\frac{1}{k_1^2 + \frac{\pi}{b}^2}\right\} v(x)\cdot\ell(t)\right\} dx} \qquad (4\text{-}183)$$

or if one considers unequal dose and Cerenkov pulse lengths, one has (similarly to (4-147)),

$$U = \log_{10} \frac{\displaystyle\int_o^c \int_o^{a_c} \Lambda \sin\frac{\pi}{c} t' \cos\frac{\pi}{2a_c} x\; dxdt'}{\displaystyle\int_o^c \int_o^{a_c} \Lambda \sin\frac{\pi}{c} t' \cos\frac{\pi x}{2a_c} \exp\left\{-X\frac{\pi}{2b}\right\}\left\{\frac{1}{k_1^2 + \frac{\pi}{b}^2}\right\}v(x)\cdot\ell(t' + \frac{b}{2} - \frac{c}{2})\right\} dxdt'} \qquad (4\text{-}184)$$

These double integrals can be evaluated numerically on the computer, using double Gaussian quadrature. A sample calculation for equation (4-184) is shown in figure 4-4, where the absorbance is again plotted as a function of k_1 the pseudo first-order rate of decay for the absorbing species. The effect of including different durations for the Cerenkov and dose pulses is illustrated for several different values of the Cerenkov pulse width c, while keeping the dose pulse constant at b = 3.8 nanoseconds. This figure shows the significant increase in the absorbance for decay rates $k_1 < 5 \times 10^9$ sec^{-1}, resulting from the buildup of absorbing species before the Cerenkov emission begins. Fortunately such effects are fairly small
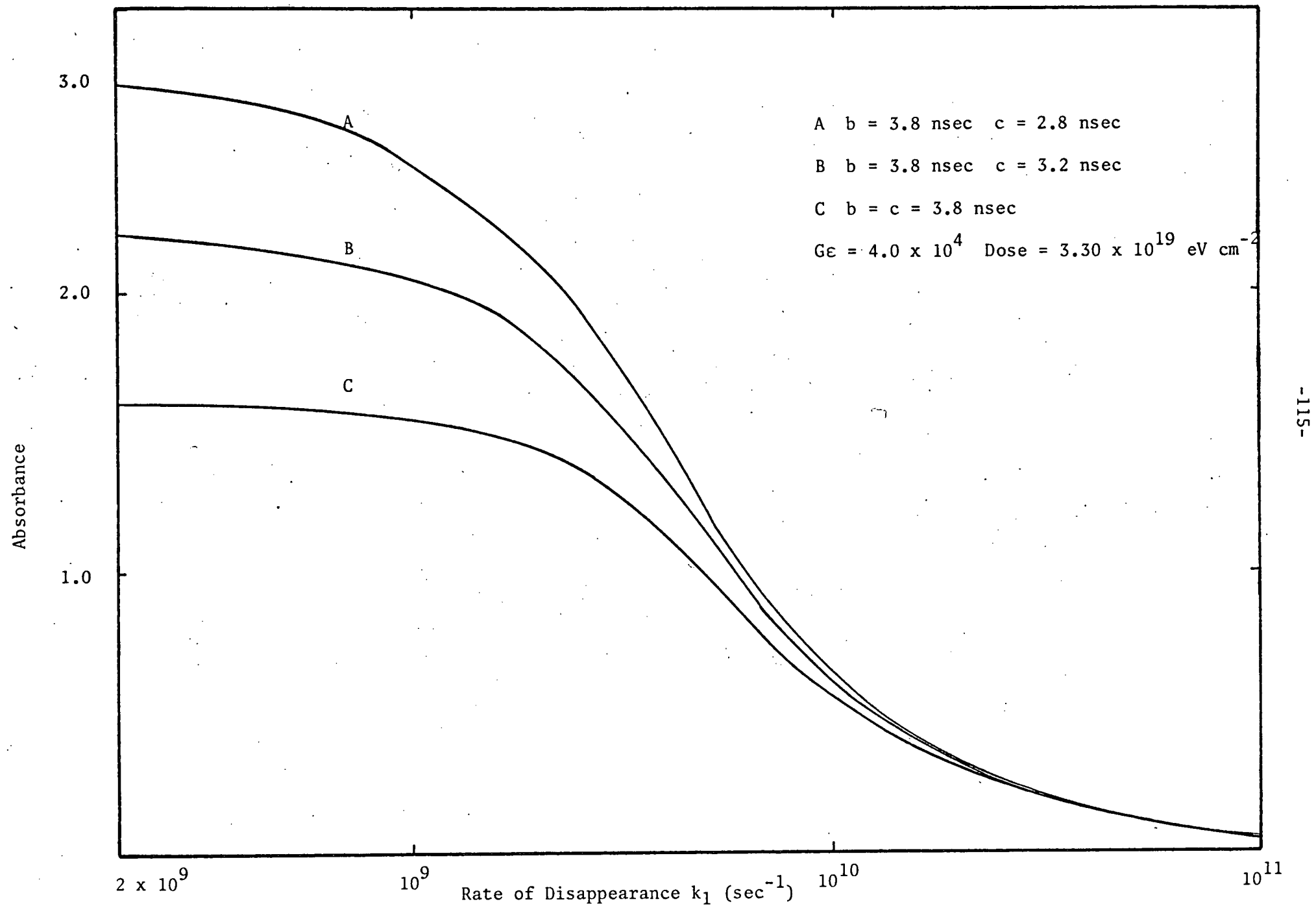
Figure 4-4 The effect of several combinations of Cerenkov and dose pulse durations ob the calculated absorbance of e^-_{aq}

in this work, where c = 3.2 nanoseconds, so that calculations (equation 4-52) based on the monoenergetic approximation can still be used to compare relative G products where the rate of disappearance of the absorbing species is $k_1 < 10^9$ sec^{-1}.

The functional dependence of the absorbance on the Gε product is shown in figure (4-5(a)) for several values of k_1. It is noteworthy that for $k_1 > 5 \times 10^9$ sec^{-1}, the absorbance is directly proportional to the Gε product, rather than to the logarithm of Gε product for species (equation 4-52). Thus, absorption spectra obtained where the absorbing species disappear sufficiently rapidly will have exactly the same shape as those obtained by the more normal absorption spectrometric techniques.

For long lived absorbing species, it is expected that reabsorption would significantly alter the shape of the absorbed Cerenkov light pulse from that of the reference Cerenkov light pulse, because of the build-up of absorbing species in the latter part of the pulse. Using equation (4-106) a series of pulse shapes have been calculated for different values of k_1, to illustrate this effect and the results are shown in figure 4-5(b).

(B) <u>Cerenkov Radiation Calculations</u>

In order to interpret the results of experimental Cerenkov radiation measurements it is important to have a theoretical understanding of the physical parameters which characterise such emission. The starting point in this study is the fundamental equation (1-7) for Cerenkov energy loss per unit path length. Using this equation, expressions will be derived to determine the effects of electron deceleration, dispersion of the medium, and the inclusion of quantum corrections on the experimentally observed Cerenkov intensities.
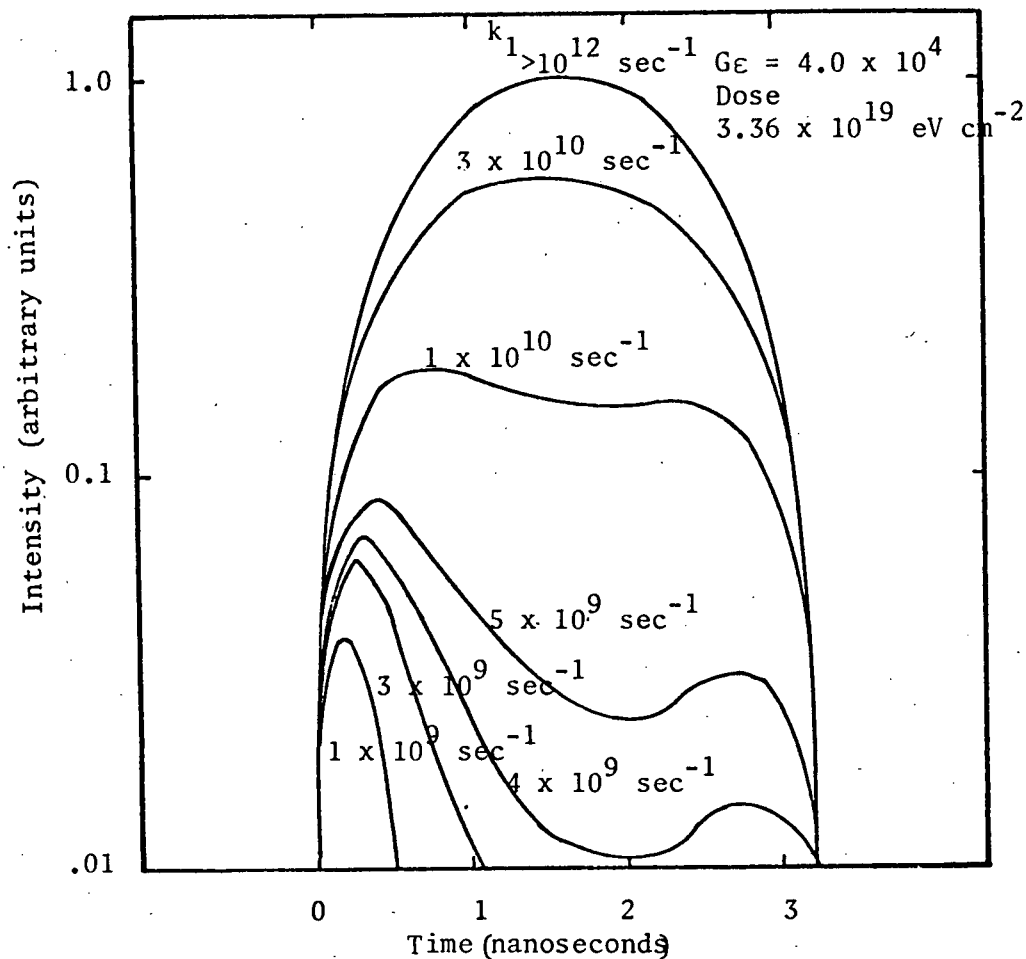
Figure 4-5(b) Calculated Cerenkov pulse shapes for the reabsorbed emission pulse.
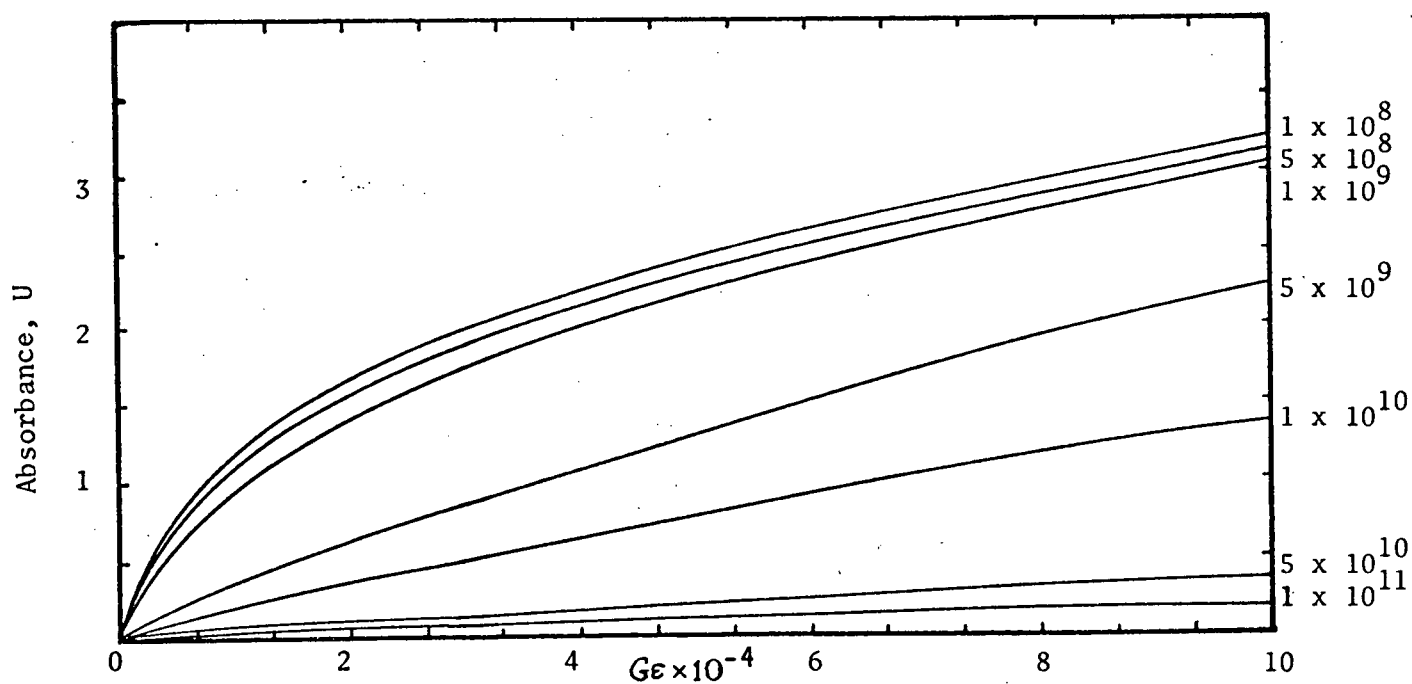
Figure 4-5(a) Functional dependence of the absorbance U on the $G\epsilon$ product for different values of k_1

(1) Relative Intensities and Energy Dependence.

Although the original theoretical treatment of Frank and Tamm assumes that the velocity of the high energy electron is constant, in the real case the effects of slowing down must be included. Fortunately this correction can be made in the framework of the original theory, because the rate of deceleration for fast electrons is sufficiently low that the coherence condition along their tracks will still be satisfied (17). Thus starting with equation (1-7),

$$\frac{dW}{dl} = \frac{e^2}{c^2} \int_{\beta n > 1} \left(1 - \frac{1}{\beta^2 n^2}\right) \omega \, d\omega \qquad (1\text{-}7)$$

$\dfrac{dW}{dl}$ = the rate of energy loss per unit path length,

e = the electron charge,

c = the velocity of light,

ω = the angular frequency of the emitted light,

$\quad$ = $2\dfrac{\pi c}{\lambda}$ where λ is the wavelength;

β = $\dfrac{v}{c}$, the ratio of the electron velocity to the speed of light in vacuum, and

n = the refractive index of the medium.

One may make the following substitutions:

$$\omega = 2\pi\nu, \quad d\omega = 2\pi \, d\nu \qquad (4\text{-}185)$$

$$\frac{dW}{dl} = \frac{d \, (N \, h\nu)}{dl} \qquad (4\text{-}186)$$

to yield

$$\frac{dN}{dl} = \frac{4 \pi^2 e^2}{c^2 h} \int_{\nu_1}^{\nu_2} (1 - \frac{1}{\beta^2 n^2}) \, d\nu \qquad (4-187)$$

and finally, making the assumption that the refractive index is frequency independent,

$$\frac{dN}{dl} = \frac{4 \pi^2 e^2}{c^2 h} (\nu_2 - \nu_1)(1 - \frac{1}{\beta^2 n^2}) \qquad (4-188)$$

where $\frac{dN}{dl}$ = the number of photons emitted per unit path length.

This expression must be integrated over the range of energies of the decelerating electron terminating when $\beta n = 1$, so that a relationship between path length and energy (or in the variables of equation (4-188) path length and β) must next be derived. From the Bethe equation (see equation (1-3)) one has:

$$\frac{dE}{dl} = - \frac{2 \pi N_o e^4 \rho Z}{m_o c^2 \beta^2 A} f(\beta) \qquad (4-189)$$

and $f(\beta) = \dfrac{\ln m_o^2 c^4 \beta^2 (1 - \sqrt{1 - \beta^2}) + (1 - \beta^2)(\ln 2 + \frac{9}{8})}{2 I^2 (1 - \beta^2)^{3/2}}$

$$- \sqrt{1 - \beta^2} \, (\frac{1}{4} + 2 \ln 2) + \frac{1}{8} \qquad (4-190)$$

where A = atomic weight of the absorber,

      Z = atomic number of the absorber,

      ρ = density of the absorber,

      N_o = Avagadro's number

      e = the electron charge,

      m_o = the rest mass of the electron,

      I = the average excitation potential, calculated from the Bragg

rule for compounds or mixtures, and

$$E = m_o c^2 \left(\frac{1}{\sqrt{1 - \beta^2}} - 1 \right) \tag{4-191}$$

Thus one can obtain directly from the chain rule the required

relationship between $d\beta$ and dl;

$$\frac{d\beta}{dl} = \frac{dE}{dl} \cdot \frac{d\beta}{dE} \tag{4-192}$$

Differentiating (4-191)

$$\frac{dE}{d\beta} = m_o c^2 \beta (1 - \beta^2)^{-\frac{3}{2}}, \text{ so that} \tag{4-193}$$

$$\frac{d\beta}{dl} = -\frac{2 \pi e^4 Z \rho N_o f(\beta)}{m_o^2 c^4 \beta^3 A (1 - \beta^2)^{-\frac{3}{2}}}$$

Therefore upon substitution into (4-188) the final result is:

$$N = \frac{1}{n^2} (\nu_1 - \nu_2) \frac{2 \pi m_o^2 c^3 A}{he^2 Z N_o} \int_{\frac{1}{n}}^{\beta_o} \frac{(\beta^2 n^2 - 1)}{(1 - \beta^2)^{\frac{3}{2}}} \frac{1}{f(\beta)} d\beta \tag{4-195}$$

where β_o refers to the velocity of the incident electron and N is the

total number of emitted photons.

Direct evaluation of the integral in (4-194) is impossible

because of the complicated form of $f(\beta)$. However, over the small range

of energies(265 - 600 KeV) in this work the approximation that $f(\beta)$

is a constant can be made. Thus integrating the remainder of (4-195)

one has:

$$N = \frac{1}{n^2} (\nu_1 - \nu_2) \left\{ \frac{2 \pi m_o^2 c^2 A}{he^2 Z \rho N_o} \right\} \frac{1}{f(\beta_o)} \left\{ \frac{\beta_o^2 n^2 - 1}{(1 - \beta_o^2)^{\frac{1}{2}}} + Zn^2(1 - \beta_o^2)^{\frac{1}{2}} - Zn(n^2 - 1)^{\frac{1}{2}} \right\} \quad (4-196)$$

Comparison with the results of a complete numerical integration

of equation (4-195) shows that at these low energies equation (4-196) is a

very good approximation, significant deviations appearing only for

energies in the MeV region. The important variables in equation (4-196)

are the density, refractive index and the incident electron velocity.

Apart from the density, the functional dependence of N on the variables

n and β is best described graphically. Figures 4-6(a) and 4-6(b)

illustrate respectively the energy dependence of the photon yield in water

and the effect of increasing refractive index for a medium of unit

density and incident electron energy 0.5 MeV. Surprisingly, in this

energy range, the number of photons per incident electron shows a

rectilinear dependence on both refractive index and incident energy.

(2) Inclusion of Dispersion.

In the previous section the integral over emission frequencies

in equation (4-187) was evaluated assuming the refractive index of the

emitting medium to be independent of wavelength. For the visible part

of the spectrum this approximation is quite good but towards the ultra-

violet the refractive index increases rather rapidly, especially near

absorption bands. Since Cerenkov radiation has been used to calibrate
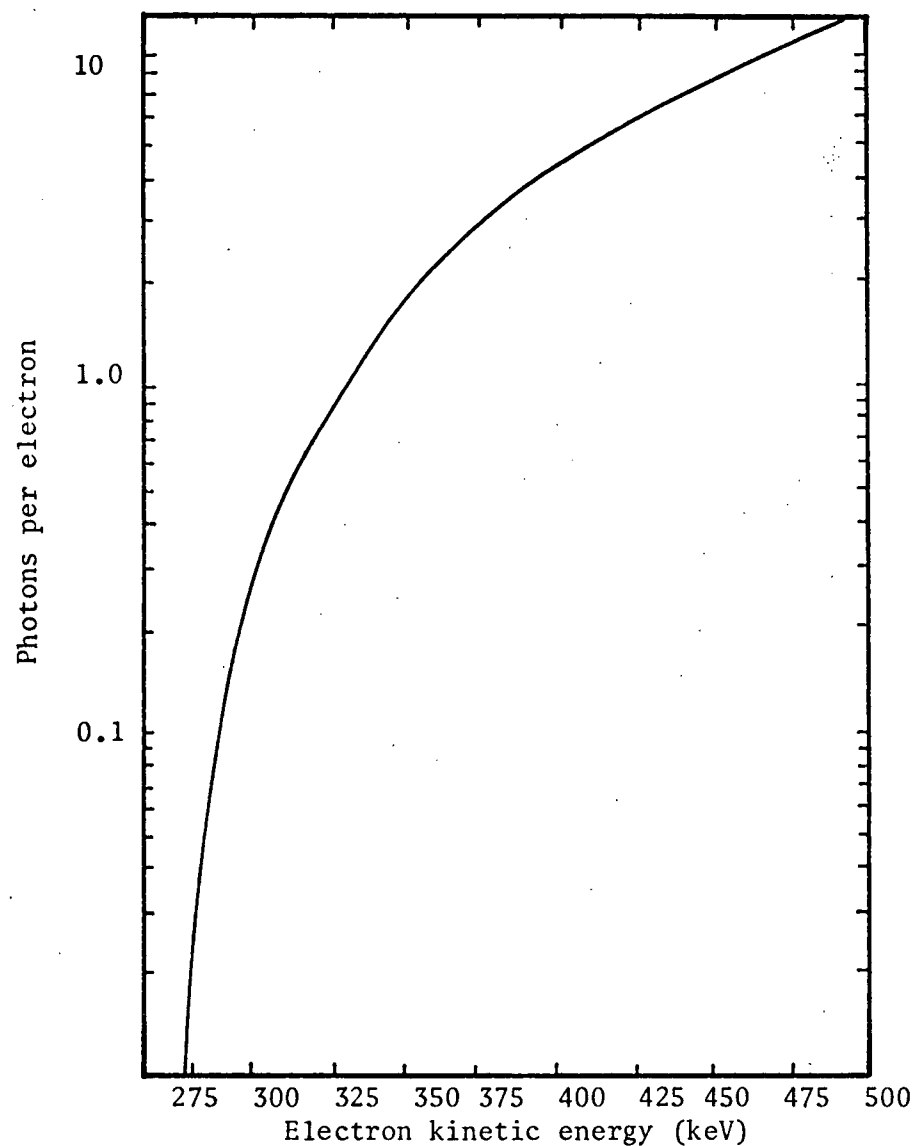
Figure 4-6(a)   The number of Cerenkov photons per
high energy electron in the wavelength
interval 400 nm-600 nm in water as a
function of electron kinetic energy.
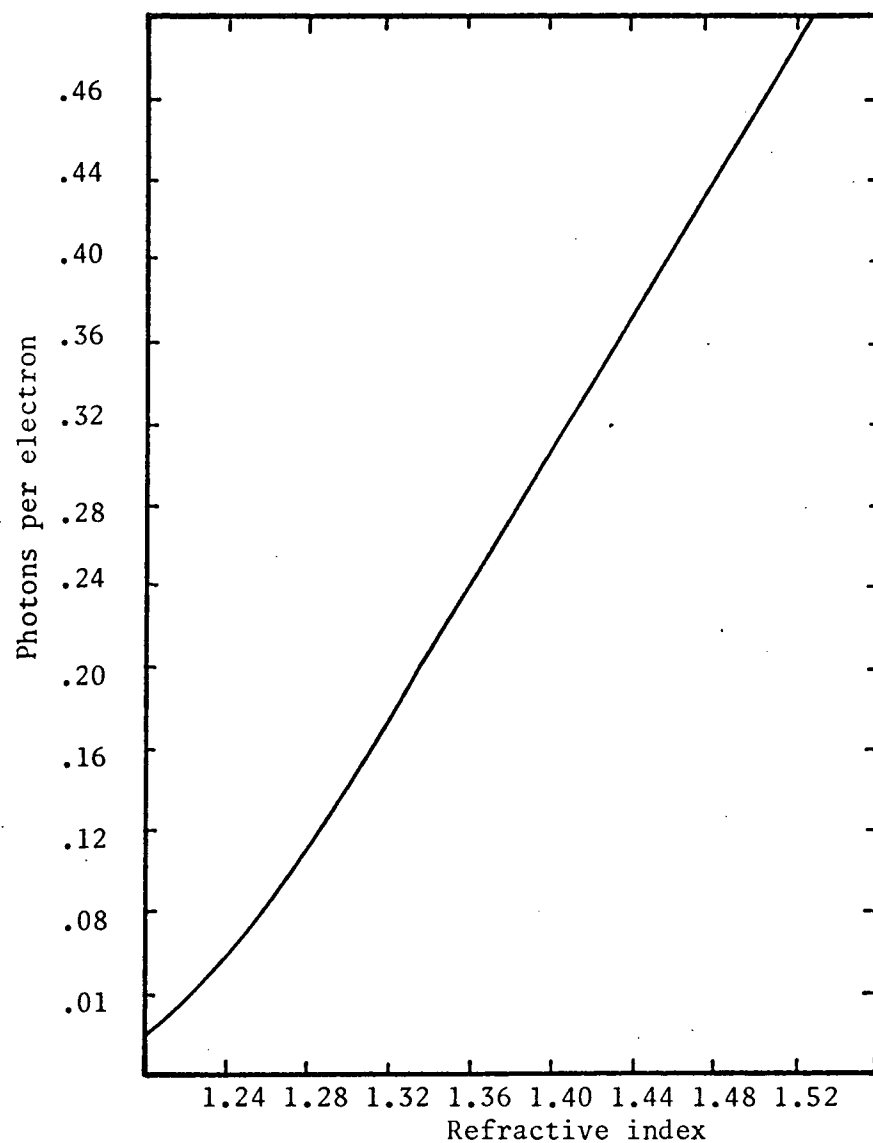
Figure 4-6 (b)   The numbers of Cerenkov photons
per 500 keV electron in a 10.0 nm
interval centered at 600 nm as a
function of refractive index in water.

the spectral sensitivity of photomultipliers in the ultra-violet

region (77) where black body sources have very low intensity, a

quantitative evaluation of the difference between the exact spectral

distribution and the simple λ^{-2} spectral distribution was undertaken

for water for which the refractive index as a function of wavelength is

well documented (78).

Starting from equation (4-187), and writing n = n(ν),

one has that:

$$\frac{dN}{dl} = \frac{4 \pi^2 e^2}{c^2 h} \int_{\nu_1}^{\nu_2} (1 - \frac{1}{\beta^2 n^2(\nu)}) \, d\nu \qquad (4\text{-}197)$$

which may be separated into two parts as follows,

$$\frac{dN}{dl} = \frac{4 \pi^2 e^2}{c^2 h} \left[\int_{\nu_1}^{\nu_2} d\nu - \frac{1}{\beta^2} \int_{\nu_1}^{\nu_2} \frac{1}{n^2(\nu)} \, d\nu \right] \qquad (4\text{-}198)$$

$$= \frac{4 \pi^2 e^2}{c^2 h} \left\{ (\nu_2 - \nu_1) - \frac{1}{\beta^2} N^0 (\nu_1, \nu_2) \right\}$$

$$\text{where } N^0(\nu_1, \nu_2) = \int_{\nu_1}^{\nu_2} \frac{1}{n^2(\nu)} \, d\nu \qquad (4\text{-}199)$$

Using exactly the same arguments as in section (1) for the energy

dependence of the Cerenkov emission, one can obtain the final expression

for N,

$$N = \frac{2 \pi m_o^2 c^2 A}{h \, e^2 Z \rho N_o} \int_{\frac{1}{n}}^{\beta_o} \frac{\beta}{(1 - \beta^2)^{\frac{3}{2}} f(\beta)} \left\{ \beta^2 (\nu_2 - \nu_1) - N^o(\nu_1, \nu_2) \right\} d\beta \quad (4\text{-}200)$$

Once again this equation must be evaluated numerically, integrating

first over the refractive index and secondly over β. The results of

these calculations for water, illustrated in fig. 4-7, show that

significant deviations from the λ^{-2} spectral distribution do indeed

occur in the ultra-violet region, even for a relatively transparent

liquid like water.

(3) The Region of Anomalous Dispersion.

In the neighbourhood of an absorption band the refractive

index of a medium increases rapidly, and within the band itself contains an

additional imaginary part resulting in a significantly increased

Cerenkov radiation yield. Although this emission will never be observed

because of self-absorption by the medium, it is nevertheless of interest

to estimate the magnitude of such effects. The fundamental equation for

the radiation output in this case is:

$$\frac{d\omega}{dl} = \frac{e^2}{c^2} \int \left(1 - \frac{Re \, \varepsilon \, (\omega)}{\beta^2 | \, \varepsilon \, (\omega) |^2} \right) \omega \, d\omega \quad (4\text{-}201)$$
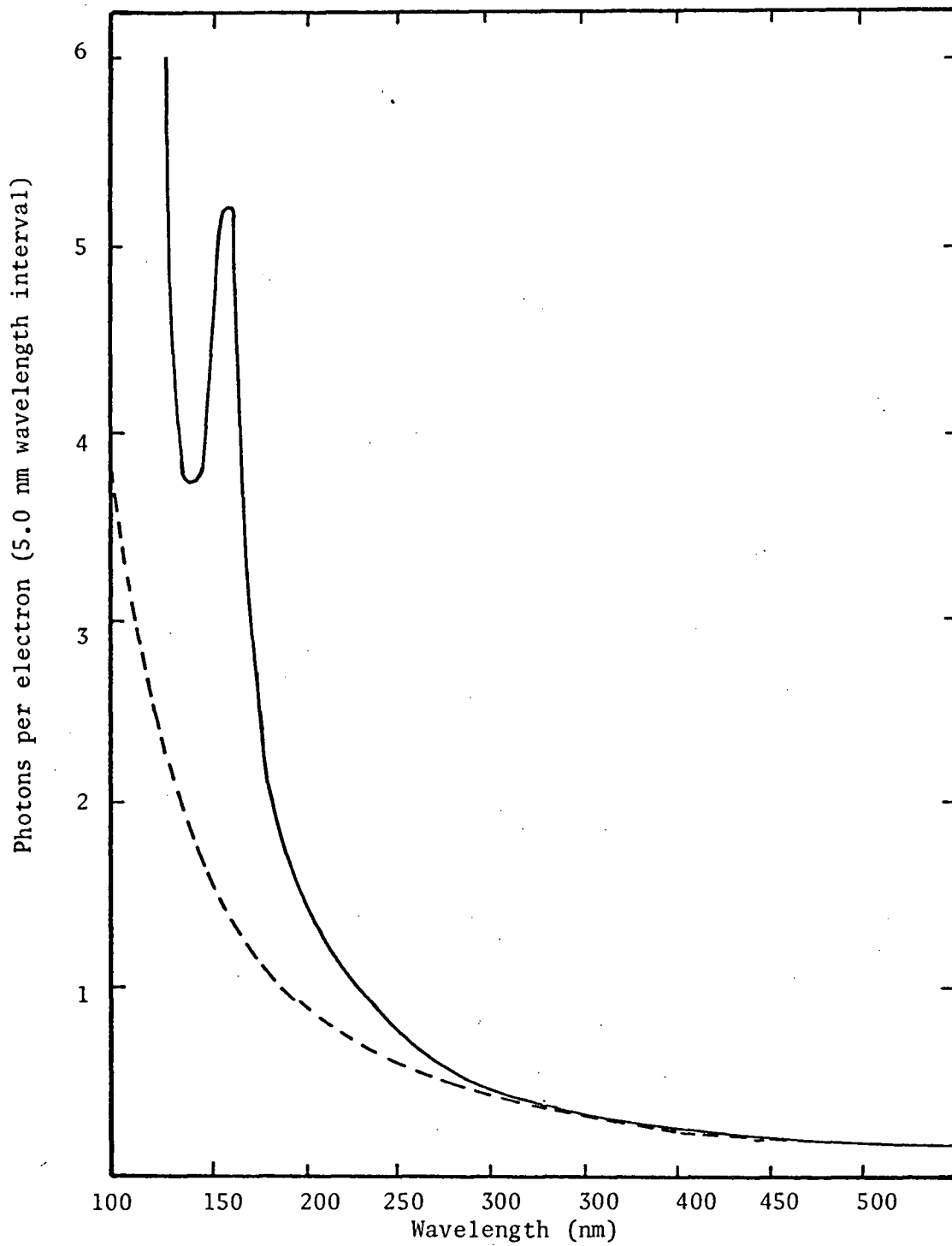
Figure 4-7   Cerenkov emission spectrum calculated taking dispersion into account (solid line) and λ^{-2} dependency (dotted line) in water, for 500 keV electrons.

where $\varepsilon(\omega) = Re\ \varepsilon(\omega) + i\ Im\ \varepsilon(\omega)$, is the complex (high frequency)

dielectric constant of the medium. The final expression, derived in a

similar way to equation (4-200), for the photon yield is:

$$N = \frac{2\pi m_o^2 c^2 A}{h\ e^2 Z\ \rho\ N_o} \int_{\frac{1}{n}}^{\beta_o} \frac{\beta}{(1-\beta^2)^{\frac{3}{2}} f(\beta)} \left\{ \beta^2 (\nu_2 - \nu_1) - N'(\nu_1, \nu_2) \right\} d\beta \qquad (4\text{-}203)$$

$$\text{where} \quad N'(\nu_1, \nu_2) = \int_{\nu_1}^{\nu_2} \frac{Re\ \varepsilon(\nu)}{|\varepsilon(\nu)|^2}\ d\nu \qquad (4\text{-}204)$$

The recent availability of vacuum ultra-violet optical constants ([79])

for water allows these equations to be evaluated in the wavelength range

125 nm - 200 nm to calculate the spectrum shown in fig. 4-7, the

total number of photons per electron in this wavelength range

corresponding to a 100 eV yield of about 10^{-2} for a 0.5 MeV electron.

(4)   The Inclusion of Modifications due to Quantum Theory.

        With the inclusion of effects due to the reaction of the

emitted photon on the motion of the electron, small higher order

terms are introduced into equation (1-7) giving ([17]):

$$\frac{d\omega}{dl} = \frac{e^2}{c^2} \int 1 - \frac{1}{\beta^2 n^2} (1 + \frac{n^4}{4} \left\{ \frac{\hbar\omega}{mc^2} \right\}^2 + n^2 \left\{ \frac{\hbar\omega}{mc^2} \right\})\omega\ d\omega \qquad (4\text{-}205)$$

and if slowing down is included, the equation for the total number of photons

per incident electron is:

$$N = \frac{2 \pi m_o^2 c^2 A}{h e^2 Z \rho N_o} \int_{\frac{1}{n}}^{\beta_o} \frac{\beta}{(1 - \beta^2)^{\frac{3}{2}} f(\beta)} \left\{ \beta^2 (\nu_1 - \nu_2) - N^2 (\nu_1, \nu_2) \right\} d\beta \quad (4\text{-}206)$$

where $N^2(\nu_1, \nu_2) = \int_{\nu_1}^{\nu_2} \left\{ \frac{1}{n^2(\nu)} + \frac{h \nu}{mc^2} + \left\{ \frac{h}{mc^2} \right\}^2 \frac{n^2(\nu) \nu^2}{4} \right\} d\nu \quad (4\text{-}207)$

Evaluation of this expression by numerical integration shows that these quantum effects are so small that they can be completely ignored, since their inclusion changes the calculated yield of photons by less than 0.1% at all wavelengths.

CHAPTER V

PRESENTATION OF EXPERIMENTAL RESULTS

(A) The Question of Light Emission from Physicochemical Processes in the
     Radiolysis of Water

In a previous study (69,80) of light emission from pulse irradiated

water (using the 30 nanosecond pulse from the Febetron 701 (266/5235)

it was concluded that the principal origin of the radiation-induced

luminescence observed in the spectral region 400 nm - 600 nm was the

Cerenkov effect, rather than any molecular process as had been previously

proposed (81). A preliminary aspect of this thesis is the further

investigation of this emission from pulse-irradiated water, using the

even higher dose-rate (increased by x 100) 3 nanosecond pulse from the

Febetron 730/2667, extending both the temporal and spectral ranges of

these studies.

Spectrophotometric measurements in doubly distilled water were

made over the spectral range 200 nm - 750 nm, using the Jarrell Ash

monochromator and either RCA 1P28 or Hamamatsu R213 photomultipliers with

a linear distribution of dynode voltages, in conjunction with the

Tektronix 454 oscilloscope. A typical waveform, as shown in figure 5-1(a),

has a width at half-height of $\sim$ 6 nanoseconds, considerably broader

than would be predicted from Faraday cup measurements, although the width

is constant at all wavelengths. Rough correction of these data (in the

range 300 nm - 650 nm) for the spectral sensitivity of the photomultiplier,

(a) 5 nanoseconds/div
10 mv/div
Tektronix 454 oscilloscope

(b) 1 nanosecond/div
10 mv/div
Hewlett Packard 183A
oscilloscope

(c) 2 nanosecond/div
10 mv/div
Hewlett Packard 183A
oscilloscope

(d) 2 nanoseconds/div
10 mv/div
Hewlett Packard 183A
oscilloscope
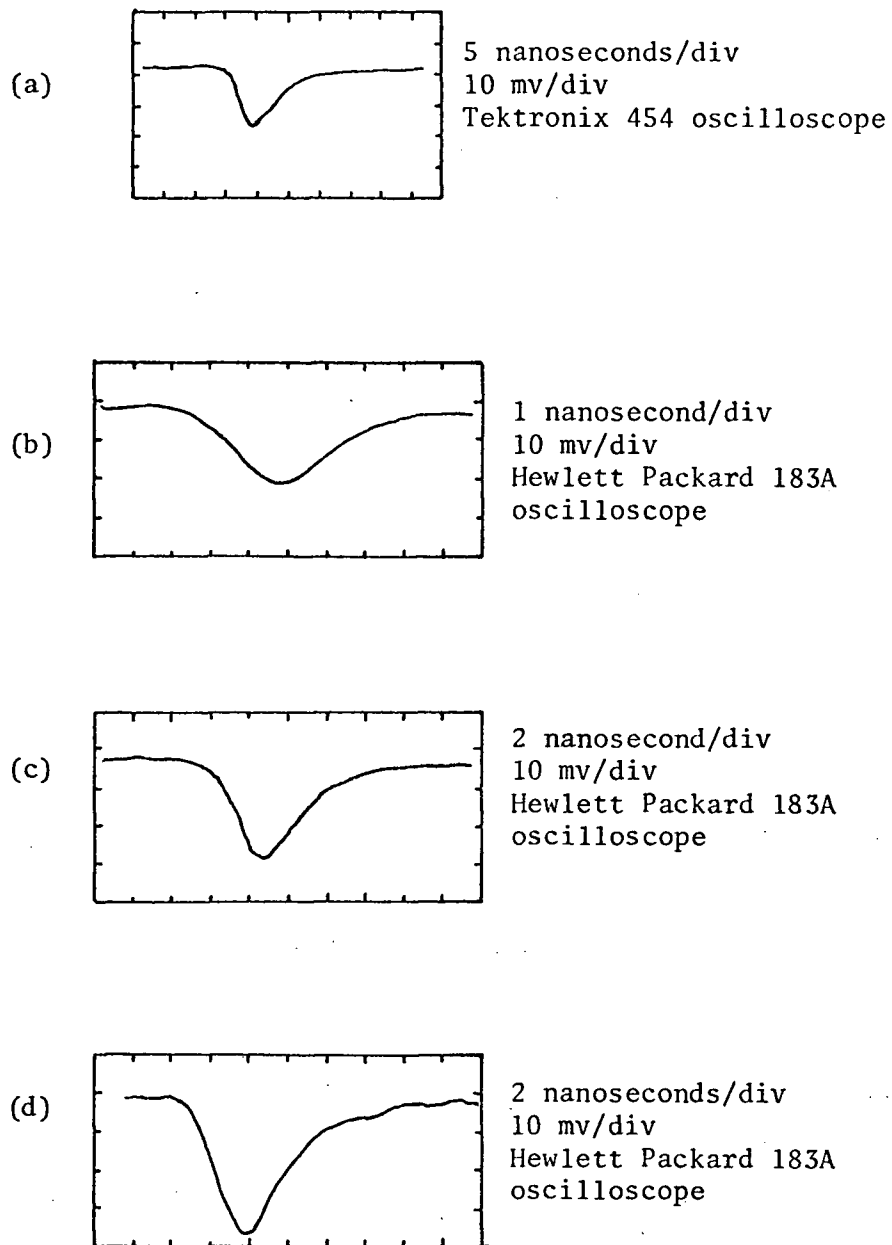
Figure 5-1 Reproductions of oscilloscope traces of light emission pulses

    (a)   pure water
    (b)   pure water
    (c)   1 M H_2O_2 in water
    (d)   0.5 M sodium salicylate in water

using a standard lamp of known emissivity (having substituted a $10^7 \Omega$
anode load in the photomultiplier chain assembly to increase its
sensitivity) showed that the intensity of this emission decreased
continuously into the red. However, no quantitative spectral measure-
ments were made over the entire spectral range. More recent photometric
measurements (figure 5-1(b)) using a detection system of improved
frequency response, which consisted of an RCA 1P28 photomultiplier in
a non-linear dynode voltage distribution (figure 3-8(a)) coupled to
Hewlett Packard 183A oscilloscope have shown these light pulses to be
significantly narrower, $\sim$ 3.5 nanoseconds in pure water. In order to
corroborate the previously estimated radiation yield of luminescence
in pure water (69,80), a comparison was made between emission from pure
water and the fluorescence intensity of a 0.5 M sodium salicylate solution
for which the 100 eV yield of photons has been measured independently (82).
The observed light emission waveforms at 420 nm are reproduced in figure 5-1(c)
and 5-1(d) for pure water and 0.5 M sodium salicylate respectively, both
pulses being of quite similar duration because of the very short lifetime
of the salicylate fluorescence in irradiated water. Before any comparisons
are possible, a number of corrections must be made for the different
spatial and spectral distributions of the emitted light as detailed in
Appendix D, giving a 100 eV yield of emission in the spectral range
400 nm - 600 nm of

$$G_{400-600} = 8 \pm 4 \times 10^{-4} \text{ photons } (100 \text{ eV})^{-1}.$$

This figure is to be compared with the previous measurement (80)

$$G_{400-600} = 9 \pm 4 \times 10^{-4} \text{ photons } (100 \text{ eV})^{-1}$$

for the 30 nanosecond pulse, both values having been obtained at a
similar average electron kinetic energy of $\sim$ 450 keV.

Spectrographic measurements would be expected to be more sensitive
to long-lived weak luminescence than short-lived intense emission, because
of the decreasing reciprocity law failure at longer time-scales.
However, there was no indication of any such luminescence over the
spectral range 250 nm - 850 nm, and in particular the 250 nm - 400 nm
region, where electron-induced emission from ice has recently been
observed (84).

From both spectrophotometric and spectrographic measurements, the
spectral distribution of the emitted light from water appeared to diminish
more rapidly into the red than would be expected for the λ^{-2} Cerenkov
radiation spectral dependence. Because of the very high dose-rate used
in these studies, it is possible that some of the Cerenkov radiation is
not transmitted from the irradiated water, due to reabsorption by the
high concentration of hydrated electrons simultaneously produced by the
high energy electron pulse. The addition of chemical scavengers to
water, which would suppress the hydrated electron, resulted in a dramatic
increase (corresponding to an absorbance $\sim$ 1) in the intensity of emission
over the entire visible region, especially in the red where the maximum
absorption of the hydrated electron occurs. This effect was previously
proposed to explain the deviations from the λ^{-2} Cerenkov spectral obtained
in experiments using the 30 nanosecond pulse (69). However, calculations
using equation (4-184) show that the magnitude of the reabsorption in
the latter experiments would have been small, with U $\sim$ 0.2 at 600 nm,
because of the lower dose-rate with the 30 nanosecond pulse. With the

shorter 3 nanosecond pulse of the Febetron 730/2667 , the peak dose-rate is increased by a factor of ~400 and the Cerenkov reabsorption effect becomes quite significant, so that quantitative measurements of this reabsorption to yield the absorption spectra of transient specied produced in radiolysis are now practicable.

(B) Quantitative Measurement of Cerenkov Reabsorption

The quantitative evaluation of Cerenkov reabsorption as measured by the absorbed and reference Cerenkov light pulses, is made in different ways depending on the method of detection used. Spectrographically, the photographic emulsion integrates the total Cerenkov light pulse, yielding a number proportional to the logarithm of the exposure. Thus, one defines an absorbance U,

$$U = \log_{10} \left\{ \frac{Io}{It} \right\} \tag{4-4}$$

with
$$I_o = \int_0^{\tau_p} I_t(t)dt \tag{4-2}$$

$$I_t = \int_0^{\tau_p} I_o(t)dt \tag{4-3}$$

when I_o and I_t are the total integrated Cerenkov light emission per pulse, for the reference and absorbed Cerenkov respectively. Direct spectrophotometric observation of the actual emission pulse shape may be interpreted in two ways, comparing either the ratio of pulse areas

$$S = \frac{I_o}{I_t} \tag{4-155} \quad \text{or} \quad = \log_{10} \frac{I_o}{I_t} \tag{4-4}$$

with I_o and I_t as in (4-2) and (4-3) or the ratio of the peak heights as:

$$H = \frac{I_o \ (t \ max)}{I_t \ (t \ max)}$$

(4-162)

The choice between spectrographic or spectrophotometric methods is influenced primarily by the experimental limitations of each technique, which vary depending on the magnitude of the absorbance. It is the purpose of the following discussion to document the pitfalls and problems encountered in their application to the quantitative measurement of Cerenkov reabsorption.

(1) Spectrographic Measurements

The quantitative evaluation of sensitometric photographic densities poses difficult problems on the very short time-scale of the Cerenkov emission light pulse. The response of a photographic emulsion, measured by the sensitometric density D is a non-linear function of emulsion exposure called a characteristic curve (see figure 5-2). The difficulty that arises is that these characteristic curves show a temporal dependence corresponding to a significant lowering of emulsion sensitivity for exposure to both very high and very low incident intensities, called reciprocity law failure. The effect of high intensity reciprocity law failure as encountered in this work is illustrated in figure 5-2(a), where the long time-scale characteristic curve (A) was obtained from a series of exposures (.01 to 1 second) to a standard lamp, while the short time-scale characteristic curve (B) was derived by plotting the density of multiple pulse Cerenkov emission exposures
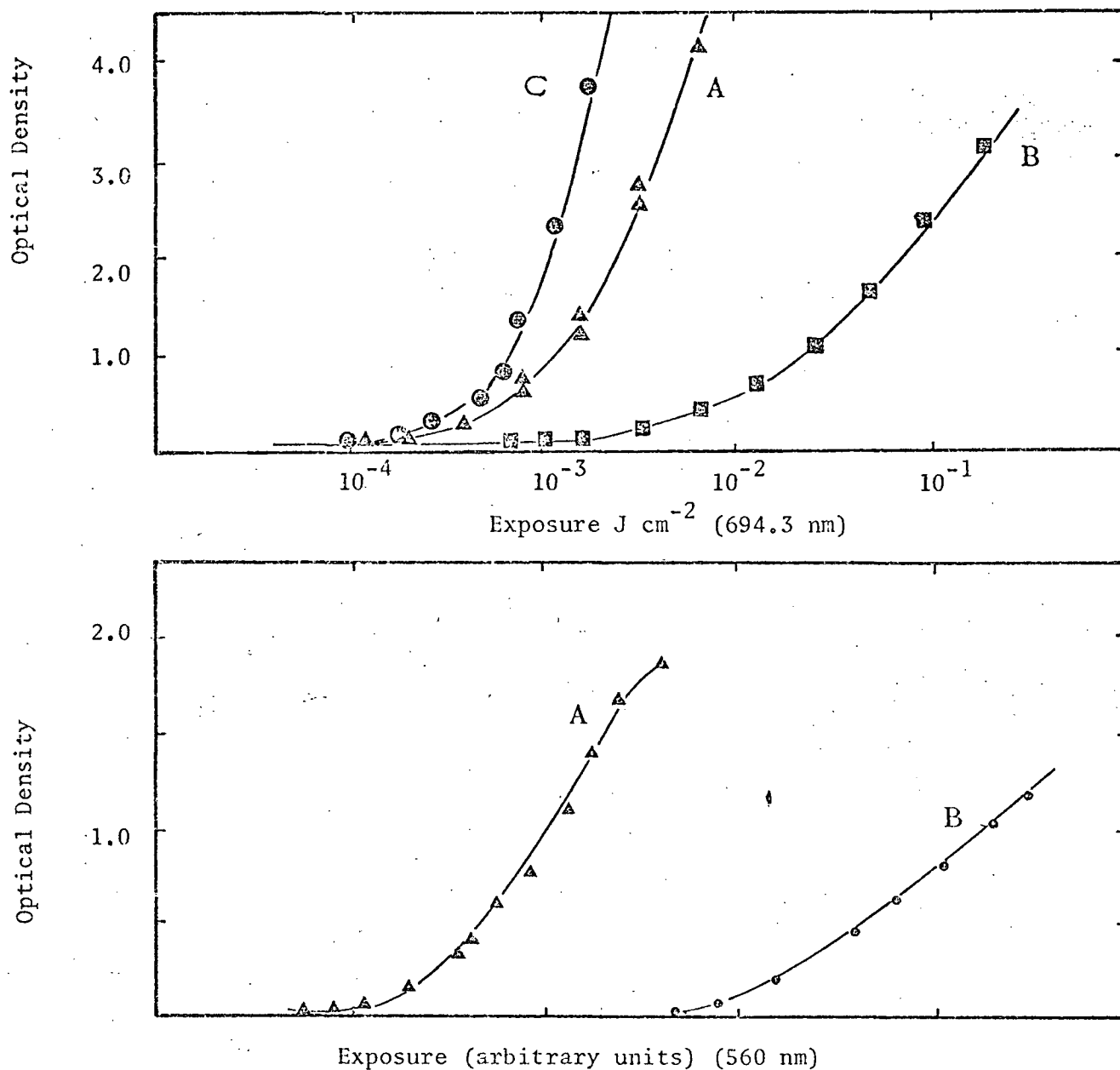
Figure 5-2 The comparison of long and short time-scale characteristic curves
(a) This work, A long time-scale (msec) curve, B Short
     time-scale (nsec) curve.
(b) Hercher and Ruff (85), B, 60 sec exposure times;
     C, .25 msec exposure times; A, 15 nsec exposure times

against the log of the number of pulses, for each point. The relative
positions of these two characteristic curves on the exposure axis
was not determined in this work, however by analogy with a previous
quantitative study of reciprocity law failure (85) shown in figure 5-2(b),
the short time-scale characteristic curve is displaced to higher exposure
by two orders of magnitude. As well, it is observed that with increasing
reciprocity law failure the gradient of the characteristic curve decreases,
further contributing to the loss of sensitivity.

The reasons for reciprocity law failure may be understood by
considering the microscopic sequence of events leading to the formation
of a latent image in the AgBr grains of a photographic emulsion (86).
The absorption of a photon produces a highly mobile photoelectron, which
upon trapping at surface defect sites on the AgBr grain, reacts with a
free Ag^+ ion to produce a trapped silver atom. When a minimum number of
these Ag atoms ($\sim$ 3.6) has been created at a particular defect site,
they form a stable latent image which then later catalyzes the development
of the entire grain. However, because of the diffusion of the Ag atoms
away from the defect site, when the incident photon flux is too low
Ag atoms escape the trapping site before the stable grouping of 3-6
atoms is achieved, giving rise to low-intensity reciprocity law failure.
On the other hand for very short, high intensity exposures, a stable
latent image is not always achieved because of the time interval required
for its formation, resulting in high-intensity reciprocity law failure.

Because of the logarithmatic relationship between film density and
exposure in the characteristic curve, the absorbance (defined by
equation (4-4)) comes directly from the difference in the abscissae

corresponding to the densities induced in the photographic emulsion by the absorbed and reference Cerenkov light pulses (see figure 5-2(a)). If characteristic curves determined from long time-scale exposures (i.e. to a standard light source) are used to calculate absorbances, the result will be to underestimate the magnitude of reabsorption, due to the increasing gradient of characteristic curves with longer time-scales. The seriousness of this effect will be minimized for high sensitivity photographic emulsions, since these materials show the least reciprocity law failure. However, the problem is eliminated by using short time-scale characteristic curves determined from multiple pulses of a suitable Cerenkov radiator. Absorbances may either be calculated directly from the densities induced by the absorbed and reference Cerenkov pulses, as indicated above, or a method of working to constant density may be used as described below. Characteristic curves are constructed using multiple pulses from the absorbing solution itself. Then, one pulse of transmitted Cerenkov radiation will produce a density on the film corresponding on the abscissa to a multiple of the 'per-pulse' Cerenkov emission from the absorbing compound, that is,

$$\log I_{cer} = \log (I_a \cdot n_{cer}) \tag{5-1}$$

where

I_{cer} = transmitted Cerenkov per pulse

I_a = absorbed Cerenkov per pulse

$\log n_{cer}$ = the numerical value of the abscissa so that

$$U = \log \frac{I_{cer}}{I_a} = \log \frac{I_a \cdot n_{cer}}{I_a} = \log n_{cer} \tag{5-2}$$

Therefore the absorbance is simply the log of the number of pulses of absorbed Cerenkov emission which gives the same density as one pulse of transmitted Cerenkov radiation. This is clearly a superior method for evaluating U, since it yields the absorbance directly and errors associated with taking differences between logarithms are eliminated.

As a demonstration of the validity of spectrographic measurements on the nanosecond time-scale, the absorption spectrum of a stable chemical species, whose spectrum could be independently determined on a spectrophotometer, was recorded in situ by the Cerenkov reabsorption technique, the spectrum being obtained from the sensitometric data by the constant density method. A 0.5 molar $NiSO_4$ aqueous solution also containing 2 molar $NaNO_3$ was chosen, the $NaNO_3$ being present to scavenge the hydrated electron and thus insure that there would be no possibility of any interfering absorption. The spectrum shown in figure 5-3 compares well with that measured on a Cary 14 spectrophotometer (the lower displacement of the spectrographic determination being due to the depth-distribution of Cerenkov radiation in water). In this way the reliability of the spectrographic method was established.

For measurements of absorbances above U $\sim$ 1.5 this constant density method significantly overestimates the magnitude of the Cerenkov reabsorption as evidenced by comparison with absorbances obtained by spectrophotometric techniques (see later). It is suggested that the spectrographic method breaks down because of reciprocity law failure between the reference and absorbed Cerenkov light pulses. That is the characteristic curves built up from multiple pulses of the reference and absorbed Cerenkov emission would not be superimposed, rather the characteristic curve derived from
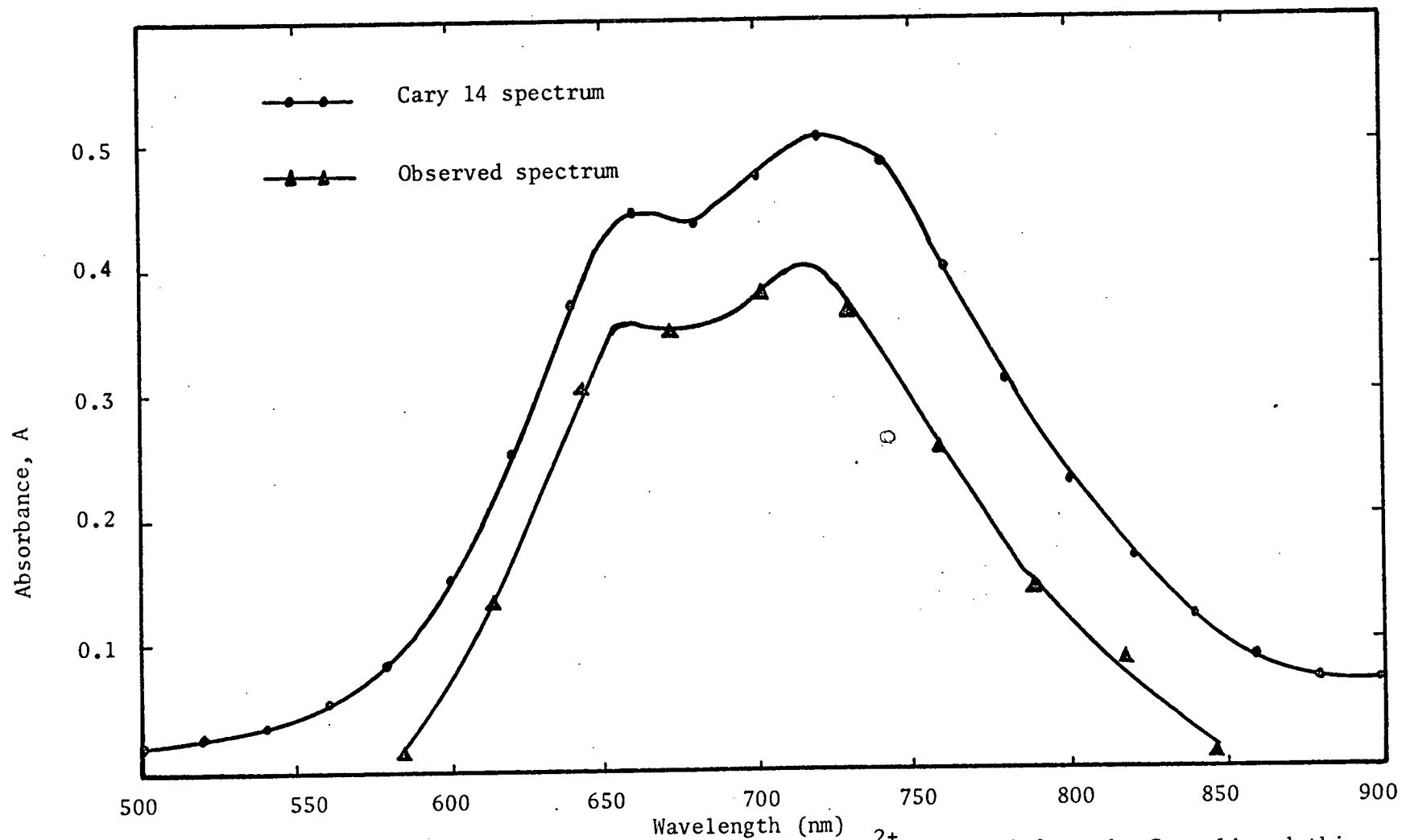
Figure 5-3 A comparison of the absorption spectrum of Ni^{2+} obtained from the Cary 14 and this technique.

the reference Cerenkov pulses would be displaced to a lower exposure with respect to that from the absorbed Cerenkov pulses. Thus the photographic emulsion is effectively more sensitive to the reference Cerenkov pulse, and therefore when the reference Cerenkov pulse is compared against the characteristic curve derived from the absorbed Cerenkov pulses, an overestimate of the absorbance is obtained, so that the resulting absorption spectrum will be more sharply peaked than in reality.

If spectrographic measurements of absorbances greater than U ∼1.5 are made using long time-scale characteristic curves, the spectrum obtained will be distorted by several factors. The higher gradient of the long time-scale characteristic curve would cause the absorbance to be underestimated, perhaps also making the absorption spectrum appear narrower, where the emulsion densities corresponding to weak absorption are on a steep part of the characteristic curve. However, the additional reciprocity law failure of the reabsorbed Cerenkov pulse (that is, many pulses are required to achieve a measurable emulsion density) results in both a net overestimation of the absorption and a broadening of the spectrum, when the logarithm of the number of the pulse required for a measurable density from the absorbed Cerenkov is combined with the difference in exposure corresponding to the respective reference and absorbed Cerenkov radiation emulsion densities. Nevertheless, although the exact shape of the absorption band would not be obtained, the wavelength of maximum absorption would remain unaffected by this distortion.

(2) Spectrophotometric Techniques

Spectrophotometric measurements of the Cerenkov emission pulse
shape were also made using an RCA 1P28 photomultiplier with a non-linear
distribution of dynode voltages (figure 3-8(a)) in conjunction with a
Hewlett Packard 183A oscilloscope. The frequency response of this
detection equipment is governed primarily by the rise time of the
oscilloscope (manufacturer's specification, rise time 10%-90% $\leqslant$ 1.5 nanoseconds)
with the estimated rise time of the photomultiplier, $\sim$ 0.5 nanoseconds with
a 50Ω load, contributing slightly. Therefore the total response time
of this photomultiplier - oscilloscope arrangement to the leading edge
of the pulse is estimated to be $\leqslant$ 2 nanoseconds. Since the Cerenkov
emission pulse will have a duration of $\sim$ 3 nanoseconds, it is not expected
to observe an undistorted pulse. However, although the oscilloscope trace
shown in figure 5-1(e) may not be a faithful reproduction of the real
pulse shape, the area of this pulse would be expected to be proportional
to the charge passed through the photomultiplier anode load, and hence
to the integrated Cerenkov emission per pulse, so that Cerenkov
reabsorption measurements can be made spectrophotometrically,
in spite of some pulse shape distortion. The comparison of peak heights
measured photometrically is not nearly as satisfactory as the use of
pulse areas, because the rise time of the detection equipment is clearly
not sufficient to fully resolve the peak. This is especially important,
since the equations in Chapter IV for the comparison of peak heights
were derived for a triangular pulse shape for which a sharp peak must
be observed.

Measurements of relative pulse areas for absorbed and reference
Cerenkov were always made with approximately equal illumination of the
photocathode by employing Wratten neutral density filters. Thus, the
electronic detection equipment always responded to approximately the
same signal in all experiments, with the photomultiplier at a constant
voltage, and hence at a constant frequency response. The range of
absorbances which can be measured by this method is restricted only
by the limiting sensitivity of the detector, with none of the reciprocity
law failure that plagues photographic detection. Therefore
spectrophotometric measurements supplement spectrographic techniques
for absorbances greater than 1.5.

(3) Spectrographic versus Spectrophotometric Methods.

Although the spectrophotometric method gives an absorbance
directly because of its linear response, the recording of spectra is
more conveniently carried out spectrographically. This is due to the
fact that an entire spectrum is recorded on the photographic emulsion
in a single event, thus eliminating problems from pulse-to-pulse
variations in point-by-point spectrophotometric measurements.
Moreover, because the 1P28 photomultiplier is insensitive beyond 650 nm,
spectrographic measurements were exclusively used in the near infrared.
The comparison between the two methods is quite satisfactory,
where equivalent measurements have been made, and a number of spectro-
photometric points are included on spectrographic results of figure 5-7.
Absorbances above $\sim$ 1.5 had to be made exclusively by the spectro-
photometric technique because of the reciprocity effects in spectrographic

measurements. Each point is an average of > 10 pulses, with the uncertainty indicated derived from this range of data.

(C)   Spectral Studies

(1)   Preliminary Spectra

(a)   Visible region

Following the initial qualitative observations of Cerenkov reabsorption by the hydrated electron, the first quantitative spectral measurements (87), in the range 410 nm - 700 nm, were made using the Bass-Kessler grating spectrograph with Kodak 2475 recording film. Characteristic curves constructed from a series of exposures to a standard lamp of known emissivity were used to convert the measured film densities to relative numbers of photons at each wavelength. It follows from the previous discussion, that these characteristic curves are clearly not the correct ones to use, but because of the very high photographic sensitivity of this particular photographic emulsion (ASA $\sim$ 3000), errors in the gradient of the characteristic curves due to reciprocity-law failure will probably be quite small, so that only absolute measurements will be seriously affected. This supposition is verified by the observation of the theoretically predicted Cerenkov emission spectra, both in spectral distribution ($I \propto \lambda^{-2}$) and relative intensities from the compounds used in this series of experiments.

The absorption spectra of solvated electrons in methanol and glycerol, and the benzene excimer in pure benzene illustrated in figure 5-4 are typical of the spectra obtained in these experiments.
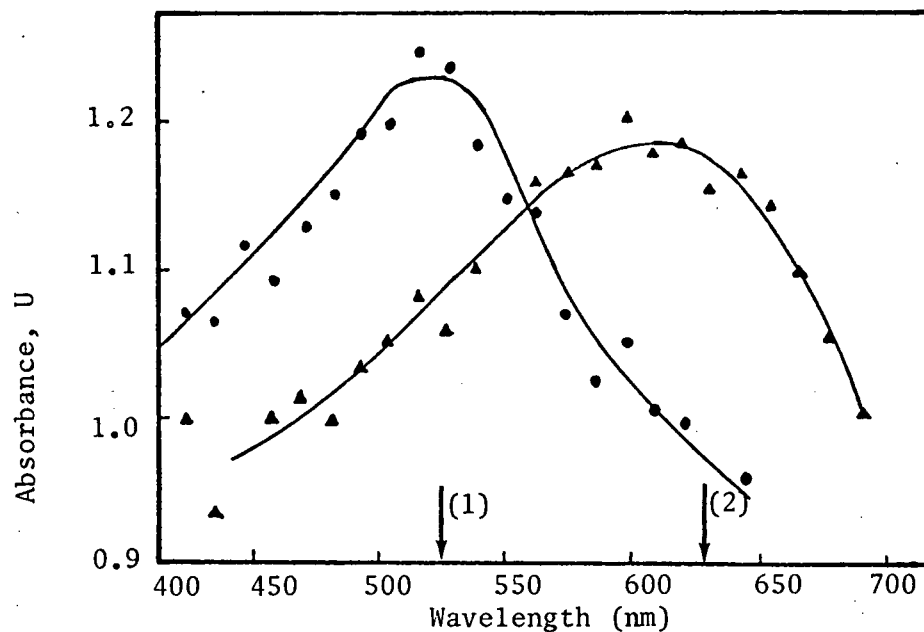
Figure 5-4(a) The solvated electron absorption
spectrum (1) glycerol and (2) methanol.
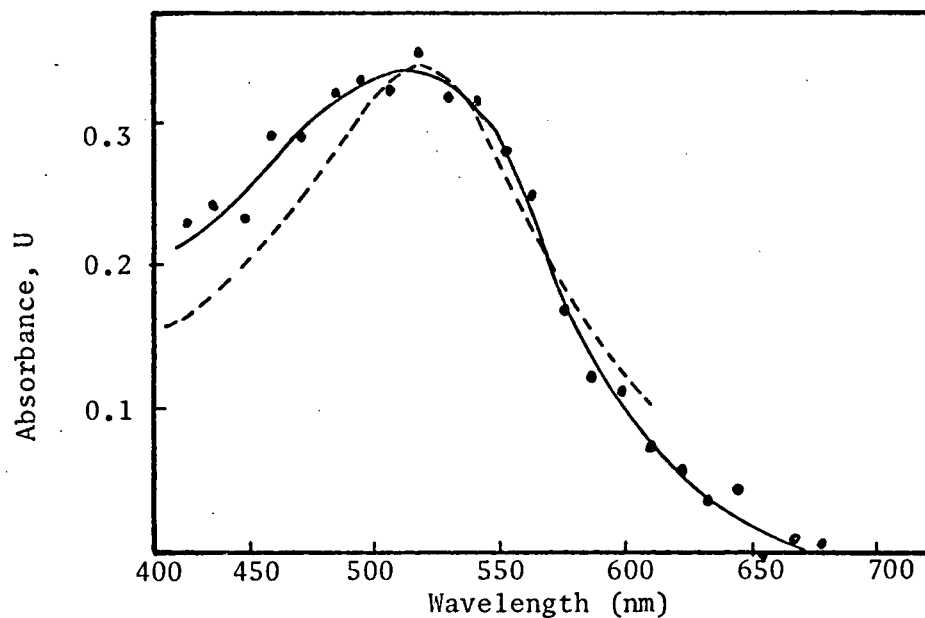
Figure 5-4 (b) The absorption spectrum of the benzene
excimer in pure benzene; the dashed
line is the spectrum observed by Cooper
and Thomas (89).

Agreement with previously reported spectra for these species is satisfactory, the positions of the published absorption maxima in alcohols (88) are indicated by arrows in figure 5-4(a), and the dashed line in figure 5-4(b) is the spectrum attributed to the benzene excimer observed by Cooper and Thomas (89).

The Cerenkov reference in the alcohols was obtained by quenching the solvated electron absorption using 2M $CHCl_3$, while for the benzene it was calculated from the cyclohexane emission spectrum, since the benzene excimer could not be satisfactorily scavenged.

For any comparison of the absorbances obtained in this series of experiments with those in all ensuing work it should be noted that the 5510 electron tube, rather than the higher dose 5515 electron tube, was used for these exploratory studies. The dose from the two tubes differs by approximately a factor of three; however, this ratio has not been measured accurately.

(b) Near-Infrared Spectra

Following the first experiments in the visible part of the spectrum, measurements were extended to the near-infrared spectral region using high speed infrared film (Kodak) and the same Bass-Kessler spectrograph. The calibration of the emission and treatment of data were exactly the same as described in section one, that is, using characteristic curves obtained on a millisecond time-scale by photographing the emission spectrum of a standard lamp of know emissivity. Because of the very much lower emulsion sensitivity of high speed

infrared film ($\sim$ 30 times less) compared to 2475 recording film, it was expected that reciprocity law failure would present a more serious problem than encountered in the visible measurements. Although the wavelength of maximum absorption would be unaffected, there would likely be a significant distortion of the absorption bands.

With the higher dose-rate electron tube (5515) which was used in these experiments, a considerable increase in the magnitude of Cerenkov reabsorption was observed. The spectra obtained were excessively broad, due to the reciprocity law failure effects inevitable in the use of long time-scale characteristic curves where there is also a very strong Cerenkov reabsorption. The wavelengths of maximum absorption for the materials studied in these experiments are given in Table IV , with the estimated magnitude of the experimental uncertainty in these measurements being primarily due to the inherent broadness of these absorption bands.

(2) Absorption Spectra in Water and Formamide.

The preliminary spectrographic studies showed, not unexpectedly, that the extraction of a reliable absorption spectrum from spectrographic data must be carried out using short time-scale characteristic curves. Thus the following spectra, obtained spectrographically, were all determined using characteristic curves built up from multiple exposures to single Cerenkov light pulses, the absorbance being obtained by the method of working to a constant density. Typical sensitometric data used to derive the spectrum of the hydrated electron in 1.0 Molar $HClO_4$ are shown in figure 5-5. The series of microdensitometer traces from

Table IV   Solvated Electron Absorption Spectra

Compound	λ-max (nm) This work	λ-max (nm) Other work (88)	Photon Energy at λ-max (kcal mole^{-1})
methanol	620 ± 20	630 ± 15	46.0 ± 1.6
2-propanol	800 ± 30	820 ± 15	35.6 ± 1.4
1-butanol	680 ± 20	680 ± 15	41.9 ± 1.4
1-pentanol	660 ± 20		43.2 ± 1.4
1,3-butanediol	650 ± 20		44.0 ± 1.4
2-methoxyethanol	720 ± 20		39.6 ± 1.3
3-methylbutanol	690 ± 20		41.3 ± 1.4
1,2-ethanediol	560 ± 10	580 ± 15	51.0 ± 1.0
1,2,3-propanetriol	525 ± 10	525 ± 15	54.4 ± 1.1
H_2O	720 ± 10	720 ± 10[*]	39.6 ± 0.7

[*]   references (89,90)

900 nm   (a)   520 nm   (b)
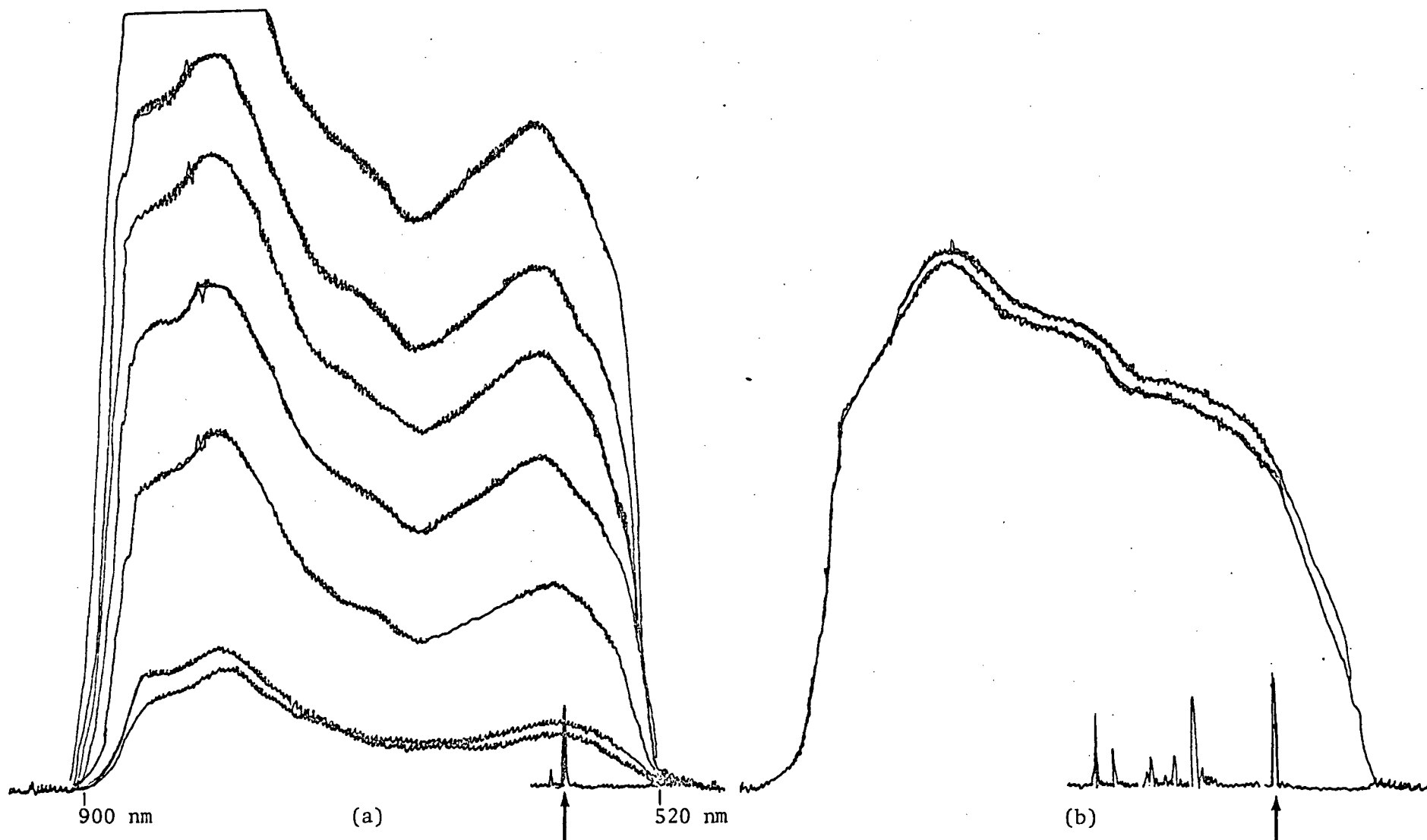
Figure 5-5   Microdensitometer tracings of the data used to calculate the absorption spectrum of the hydrated electron in 1.0 M $HClO_4$ (figure 5-7), recorded on high speed infrared film. The wavelength calibration line from Ne is indicated by an arrow.

(a)   1,2,3,4,5,7 pulses 1.0 molar $HClO_4$

(b)   3 molar H_2O_2

exposures to 1,2,3,4,5, and 7 pulses from the 1.0 M acid solution in figure 5-5(a) were plotted against the log of the number of pulses to give the characteristic curves in figure 5-6. From these characteristic curves, the absorbance at a given wavelength is then simply the value of the abscissa corresponding to the experimentally measured sensitometric density of the reference Cerenkov spectrum shown in figure 5-5(b), 3 M H_2O_2 in water. The uncertainty in the absorbance as measured by this method, is primarily due to the pulse-to-pulse variation of the Cerenkov reference, since such variations tend to be averaged out in multiple pulse characteristic curves. Thus the estimated experimental uncertainty, as indicated by the pulse-to-pulse reproducibility is less than 0.1 absorbance unit, normally being < .05, but depending on the daily operation of the electron accelerator.

(a) <u>Water</u>

With the development of suitable experimental techniques for the spectrographic measurement of Cerenkov reabsorption spectra, a comprehensive investigation of the scavenging of the hydrated electron by concentrated solutes was undertaken. In view of the recent picosecond studies along this line both H_3O^+, in the form of $HClO_4$, and non-acidic solutes such as H_2O_2 and formamide were used. Where the absorbance was less than 1.3, spectrographic detection was utilised, however because of the very strong absorption in pure water, spectrophotometric measurements were also employed (unfortunately the latter limited observations to wavelengths less than 630 nm). Spectra were obtained under the following conditions:

(i) acid solutions: 0.5, 1.0, 2.0, 3.0 molar $HClO_4$, figure 5-7.
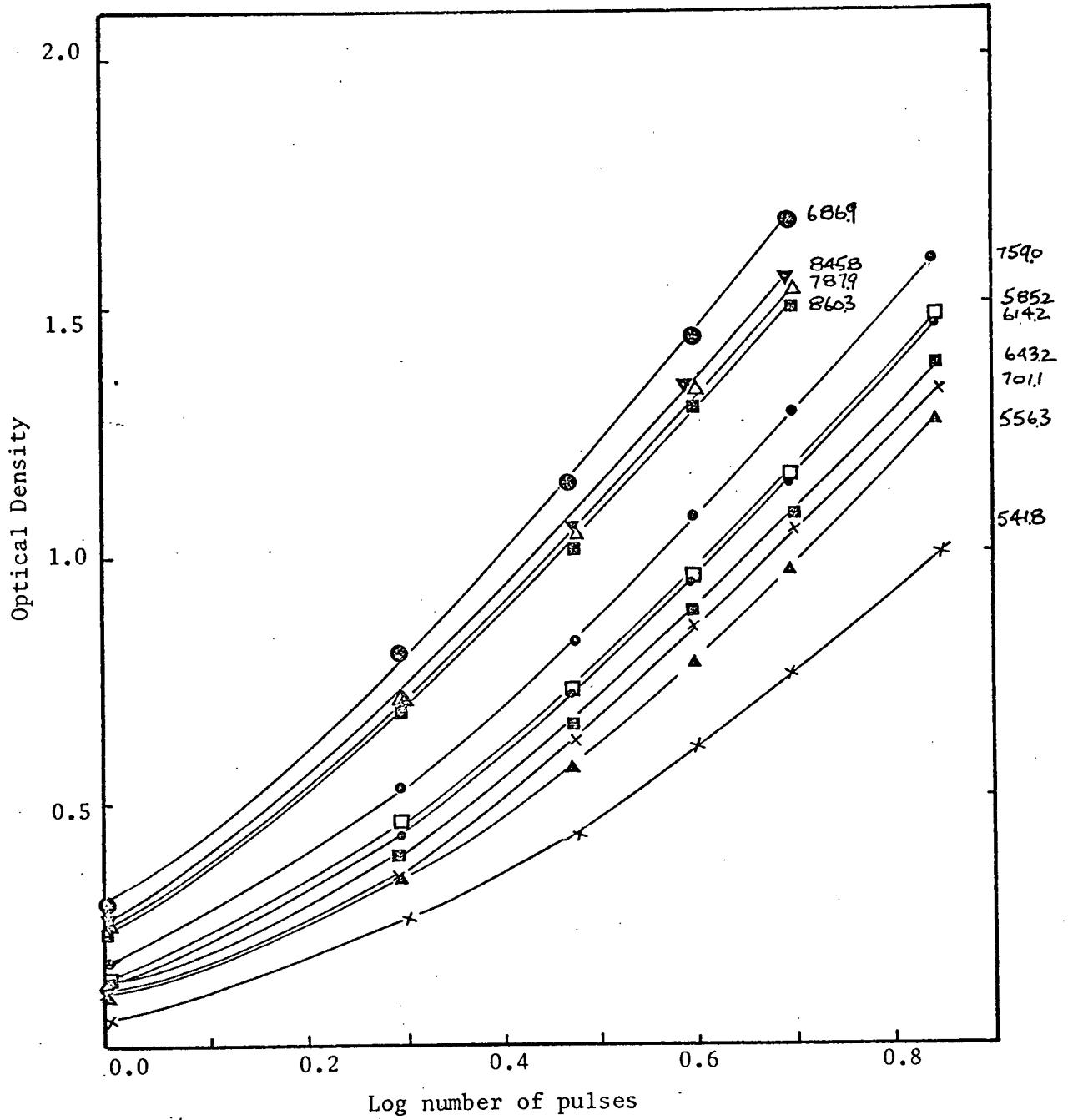
Figure 5-6 Nanosecond characteristic curves derived from the data in figure 5-4. The numbers on the left hand side give the wavelength in nm for each curve.
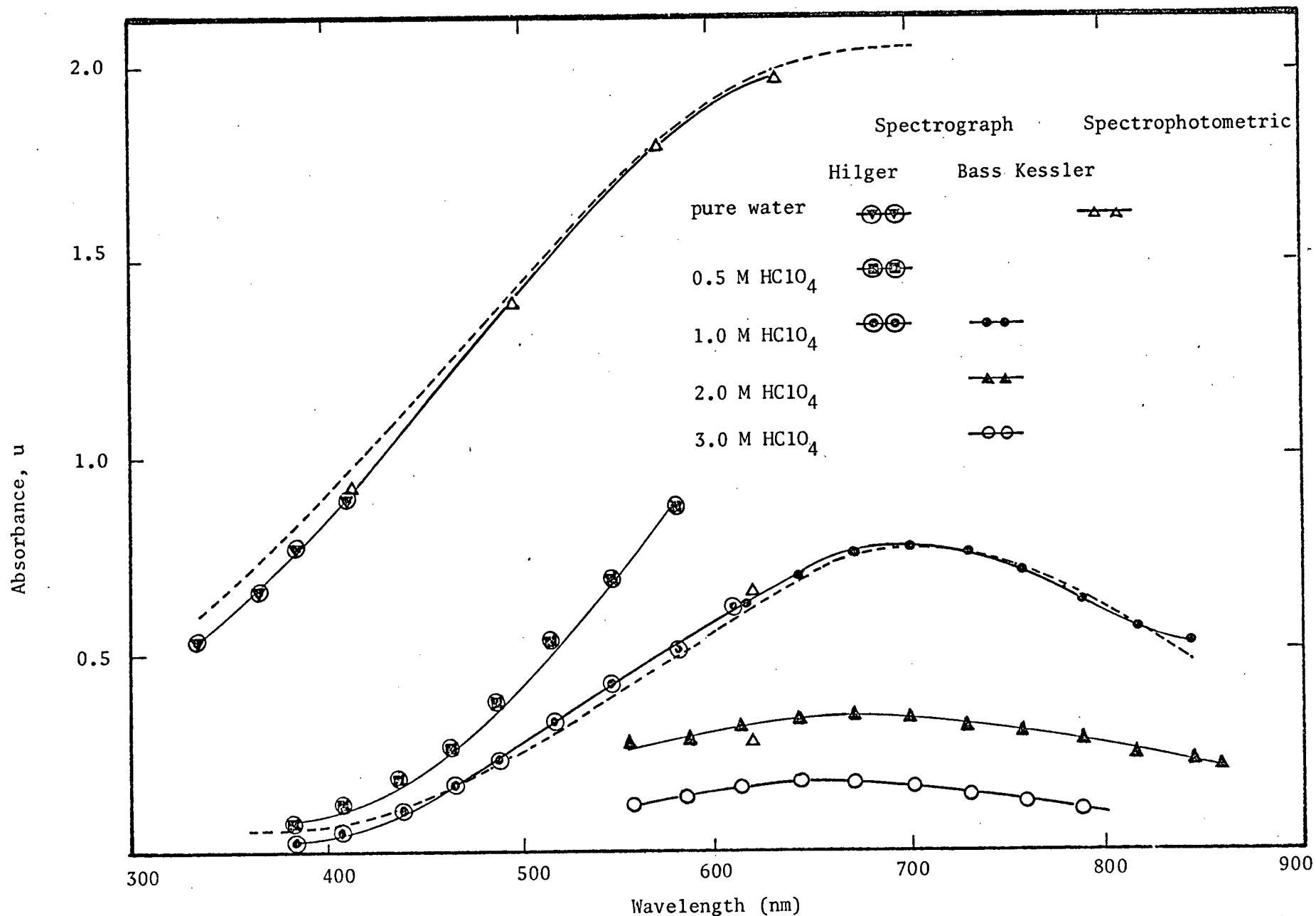
Figure 5-7 Hydrated electron spectra in water and perchloric acid solutions. The dotted line is the microsecond
data from reference (90)

(ii) H_2O_2 solutions: 0.5, 1.0, 2.0 molar, figure 5-8.

The most important parameter determining these spectra is the reference Cerenkov radiation intensity, so that several different media for Cerenkov emission were investigated. The final choices were a 3 M H_2O_2 solution for the near infrared and visible region and pure n-pentane (with a small intensity adjustment for differences in refractive index and density). The selection of 3 M H_2O_2 was strictly one of convenience and availability, since scavengers such as 2 molar $NaNO_3$, 2 molar $CdCl_2$, 5 molar $HClO_4$, or 4 molar acetone gave exactly the same results. However in the blue and near ultra-violet spectral regions, significant absorptions which were either intrinsic (H_2O_2, $NaNO_3$, $CdCl_2$) or radiation-induced ($NaNO_3$, $CdCl_2$, $HClO_4$, and acetone) required the use of some other more inert and transparent material such as n-pentane. Even so, due to reciprocity law failure, it can never be absolutely verified that this n-pentane emission has the proper Cerenkov spectral distribution in the ultra-violet region; however above 300 nm any extraneous emission or absorption from the highly purified n-pentane used in this work seems very unlikely.

The ordinate on these spectra is the experimentally measured absorbance U and must be related to the $G\varepsilon$ product for the absorbing species by the appropriate relationship derived in Chapter IV, depending on the lifetime of the absorbing species. In order to compare the previously determined microsecond spectrum of the hydrated electron with the results of these experiments, where the rate of decay is slow ($k < 10^9$) as in pure water, a logarithmatic function must be used;
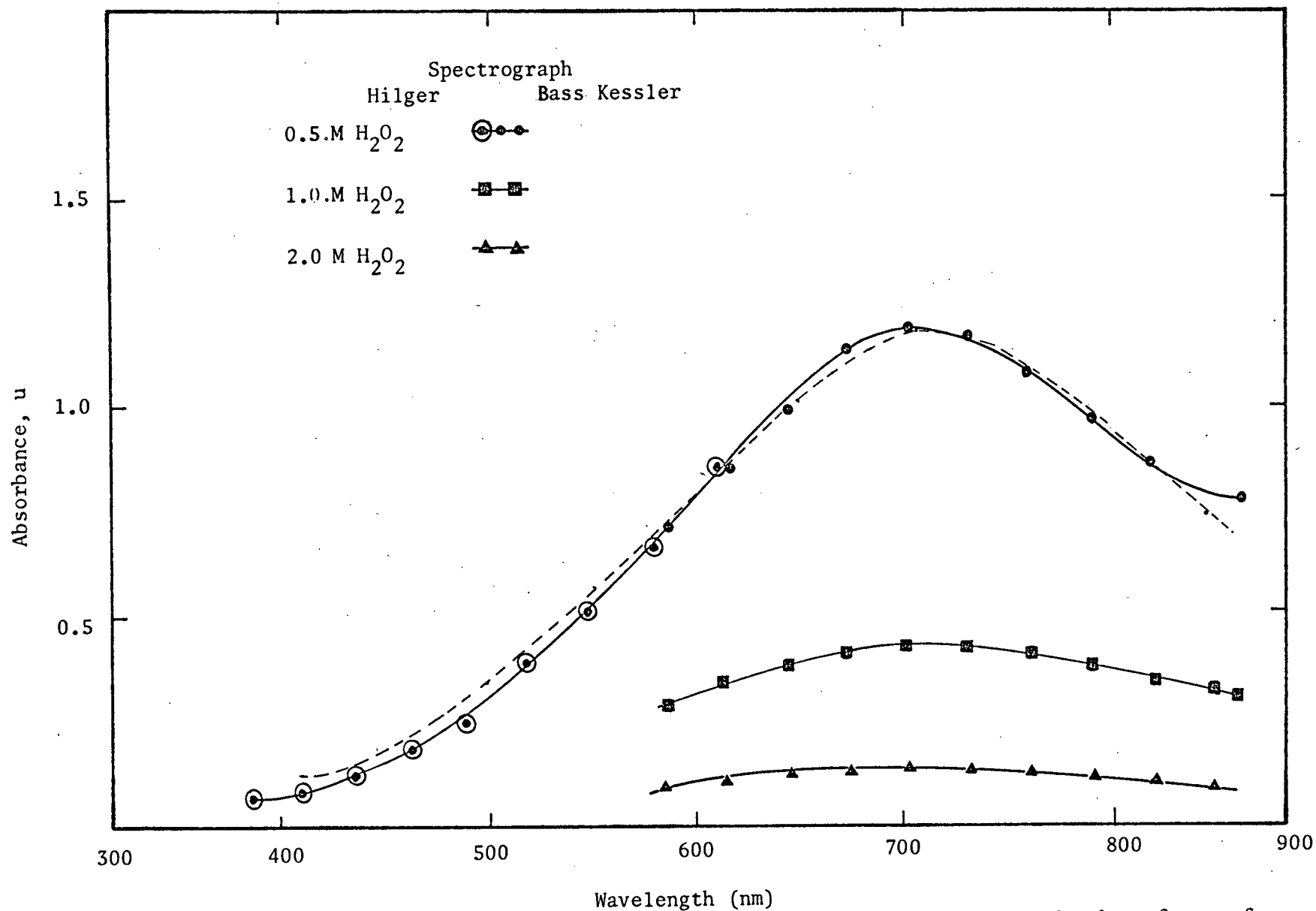
Figure 5-8 Hydrated Electron Spectra in H_2O_2 solutions. The dotted line is the data from reference (90).

but in the presence of scavengers when the disappearance of the electron

is very rapid, simple proportionality holds. Of the two published

hydrated electron spectra (90,91), better agreement was obtained

between this work and the more recent data of Hart et al, so that

the dotted lines superimposed on the spectra in figures 5-7 and 5-8

are from this source, normalization being made at the wavelength of

maximum absorption. A quantitative interpretation of these spectra

in terms of the $G\varepsilon$ product for the absorbing species requires the

numerical results of Chapter IV. The absorbance as a function of the

decay rate of the hydrated electron in perchloric acid solutions at

580 nm was simulated by numerical computer evaluation of equation (4-184).

$$
U = \log_{10} \frac{\displaystyle\int_0^c \int_0^{a_c} \Lambda \sin \frac{\pi}{c} t' \cos \frac{\pi}{2a_c} x \; dx \, dt'}{\displaystyle\int_0^c \int_0^{a_c} \Lambda \sin \frac{\pi}{c} t' \cos \frac{\pi x}{2a_c} \exp \left\{ - X \frac{\pi}{2b} \left\{ \frac{1}{k_1^{2+} \frac{\pi}{b}} - 2 \right\} v(x) \cdot \ell(t' + \frac{b}{2} - \frac{c}{2}) \right\} dx \, dt}
$$

The input data and its rationale are as follows:

(i) The dose-depth and Cerenkov depth distributions shown in figure 4-3

were used. The dose-depth curve follows the published data for 500 keV

electrons in water with a small increase in the deposited dose in the

first few lengths of a millimeter to account for the lower energy

electrons present in the electron pulse. The depth distribution of

Cerenkov emission is estimated from the Bethe equation, and thus is not

without a degree of uncertainty; however, there is no better available

method of calculation and no experimental data on which to base an estimate, so that this distribution was used. Cerenkov photons are also emitted at a specific angle to the track of the high energy electron. In these experiments, the angular distribution of light emission from the radiation cell shows only a spatial anisotropy of emission in the forward direction with no evidence of a Cerenkov cone. This behaviour is expected for low energy electrons which would be strongly scattered, thus destroying the details of the spatial anisotropy.

(ii) The dose-rate function is determined from the Faraday cup waveform. A sinusoidal function fits the dose-rate function derived from the square of the Faraday cup waveform very well (see figure 5-9), so that it is necessary to specify only the base width, b = 3.8 nanoseconds, and the total incident dose measured calorimetrically, which is 3.4×10^{19} eV cm^{-2}. The Cerenkov radiation pulse will be slightly shorter than the dose pulse, due to the presence of low energy electrons in the leading and tailing edge of the electron pulse. Energy analysis can only be done very roughly (see page 109) yielding a sinusoidal Cerenkov radiation pulse of base width, c = 3.2 nanoseconds, which is superimposed on the dose pulse in figure 5-9.

(iii) The rate of disappearance of the hydrated electron is described by a pseudo first-order decay constant k, which in concentrated acid is $k = k_8 [H^+]$ where $k_8 = 1.1 \times 10^{10}$ M^{-1} sec^{-1} from (4c), while in pure water, $k = \sim 5 \times 10^8$ sec^{-1} as suggested in (4c).

The results of this calculation for several values of the $G\varepsilon$ products, along with the experimental absorbances at 580 nm are shown
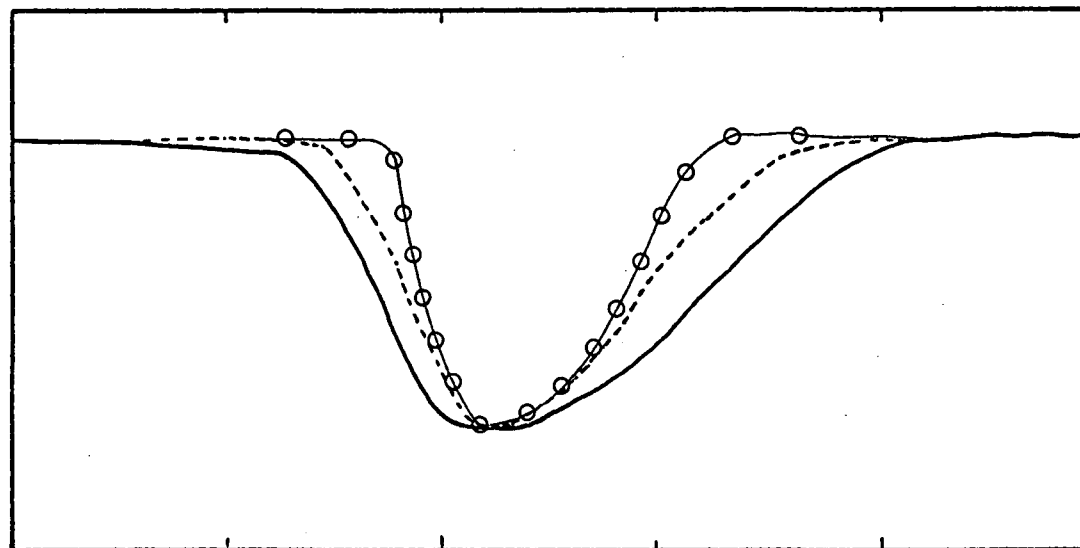
2 nanoseconds/div

Figure 5-9   Time dependence of dose deposition (dotted line)   as derived
from the Faraday cup waveform (solid line), open circles
Cerenkov radiation pulse.

in figure 5-10. The best fit is obtained for a $G\varepsilon$ product of

3.5×10^4, from which, using $\varepsilon_{580} = 1.1 \times 10^4$ M^{-1} cm^{-1} (90), the 100 eV

yield is $G = 3.2$. The estimated uncertainty in the $G\varepsilon$ product of 30%

(4-184) is principally affected by the experimental dose-rate and

Cerenkov emission functions, determined by the electron pulse shape, and

the Cerenkov depth distribution function. Although the former can be

measured quite accurately, sample calculations show that the absorbance

is sensitive to small changes in the Cerenkov emission pulse duration

contributing an error of $\sim$ 15%. In contrast, variations in the Cerenkov

depth distribution which is only approximated, cannot affect the $G\varepsilon$

product by more than $\pm$ 15%, because the range of probable Cerenkov

depth distributions is not large.

Because the $G\varepsilon$ product is directly proportional to the absorbance

when the rate of disappearance of the absorbing species $k > 10^9$ sec^{-1},

the relative initial hydrated electron yield in concentrated H_2O_2 as compared

to the rate in H_3O^+ is simply the ratio of their absorbances. Thus, the

quantitative reduction of the primary yield of hydrated electrons in

water can be calculated directly without the use of equation (4-184).

The results obtained is shown in figure 5-11, with the equivalent data from

the picosecond stroboscopic pulse radiolysis studies (4d) indicated by

the dotted line.

(b) Formamide

(i) Transient Absorption Spectra.

Preliminary investigations on pure formamide were undertaken in

conjunction with steady-state ^{60}Co γ-radiolysis experiments (92)
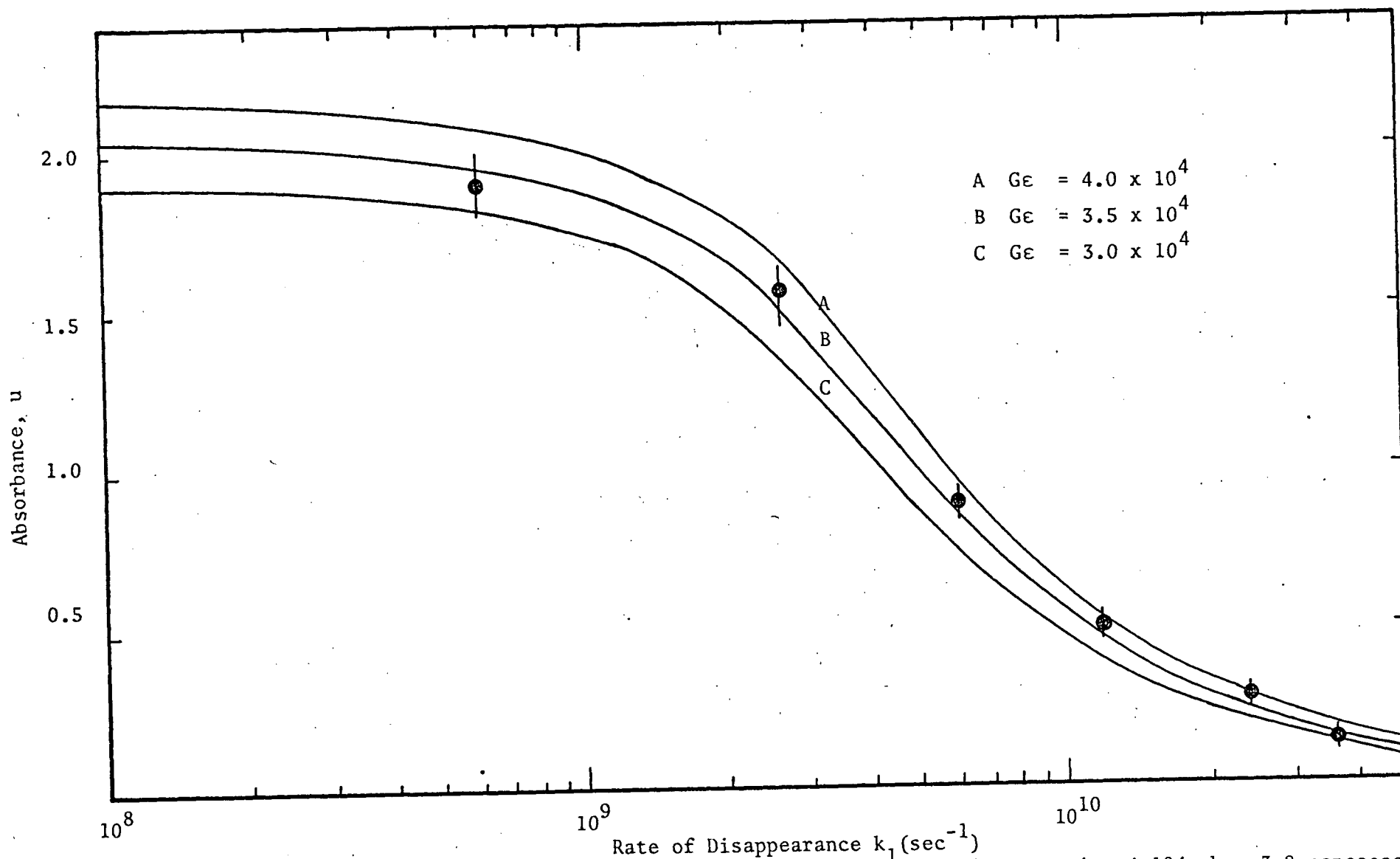
Figure 5-10   The simulation of the perchloric acid scavenging results using equation 4-184, b = 3.8 nanoseconds, C = 3.2 nanoseconds   dose = 3.4 x 10^{19} eV cm^{-2}.
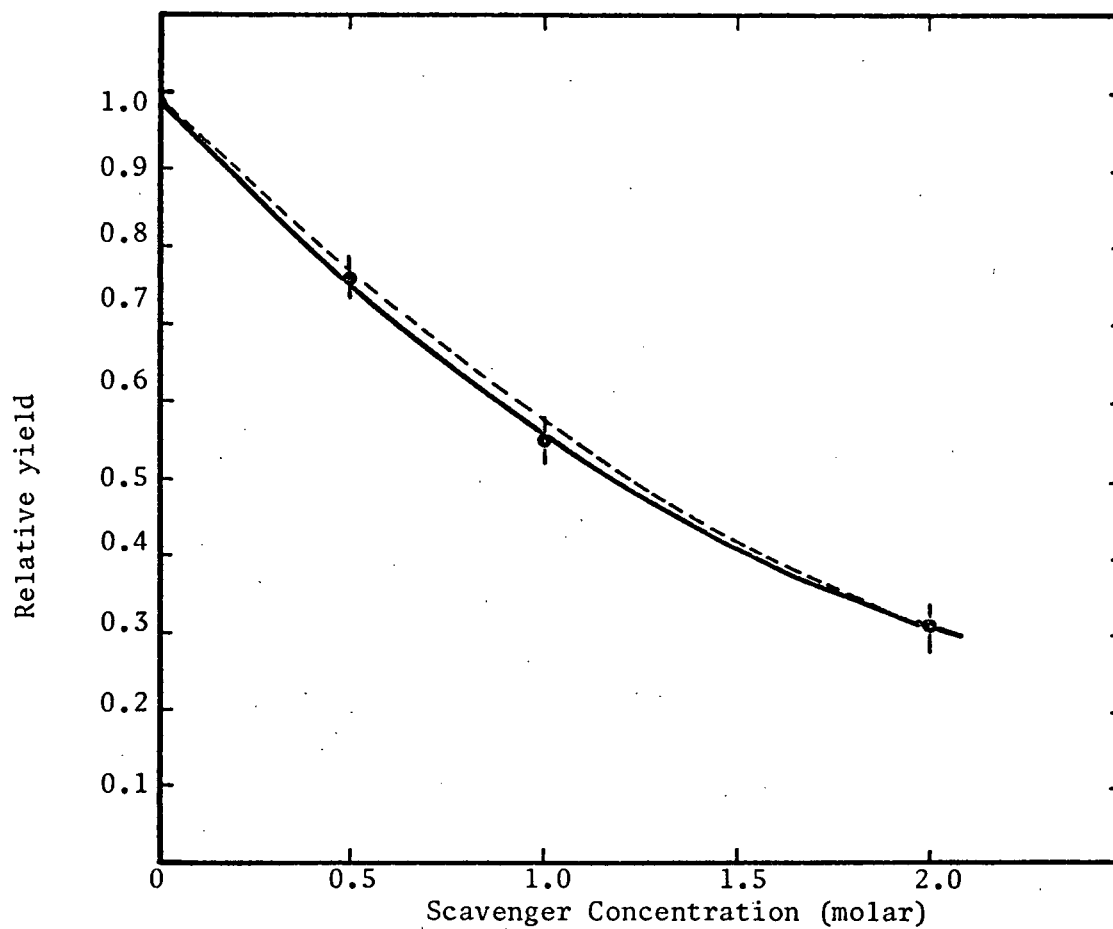
Figure 5-11 The diminution of the primary hydrated electron yield
measured in H_2O_2 relative to that in H_3O^+; the dotted line
shows the results reported in reference (4d).

in order to corroborate the substantial yield of solvated electrons, G = 3.3, indicated by nitrous oxide scavenging experiments in formamide. These experiments were carried out spectrographically, spanning the wavelength region 450 nm - 850 nm, and at a surface dose of $\sim 10^{19}$ eV cm^{-2}.

Within the limits of detection, U = 0.1, there was no absorption in the region 450 nm - 850 nm, from which it is estimated that the Gε product for any absorbing species would be less than 3 x 10^3. This observation is quite unexpected on the basis of the steady-state measurements, which might be interpreted to predict a Gε value of about 5 x 10^4 (92a). Subsequent study was directed towards the investigation of the possible existence of solvated electrons in formamide.

With the purpose of comparison to the more fully documented radiolysis of water, a series of formamide-water mixtures containing up to 50% water (by volume) were studied over the spectral range 300 nm - 850 nm. These experiments were carried out using the higher dose 5515 electron tube (3 x 10^{19} eV cm^{-2}), so that the minimum absorbance that could be detected, U = 0.1, corresponded to a Gε product value of < 10^3.

In the spectra obtained in pure formamide and the water-formamide mixtures, which are summarized in figure 5-12, two features should be noted. First, in pure formamide there is an absorption in the near ultra-violet slowly decreasing into the visible, with a very small shoulder at about 500 nm. This ultra-violet absorption is still not altered in shape in solutions containing up to 50% water, except that there is a slight increase in intensity in the blue with the addition of water. Secondly, an absorption spanning the visible and near infrared, very similar in shape to the spectrum
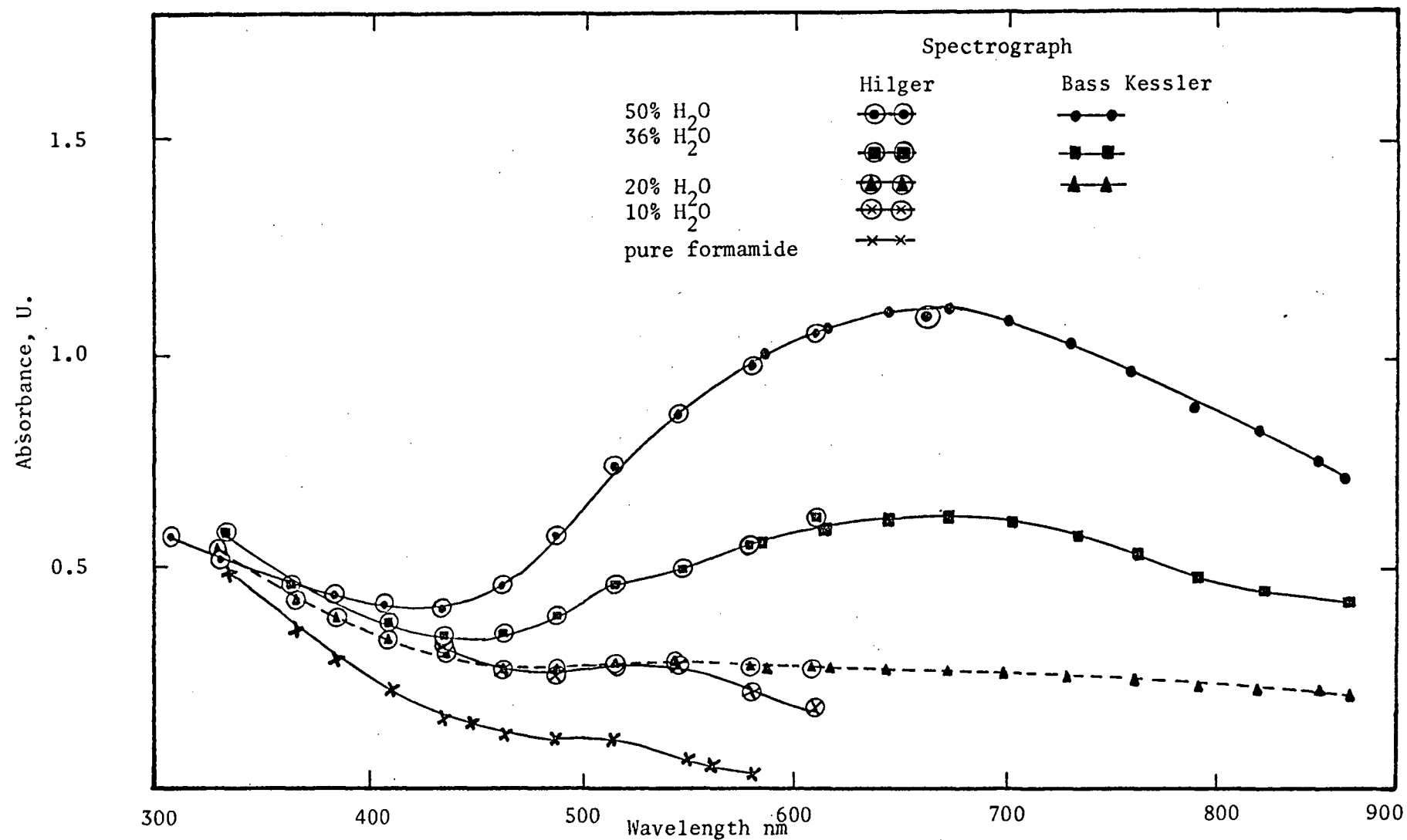
Figure 5-12   Absorption spectra observed in the pulse radiolysis of formamide-water mixtures.

of the hydrated electron in water but with an absorption maximum slightly

shifted towards the blue at 690 nm, grows in as the concentration of

water is increased. This effect is most unusual in that unlike any other

series of mixtures of polar compounds studied so far, (see for instance

(88b)), there is no gradual shift in the position of the maximum as the

composition of the mixture is varied. At low water concentrations

the weak band at $\sim$ 500 nm appears superimposed on the absorption band

whose peak is at 690 nm; as the water content increases the weak band

decreases in size and on reaching 50% water content it seems to have

disappeared.

Reference Cerenkov emission spectra were established for each

mixture in question, both by in situ scavenging of the absorbing

species by means of added solutes, and by using n-pentane, for which

calculations predict the same Cerenkov emission as formamide. In pure

formamide, acids such as trifluoroacetic and perchloric at molar

concentrations completely remove the weak absorption band at 500 nm

but only partially eliminate the absorption in the near ultra-violet.

This latter point indicates the presence of two overlapping peaks

in that region, one at about 300 nm and the other about 360 nm. The

aqueous formamide solutions showed similar scavenging behaviour with acids

in the blue and ultra-violet region as did the pure formamide, while

the absorption peaking at 690 nm could be scavenged by both

perchloric acid and hydrogen peroxide.

(ii) Nanosecond Pulse Radiolysis of Formamide-Water Mixtures.

In order to establish the life-time of the absorbing species
at 690 nm in the formamide-water a kinetic investigation was
undertaken on the nanosecond time-scale using the technique of kinetic
laser photometry at 633 nm (74). The decay of the transient absorption
in a series of mixtures, the compositions of which ranged from 50%
to 90% water, is shown in the oscilloscope traces in figure 5-13.
Although the phenomenon of delayed absorbance (93) is observed for the
higher water concentrations, linear first-order plots were obtained
for all mixtures once sufficient time had elapsed. The second-order
rate constant calculated for the reaction of the hydrated electron
with formamide from these data is $1.8 \pm 0.2 \times 10^7$ M^{-1} sec^{-1}, compared to
the two somewhat conflicting values of 10^6 M^{-1} sec^{-1} (94) and 4.2×10^7 M^{-1} sec^{-1}
(95) that have been previously reported. It is important to note that
this rate constant is independent of formamide concentration up to
about 12 molar, indicating similar kinetic behaviour over the entire
range.

Additional measurements on millimolar H_2O_2 and $HClO_4$ solutions
were made so that the generally accepted rate constants for the
reaction of these solutes with the hydrated electron could be compared
those experimental values measured in this work. The second-order rate
constants calculated from the oscilloscope traces shown in figure 5-13
are as follows:

$$k_{e^-_{aq} + H_2O_2} = 1.1 \pm 0.1 \times 10^{10} \ M^{-1} \ sec^{-1}, \ cf \ k_7 = 1.23 \times 10^{10} \ M^{-1} \ sec^{-1}$$

$$k_{e^-_{aq} + H_3O^+} = 2.2 \pm 0.2 \times 10^{10} \ M^{-1} \ sec^{-1}, \ cf \ k_8 = 2.3 \times 10^{10} \ M^{-1} \ sec^{-1}.$$

(a)

10 nanoseconds/div

(b)

10 nanoseconds/div

(c)

10 nanoseconds/div

(d)

20 nanoseconds/div

(e)

20 nanoseconds/div

(f)

10 nanoseconds/div

(g)

50 nanoseconds/div

All traces were measured using a
Tektronix 454 oscilloscope, vertical
deflection was 10 mv/div
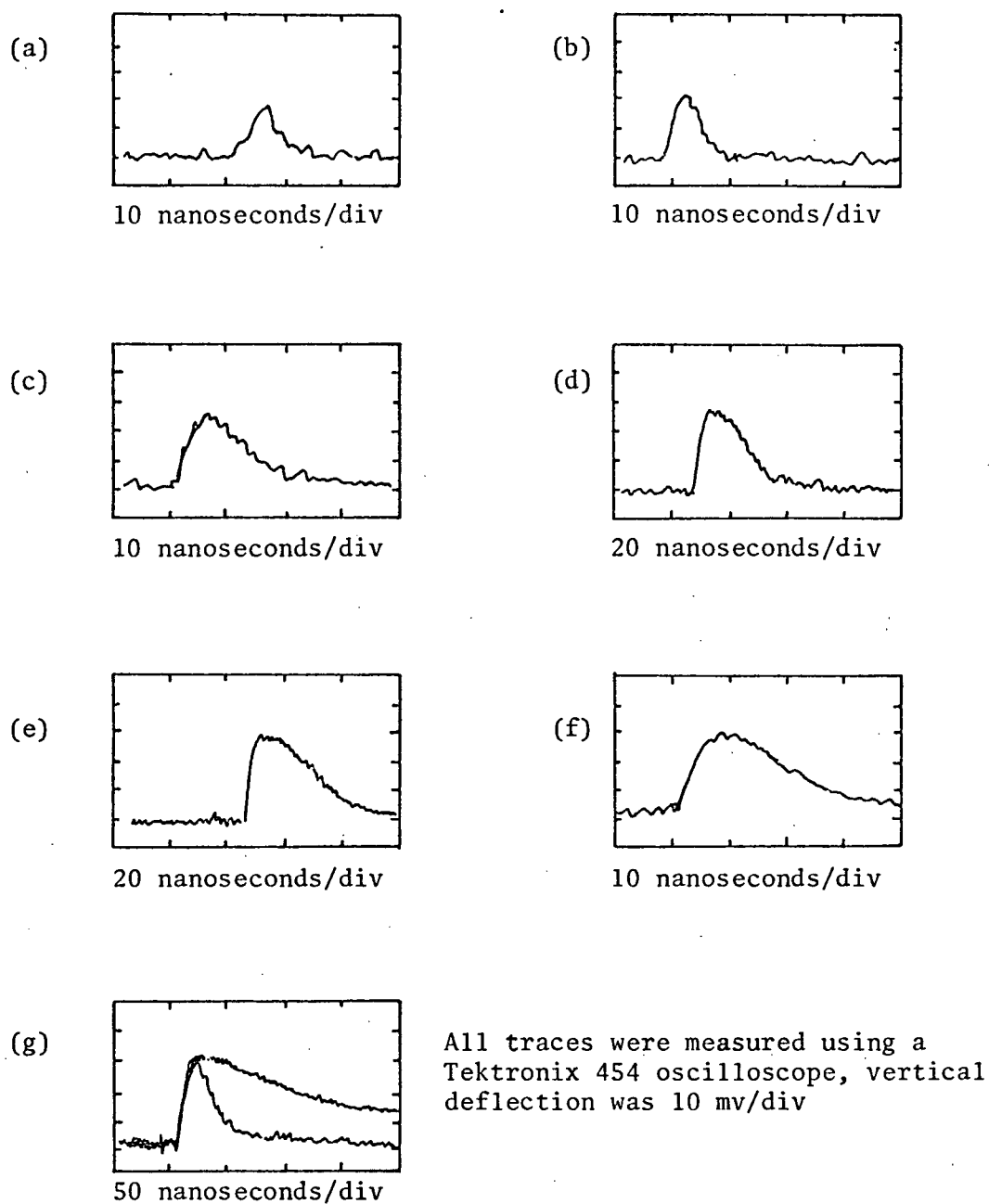
Figure 5-13 Oscilloscope traces from nanosecond kinetic laser photometry
studies at 633 nm, in aqueous solutions
(a) 12.6 molar formamide (50%)   (f) 4.5 millimolar H_2O_2
(b) 9.08 molar formamide (36%)   (g) upper trace pure water, lower
(c) 6.31 molar formamide (25%)   trace 2.04 millimolar $HClO_4$
(d) 3.78 molar formamide (15%)
(e) 2.52 molar formamide (10%)

The good agreement with the accepted literature values indicates the validity of the experimental method. Thus the rate constants obtained in these pulse radiolysis measurements for the disappearance of the transient absorption at 633 nm place the lifetime of the species giving rise to the absorption at 690 nm in the formamide-water mixtures on a nanosecond time-scale.

(D) Spectrophotometric Data

For quantitative Cerenkov reabsorption measurements on the solvated electron in pure water and the alcohols the spectrophotometric technique must be used. This is because the reciprocity law failure of photographic emulsions results in a significant overestimation of absorbances above $U \sim 1.5$ determined by the spectrographic method. Typical oscilloscope traces obtained in spectrophotometric measurements in pure water are shown in figure 5-14. The absorbed Cerenkov pulse has a width at half-height of 2.6 nsec compared to the reference Cerenkov pulse, 3.8 nsec, in qualitative agreement with the theoretical predictions of Chapter IV. Although the narrowing observed is quantitatively less than expected, thus indicating some distortion of the pulse shape, a comparison of the areas of the two pulses to give the ratio of the reference to absorbed Cerenkov intensities would not be seriously in error for pulses of equal intensity as discussed previously. Wratten neutral density filters were used to adjust the Cerenkov light intensity so that a pulse height of about 20 mv was always obtained. An absorbance was then calculated from the relative Cerenkov pulse-areas, arrived at by the product of the width at half-height and the peak height,
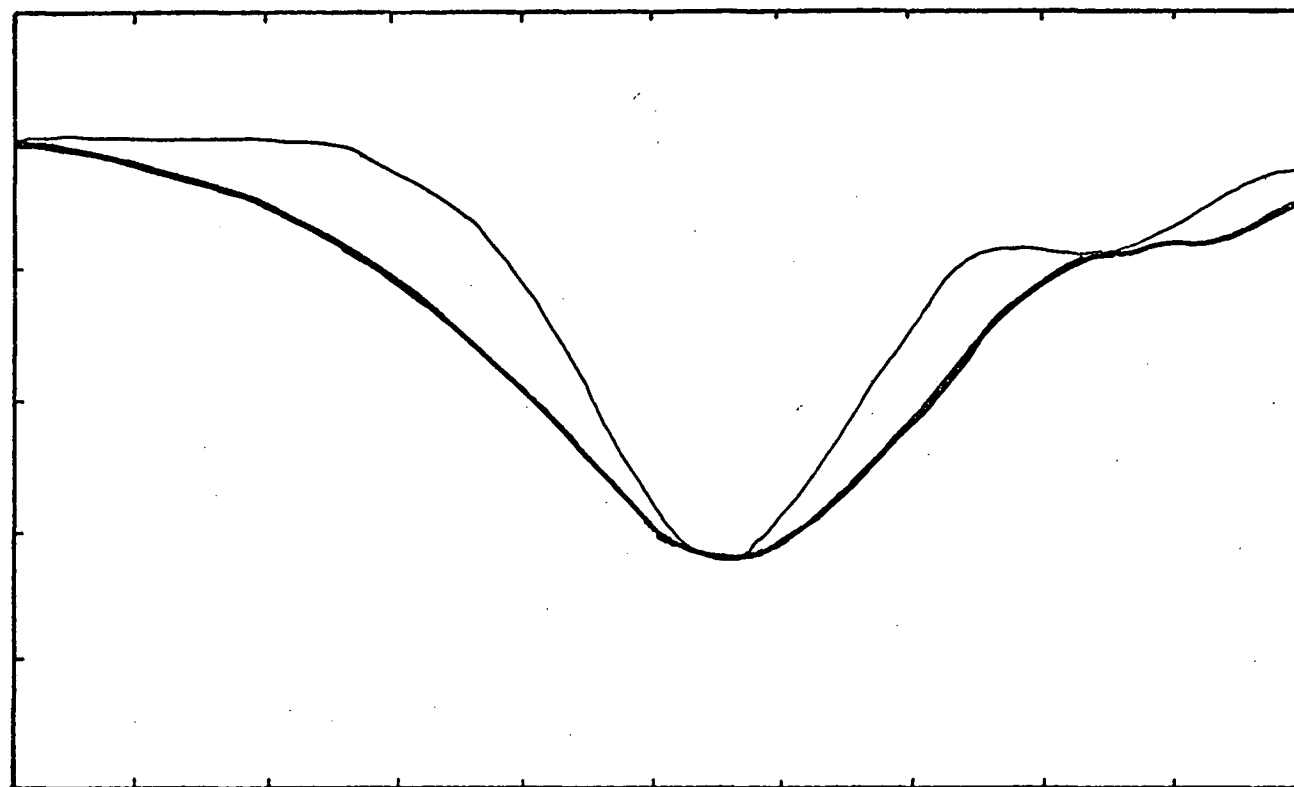
1 nanosecond/div

Figure 5-14   Typical spectrophotometric oscilloscope traces of absorbed and reference Cerenkov light pulses in water at 620 nm. The reference Cerenkov pulse, heavy line, was attenuated by a wratten neutral density filter A = 1.7.

combined with the attenuation of the neutral density filter as measured on the Cary 14 spectrophotometer.

The absorption spectrum of the hydrated electron in pure water shown in figure 5-7 was determined by this method. In addition a number of data points were obtained in perchloric acid solutions to compare with the spectrographic measurements. The agreement between the two techniques as illustrated in figure 5-7 is quite good, demonstrating their reliability.

When the rate of decay of the absorbing species is sufficiently slow ($k_1 < 10^9$ sec^{-1}), the absorbance U is proportional to the logarithm of the Gε product of the transient species, (see equation 4-52). Thus it is possible to estimate primary yields of solvated electrons in water and the alcohols relative to one another from absorbances measured in the pure liquid. The high solvated electron yields in these compounds required spectrophotometric techniques, so that absorbances were obtained either at the wavelength of maximum absorption, or at 630 nm with corrections to the absorption maximum from microsecond spectral data (88) if the maxima were at longer wavelengths. The reference Cerenkov intensities were derived from solutions containing high concentrations of appropriate scavengers, 2 molar $CHCl_3$ being used for the alcohols and 3 molar H_2O_2 for water. However, no attempt was made to compensate for any changes in the Cerenkov depth distribution in these different media, as these effects are expected to be less than the experimental uncertainty of the measurements. The results of this study are summarized in Table V, which also contains for comparative

purposes data from the picosecond stroboscopic pulse radiolysis technique (4c) and microsecond pulse radiolysis experiments (88).

Table V. Relative Solvated Electron Yields

Compound	$G\epsilon_{max}$ This work	G	$G\epsilon_{max}$ picosecond(4c)	$G\epsilon_{max}$ μsecond(88)	static dielectric constant ϵ_o
H_2O	1.00	1.00	1.00	1.00	80
methanol	.37	.42	.37	.36	34
1-propanol	.30	.43	.39	.25	21
2-propanol	.28	.38	.25	.27	19
1-butanol	.23	-	-	-	17
1,2-ethanediol	.32	.43	.36	.32	39
1,2,3-propanetriol	.42	-	-	-	43

Because of significant pulse-to-pulse variations in accelerator output at the time of this particular study, the results in Table IV are the mean of at least ten consecutive measurements, the estimated uncertainty being ± 10%.

(E) The Correlation of the Energy of Maximum Absorption for the Solvated Electron and the C.T.T.S. Band of the Iodide Ion

Although the analogy between the charge transfer spectrum of the iodide ion and the absorption spectrum is not a new idea (97,98,99), confirmation of this correlation has not been forthcoming because of a

lack of experimental data over a sufficiently wide enough range of
solvent properties. The purpose of this section is to present
some new solvated electron and iodide ion absorption spectra from this
work, as well as to tabulate what previous data had been available on
this subject. This material is summarized in Table VI reference
being made to other work by number, and to this particular study with
asterisks.

The correlation of the data in Table VI is best displayed
graphically by plotting the energies of maximum absorption for the solvated
electron and the iodide ion against each other as illustrated in figure
5-15, the numbers on the graph referring to Table VI and the error bars
corresponding to ±10 nm uncertainty in the wavelength of the solvated
electron absorption maximum.

(F) Everything Absorbs Somewhere

In the course of this work, many transient absorptions (especially
unwanted, interfering absorptions) have been observed qualitatively,
but have not been followed up with quantitative study, because the
information gained would not be directly applicable to the problem at
hand. However, this qualitative data has been included here in
Table VII so that these pitfalls may be avoided in future work or
provide the basis for suggestions for further study.
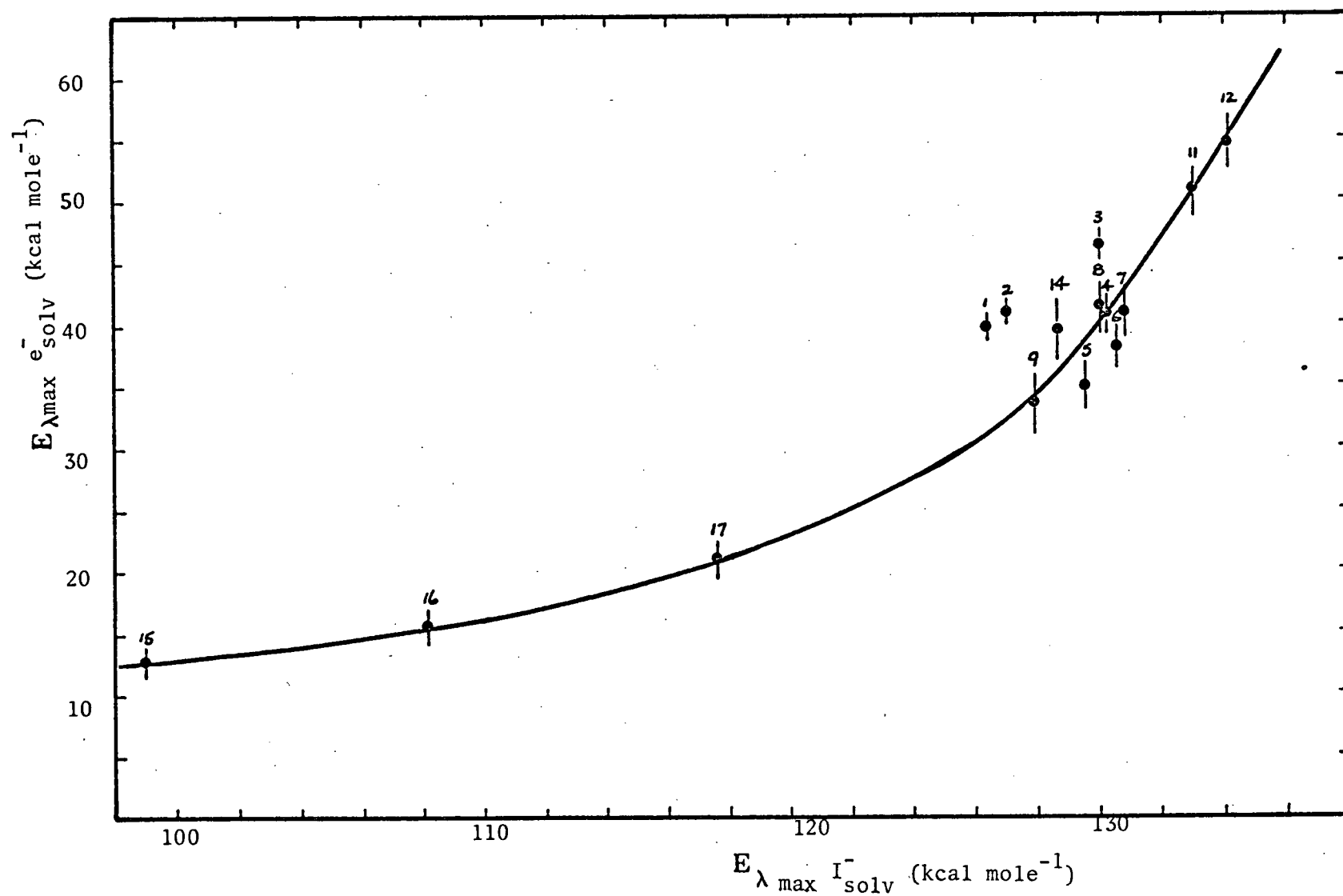
Figure 5-15 The Correlation between the Absorption Spectra of the solvated electron and the iodide ion in polar media.

Table VI   The Energy of Maximum Absorption of Solvated Electrons and Iodine Ions at $20^{\circ}C$

			The Solvated Electron			The Iodide Ion	
	Solvent	ε_o	λ-max (nm)	Energy λ-max (kcal mole^{-1})	Reference	Energy λ-max (kcal mole^{-1})	Reference
1	water	80	720	39.6	90,91,*	126.4	102
2	deuterium oxide	79.5	700	40.8	108	127.0	103
3	methanol	33.6	630	46.2	83	130.0	102
			620	46.0	*		
4	ethanol	25	799	40.7	88	130.2	103
5	1-propanol	19	740	38.4	88	130.5	*
6	2-propanol	21	820	34.7	88	129.5	107
			800	35.6	*		
7	1-butanol	17	680	41.9	88,*	130.8	107
8	3-methylbutanol		690	41.3	*	130.0	102
9	2-methyl-2-propanol	12.2	850	33.6	100	127.9	102
10	1-pentanol	13.9	660	43.2	*		
11	1,2-ethanediol	39.0	580	50.7	88	133	102
			560	51.0	*		

Table VI   The Energy of Maximum Absorption of Solvated Electrons and Iodine Ions at $20^{\circ}C$

	Solvent	ε_o	The Solvated Electron			The Iodide Ion	
			λ-max (nm)	Energy λ-max (kcal mole^{-1})	Reference	Energy λ-max (kcal mole^{-1})	Reference
12	1,2,3-propanetriol	54.1	525	54.4	88,*	134.1	102
13	1,3-butanediol		650	44.0	*		
14	2-methoxyethanol	17	720	39.6	*	128.6	102
15	hexamethylphos-phoramide	30	2200	12.8	101	99.0	*
16	ammonia	16	1830	15.5	106	108.1	105
17	ethylenediamine	14.2	1360	21.0	105	117.6	99

Table VII Some Radiation-Induced Absorptions

Material	Wavelength Region	Intensity	Suggested Identity
molar solutions of acetone in H_2O	blue and near U.V.	weak	acetone negative ion (109
acetonitrile	visible	medium	not a solvated electron
molar solutions of H_2SO_4 in H_2O	~450 nm	weak	$SO_4^{\bullet-}$ (110)
dimethylformamide	increasing into the near infrared	medium	?
dimethylsulphoxide	increasing into the blue	medium	?
N-methylformamide	increasing into the blue	very weak	?
diethyl ether	near U.V.	weak	?
1,4 dioxane	visible and near U.V.	weak	?
tetrahydrofuran	visible and near U.V.	weak	?
molar solutions of $NaNO_3$ in H_2O	blue and near U.V.	weak	?
molar solutions of $HClO_4$ in H_2O	blue and near U.V.	weak	?

CHAPTER VI

LIGHT EMISSION STUDIES ON PULSE IRRADIATED WATER

(A) Luminescence and Excited States in the Radiolysis of Water

The absence of any significant molecular mechanism of light emission in pulse irradiated water (and indeed in any other saturated polar media studied) is in agreement with previous studies of this aspect of radiation chemistry, under both continuous (111,112,113) and pulsed (69,80) conditions. This work extends the previous pulse radiolysis experiments in spectral range (from 220 nm - 850 nm), time resolution (< 2nsec) and radiation intensity (increased by a factor of 100), yet the conclusion is the same. Any molecular luminescence process (both short and long-lived) must have a 100 eV yield of less than 10^{-3}. Several excited species have been proposed as primary products following the radiolysis of water, which, in principle, should give observable emission.

(i) Calculations predict (114) that a large proportion of secondary electrons will have sub-excitation energies, and thus should produce highly excited water molecules in both singlet and triplet states as they are slowed down by the medium. Although gas phase studies indicate that the singlet states of water are all dissociative, the resulting fragments H and OH would in many cases have excess kinetic energy so that by analogy with the gas phase, hydroxyl

radical emission could be expected in the 300 nm region. In addition triplet water with an energy of $\sim$ 4 eV (115,116), excited directly by low energy electrons, might be expected to phosphoresce in the region of $\sim$ 400 nm.

(ii) Excited states of water will also be created following recombination of electrons and H_2O^+. If this is geminate recombination, a highly excited singlet species will be produced, rapidly dissociating into H and *OH; in the high density of ionization of a blob, recombination with other free electrons could also yield triplet water, depending on their relative spin states.

(iii) Finally, there is the fate of the positive ion H_2O^+. This species will probably be formed with a wide energy range, depending on the electronic origin of the ionized electron. It is suggested that this positive ion rapidly undergoes an extremely fast ion-molecule reaction with the surrounding solvent to produce H_3O^+ and OH (32), so that the excess energy of the parent ion would likely be transferred to the OH radical before deactivation could occur.

Recently reported luminescence from films of ice at 77°K excited by low energy electrons (84) lends evidence to support some of these excitation mechanisms. A band at 280 nm with an onset at $\sim$ 9 eV is attributed to .OH emission ($^2\Sigma^+ \to {}^2\pi$) from an excited .OH radical produced in the dissociation of excited water molecules

$$H_2O^* \to H(^2S_{\frac{1}{2}}) + OH(^2\Sigma^+) \tag{16}$$

while a broad band at 400 nm requiring greater than $\sim$ 12 eV

excitation energy is thought to have originated from the lowest

triplet state of water, formed perhaps from electron-ion recombination.

Unfortunately without an estimate of the radiation yield for these

processes, the relevance of this data to the radiolysis of water

cannot be easily determined. However, the strong evidence presented

in this work for the absence of any such fluorescence or phosphorescence

in the liquid state, would indicate that excited species (especially

small entities which would be expected to have long lifetimes) are

rapidly and efficiently quenched in liquid water. Consequently such

proposed excited states as $^1H_2O^*$ (117,118,119,120) and $^3H_2O^*$ (117b),

or other excited radical fragments, cannot play any significant role

in the radiation chemistry of liquid water. This conclusion is also

consistent with the fact that fluorescence from aqueous sodium

salicylate solutions has been shown to originate exclusively from direct

excitation of the salicylate ion by the primary high energy radiation (82).

Thus there is no indication of any energy transfer from solvent to

solute in the radiolysis of water, which is further evidence for the

absence of long-lived excited states in the radiolysis of liquid water.

(B) Cerenkov Radiation Calculations

The Cerenkov radiation calculations in this thesis were

undertaken in order to provide a basis for the interpretation

of the observed Cerenkov luminescence since the few theoretical

treatments available are derived for much higher energy electrons and

quite different radiator conditions. Because the high energy electrons

are completely stopped in the radiating medium, it was necessary to include

the effects of slowing down in the theory describing Cerenkov emission. Accordingly it has been possible to explain both the observed energy dependence of the Cerenkov emission in water (69) and the relative Cerenkov radiation intensities in solvents of different densities and refractive indices. In non-absorbing media, the effects of dispersion have been shown to be very small; in water for example, significant deviations from the λ^{-2} spectral distribution occur only for wavelengths less than 250 nm (figure 4-5), thus demonstrating the potential use of Cerenkov radiation as both a relative (77) and absolute (121) standard light source.

The detailed calculation into the region of anomalous dispersion shows that the possibility of significant radiation chemical effects due to reabsorbed Cerenkov radiation in the vacuum ultra-violet is extremely unlikely, because of the very small yield of such high energy photons (G $\sim 10^{-2}$, in complete agreement with the total estimated photon yield (17) over all spectral regions of G $\sim 2 \times 10^{-2}$).

Finally the numerical check of the inclusion of quantum mechanical corrections to the theory of Frank and Tamm verifies the assertion (17) that such effects will be negligible, even for low energy electrons.

These theoretical studies form the basis for a complete understanding of the properties Cerenkov light emission induced by low kinetic energy electrons. It is shown that most of the characteristics of Cerenkov emission from very high energy electrons ($\sim$ 100 MeV) retained, but the rapid deceleration of the lower energy electrons (0.5 MeV) with which this work was carried out, results in a modified dependence of the photon yield. Thus, under these circumstances the density of the medium must

also be included, along with the refractive index and the energy, in the calculation of the Cerenkov emission intensity.

CHAPTER VII

PULSE RADIOLYSIS STUDIES ON POLAR LIQUIDS

(A) The Correlation of the Spectral Properties of Solvated Electrons

Although there have been many theoretical treatments of solvated electron absorption spectra, because most of these models are individually derived in an a posteriori manner from the characteristic broad solvated electron absorption spectrum in a particular medium, no successful physical correlation of the spectral properties of solvated electrons over the complete range of solvents in which they are observed has been predicted as yet. For example, in the dielectric continuum models (54), the binding energy of the solvated electron will depend primarily on the static dielectric constant ε_0, and indeed, among the simply aliphatic alcohols a rectilinear correlation of the photon energy corresponding to the wavelength of maximum absorption and ε_0 has been observed (88a). However, with the addition of data for the longer chain alcohols and other polar compounds including the amines and water, this relationship breaks down as shown in figure 7-1 (the points are numbered according to Table VI). Another instance of the inadequacy of the dielectric continuum model is illustrated by comparing the absorption spectra of solvated and trapped electrons in water and crystalline ice (122). Because of the low value of the static dielectric constant in ice $\varepsilon_0 \sim 3$ at $77^{\circ}K$, the trapped electron would be expected to absorb far in the infrared, whereas its absorption is instead slightly shifted to
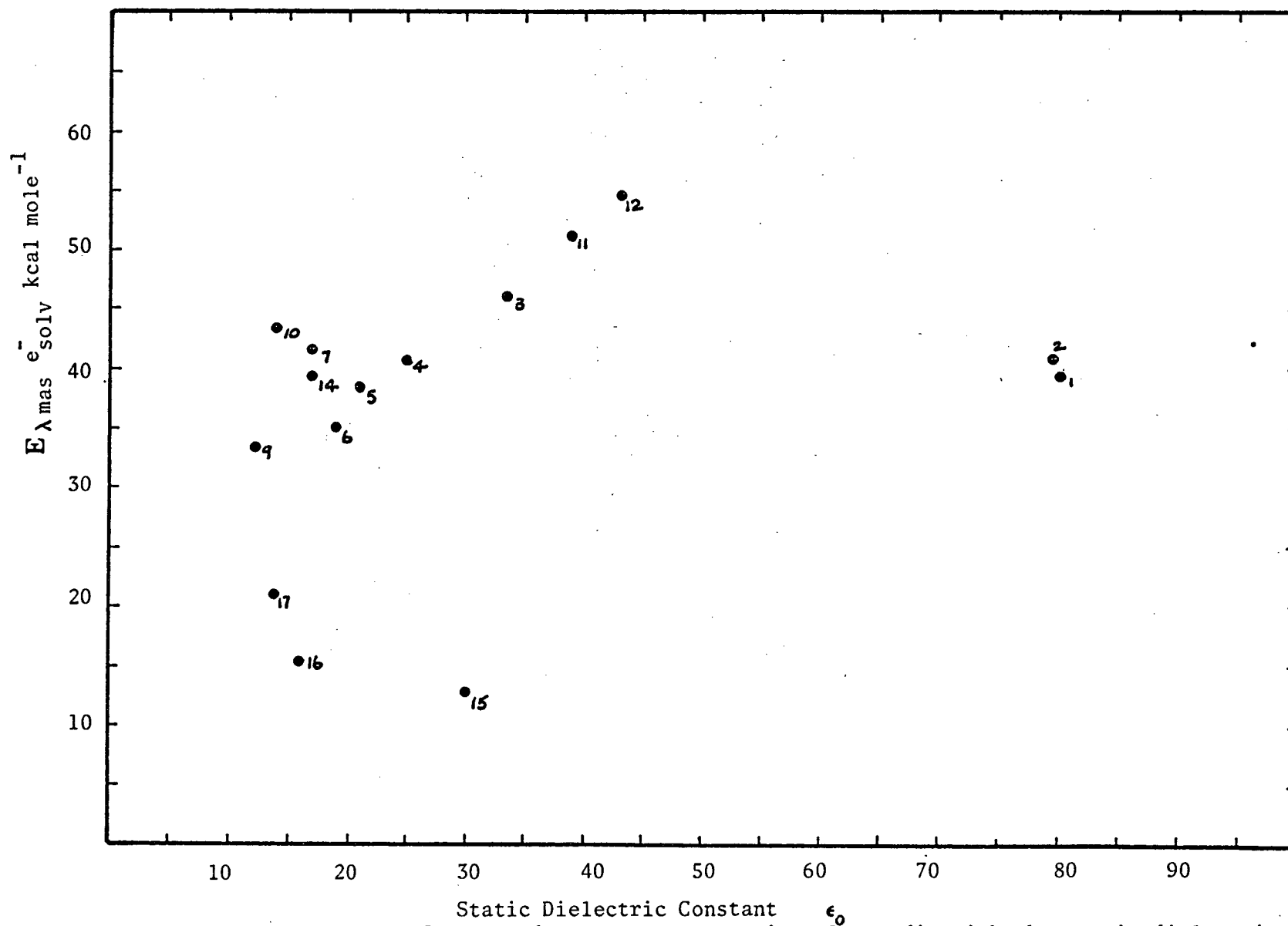
Figure 7-1 The Correlation of Solvated electron spectra in polar media with the static dielectric constant ϵ_o.

the blue by 80 nm with respect to the hydrated electron in water. The simple deduction from these experimental results on solvated electron spectra is that some short-range structural features of the medium must be included in the theory, along with the long-range interactions due to bulk dielectric properties. For instance, in what has been described as the semi-continuum model (123) including both long and short-range effects, it has been possible to predict the positions of the wavelengths of maximum absorption/both the hydrated and trapped

for

electrons in water and ice, in a single, self-consistent calculation. Clearly, this is the desirable theoretical approach for understanding electron stabilization, however, the problem arises that in other polar media the required structural details are not available. Moreover due to the complexity of the calculations themselves, it would appear that no simple correlation of solvated electron spectral data could be possible on this basis. Therefore, a more empirical approach appears necessary.

Recalling the analogy which was originally proposed (97) between the absorption spectra of the solvated iodide ion and the solvated electron, with the availability of both new and more reliable data, this correlation shown in figure 5-14 accounts quite well for the inconsistencies illustrated in figure 7-1. In fact the spectrum of the iodide ion shows exactly analogous trends as does the spectrum of the solvated electron under the effects of increased pressure (a blue shift), increased temperature (a red shift) and the addition of inorganic solutes (a blue shift), (99).

Such agreement is entirely consistent with the origins of both

the iodide ion and solvated electron spectra as proposed below.

The quantum absorbed by the iodide ion is about 50 kcal above the

gas phase ionization potential of I^-, thus giving rise to a charge-

delocalized excited state extending over the neighbouring solvent

molecules and centred on the iodine atom. This excited state decays

either by a radiationless transition to give the I^- ion or dissociates

into an iodine atom and solvated electron in a solvent cage (102). Altern-

atively one may envisage the initial excitation as a photoionization

producing an iodine atom and a free electron which rapidly becomes

solvated in close proximity to the iodine atom (102). In view of

recent experiments showing that the time scale of electron solvation

in water is only a few picoseconds (4c,62) the choice between these

two models is strictly intuitive, because if electron solvation

is this fast in principle there would be no observable difference between

the two mechanisms. Of significance to this study is that the

photoionization energy required for charge-transfer to the solvent

(C.T.T.S) must be related to the electron stabilization properties

of the solvent, and hence the correlation between the iodide ion

absorption spectrum and the solvated electron absorption spectrum is

proposed. In this way it is possible to rationalize the wide variations

in solvated electron spectra between water, the alcohols, and the amines,

the iodide ion spectra reflecting the short-range structural differences

in the binding of solvated electrons among these media by the variations

in the energy required for charge transfer to the solvent. The only

deviation from this correlation occurs for water and methanol (although

H_2O, D_2O, and methanol are all self consistent) where the iodide ion
spectra are at a lower energy than expected. This discrepancy
is probably due to the structural differences between iodide ion
solvation and electron solvation for these very small molecules, where
the additional bulk of the iodine atom would be expected to be more
important (and in fact X-ray diffraction studies on the iodide ion in
liquid water (124) show considerable expansion of the water structure
around this species). This would cause a slight reduction of the
C.T.T.S. transition energy for the iodide ion as a result of the expanded
solvation sheath. In larger molecules such as the higher alcohols,
because of the steric hindrance of the alkyl group, the molecular
aggregation of the solvating molecules is rather less pronounced
so that such effects would not be expected to occur.

More quantitative information from this correlation with the
iodide ion is unlikely to arise from optical spectroscopic studies
alone. Other techniques such as N.M.R. and perhaps X-ray diffraction
studies (125) which yield specific details of the microscopic interactions
of ion solvation will be required, since the optical absorption spectrum,
although very sensitive to variations in solvation, yields little direct
information about their origins. Nevertheless, the successful
correlation of the spectral properties of solvated electrons in this
very wide range of polar media constitutes a promising and significant
step towards the characterization and interpretation of many of the
physical properties of the solvated electron. It thus remains to be
seen how future spectral data for solvated electrons in other unexplored
polar liquids test the generality of this correlation.

(B) <u>The Solvated Electron in Formamide?</u>

Although solvated electrons are by now well documented
intermediates in the radiolysis of many polar organic liquids, such
studies have been confined to saturated compounds of relatively low
dielectric constant ($\varepsilon_0 < 40$) such as the amines and alcohols,
where the reactivity of the solvated electron with the solvent molecules
is low. With the aim of characterizing the solvated electron in a medium of
very high dielectric constant, a steady-state radiolysis investigation (91)
on liquid formamide ($\varepsilon_0 = 109$) was undertaken in this laboratory, the
results of which indicated a substantial free ion yield, G = 3.3.
This observation was consistent with the high dielectric constant of the
liquid, within the framework of models describing electron escape that are
based on the static dielectric constant (128). However because of the
less direct nature of steady-state radiolysis studies, it was not possible
to differentiate between the two alternative mechanisms for the
scavenging results obtained (92), that is, between a solvated electron
or solvent anion (or dissociation product of this anion) as the primary
reducing species. Pulse radiolysis measurements would give more direct
information towards the identification of this intermediate. Thus a
solvated electron in formamide, by analogy with other polar media would
be expected to exhibit a broad and intense absorption spectrum in the
visible or infrar-red, whereas an anion would be more likely to absorb
weakly in the blue and ultra-violet (127). Unfortunately because of the
very strong solvent absorption in liquid formamide below 300 nm an iodide
ion C.T.T.S. spectrum could not be determined satisfactorily, so that

no prediction of the wavelength of maximum absorption for the
solvated electron could be made.

The steady state scavenging experiments had implied that the
lifetime of the reducing species must be greater than 10^{-7} seconds,
so that experimental time resolution would pose no limitation to the
detection of this species in pulse radiolysis, although no absorption
signal could be detected at 633 nm in the pulse radiolyzed pure liquid
using the kinetic laser photometry technique (92). In view of these
results, it was tentatively suggested (92a) that solvated electrons
might be formed only in a secondary process. The situation may be
clarified by the observations.

The very weak radiation-induced absorption in the blue and near
ultra-violet observed in pure formamide (figure 5-12) and the absence
of any other absorption, up to 850 nm from these Cerenkov reabsorption
studies and up to 2000 nm with conventional nanosecond pulse radiolysis
techniques (126) clearly indicate that the reducing species observed
in the steady radiolysis of formamide cannot be the solvated electron.
This conclusion is also in keeping with the lifetime of 1.5 nanoseconds
calculated for the solvated electron in pure formamide using the rate
constant for the disappearance of the hydrated electron in concentrated
formamide water solutions, measured in this work,

$$k_{e^-_{aq} + formamide} = 1.8 \pm 0.2 \times 10^7 \ M^{-1} \ sec^{-1}.$$

However, it is surprising that no absorption due to the solvated
electron was observed in the Cerenkov self-absorption measurements,
since this technique has a far shorter temporal capability than 1.5 nanoseconds.

To further investigate this anomaly, a series of formamide-water
mixtures was pulse irradiated in order to follow the growth of the
expected solvated electron absorption with increasing water concentrations.
The resulting spectra illustrated in figure 5-12, are attributed to the
solvated electron absorption because of their characteristic breadth
and their suppression by electron scavengers such as H_2O_2 and H_3O^+.
These spectra are very unusual in that unlike any other known series
of mixed polar solvents, the absorption spectrum simply grows in
magnitude without any spectral changes as the concentration of water is
increased, while the formamide spectrum in the ultra-violet remains
essentially unaltered. In previous studies of mixed polar media
(88b), the effect of changing composition is to progressively shift
the wavelength of maximum absorption of the solvated electron from
that characteristic of the predominant solvent towards that of the
added co-solvent as its concentration is increased. The implication
of this effect is that solvated electrons are not formed in pure formamide,
but rather the thermalized electrons escaping from the primary ionization
event are immediately scavenged by the ubiquitous formamide molecules
to produce a negative ion. This negative ion (or some long-lived
fragment) is the primary reducing species that was observed in steady-
state radiolysis experiments. With the addition of molar concentrations
of water, electron solvation will become possible in microscopic regions
of high local water concentration, resulting in an observable yield of
solvated electrons, which then react with the formamide molecule at the
rates expected from pulse radiolysis studies of dilute formamide-water

mixtures. This very rapid pre-solvation scavenging of thermalized electrons by the formamide molecule could be expected to occur because of the readily available low energy orbitals in such an unsaturated species. Such reactivity would not necessarily be related to the rate constant for reaction between a molecule and a solvated electron. Rather, it is observed that all unsaturated molecules or ions exhibit this scavenging effect in reducing the primary yield of hydrated electrons in water, as observed in this work for H_2O_2 (see later) and more generally for solutes such as acetone, NO_3^- and Cd^{2+} (4d).

Finally a tentative assignment of the absorption spectra observed in pure formamide can be made in the framework of this proposed mechanism. The weak absorptions peaking at about 400 nm and 500 nm, which may be scavenged by acids, are probably due to the formamide anion or a fragment thereof, while the absorption peaking at $\sim$ 300 nm, which is unaffected by the addition of electron scavengers, is more likely due to some radical species.

The observed results and proposed mechanisms of this work conflict with a microsecond pulse radiolysis study of formamide previously reported (94). In this work an absorption at 550 nm with $G\epsilon \sim 5 \times 10^4$ M^{-1} cm^{-1} $(100$ $eV)^{-1}$ and decaying with a first-order rate of 1.9×10^4 sec^{-1} is attributed to the solvated electron in formamide. In addition, the reported rate constant for the reaction of the hydrated electron with formamide in dilute aqueous solution is $< 10^6$ M^{-1} sec^{-1} as compared to 1.8×10^7 M^{-1} sec^{-1} determined from this work and 4.2×10^7 M^{-1} sec^{-1} reported elsewhere (95). The origins of this variance are not immediately understood. However, perhaps the main difference arises from the experimental conditions used in the former work (94). That is, all of these experiments were carried out in

saturated solutions of hydrogen gas which at the estimated solubility in formamide might produce a small steady-state concentration of solvated electrons from negative ions as follows:

$$H-C{\overset{O}{\underset{NH_2}{\diagup}}} \ + \ H_2 \ \longrightarrow \ H_2O \ + \ e^-_{solv} \ + \text{ radical fragments}$$
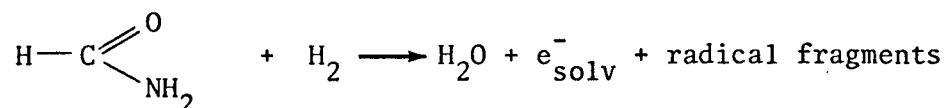
This is by analogy with the proposed single step reaction in water

$$O^- \ + \ H_2 \ \longrightarrow \ e^-_{aq} \ + \ H_2O$$
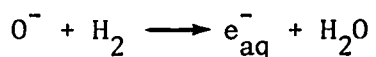
for the conversion of OH to e^-_{aq} by the two well documented reactions below.

$$OH \ + \ H_2 \ \longrightarrow \ H_2O \ + \ H\cdot$$

$$H\cdot \ + \ OH^- \ \longrightarrow \ e^-_{aq}$$
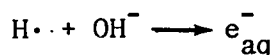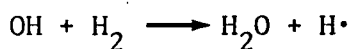
However the differences between the work in (94) and this work are ultimately rationalized, other microsecond pulse radiolysis experiments (96,126) are in good agreement with the results reported here and are also consistent with conclusion that solvated electrons are not formed as primary species in the radiolysis of formamide.

It might be anticipated that the very rapid presolvation scavenging as observed in formamide would be a general property of any molecule with low energy vacant orbitals, regardless of its reaction rate constant with a solvated electron. Thus the radiation chemistry of polar unsaturated liquids in which solvated electrons might have been expected (92a)

should be interpreted in terms of solvent anions. Steady-state radiolysis measurements of the chemical reducing yield would therefore be a reflection of the primary ionization yield, as long as no secondary reactions interfere with the chemical scavenging of these anions.

CHAPTER VIII

SUBNANOSECOND STUDIES ON AQUEOUS AND ALCOHOLIC SOLUTIONS

Although of a phenomenological nature, the spur diffusion model has been successfully employed in the rationalization of most radiation chemical yields and experimentally observed kinetic effects (reference (44) gives the most complete summary of recent work). The basic feature of this model is the concept of an inhomogeneous initial distribution of primary species in small regions of very high local concentration known as spurs; these are the result of the random sequence of discrete energy deposition, characterizing the transfer of energy from a high energy electron. In order to account for the long time-scale chemical yields (44) and the product yields in very high scavenger concentration studies (43) it is necessary to postulate a primary yield of hydrated electrons in water of G $\sim$ 5, of which about 50% disappear by intraspur reactions within a nanosecond. Similar arguments may also be advanced for the alcohols, in which a primary solvated electron yield of G $\sim$ 5 has also been proposed (127). However recent direct kinetic observations in the temporal range 20 to 300 picoseconds suggest that significant modifications of the spur diffusion model may be necessary (128) with regard to this primary solvated electron yield and, as a consequence, the ensuing kinetic description of intraspur reactions. Because of the novel departure from previous pulse radiolysis techniques in the stroboscopic, picosecond pulse radiolysis apparatus used for these measurements, the results might

be challenged on the grounds of their unique origin.

The results in this thesis offer the first direct, comparative evidence from more conventional radiolysis conditions, to be considered with the results from the stroboscopic picosecond technique, thus allowing a more definitive interpretation of the combined set of observations.

(A) Water

(1) Acid Scavenging Studies

The observation of hydrated electron absorptions in molar concentrations of H_3O^+ demonstrates quite clearly the temporal capabilities of the Cerenkov self-absorption technique. Using the mathematical model summarized in equation (4-184), the diminution of the absorption due to the hydrated electron with increasing $HClO_4$ concentration is consistent with a constant $G\varepsilon$ product of $(3.5 \pm 1) \times 10^4$ molar^{-1} cm^{-1} (100 eV)$^{-1}$ at 580 nm and a rate constant of $(1.2 \pm 0.4) \times 10^{10}$ M^{-1} sec^{-1} for the reaction of the hydrated electron and H_3O^+. Up to the limiting acid concentration of 3 molar (corresponding to a half-life for the hydrated electron of $\sim$ 20 pico-seconds) the absorption spectrum does not vary perceptibly from that obtained in microsecond experiments (89,90), except that it is increasingly shifted to the blue by higher acid concentrations. This shift is indeed predicted by the iodide ion - solvated electron spectral correlation (Chapter VII).

The discrepancy in the value of the rate constant for hydrated electron scavenging by H_3O^+, between the value of 1.2×10^{10} M^{-1} sec^{-1}

implied by these results and the higher figure of $2.2 \times 10^{10} M^{-1} sec^{-1}$ measured directly in nanosecond pulse radiolysis experiments (p 162) is not caused by some experimental artifact. Rather it is probably due to the microscopic inhomogeneity caused by local depletion of H_3O^+ on this very short time scale. A theoretical description of the effects of diffusion on the observed reaction rates under conditions of microscopic inhomogeneity has been given (130). Thus in the case of hydrated electron scavenging by H_3O^+ as exists with molar concentrations of acid, the time dependence of the observed reaction rate constant would be

$$k(t) = \frac{4\pi\rho D'}{1 + \frac{4\pi\rho D'}{k}} \left[1 + \frac{\rho}{1 + \frac{4\pi\rho D'}{k} \sqrt{\pi D' t}} \right] \qquad (8-1)$$

where D' = the relative diffusion coefficient of H_3O^+ and e^-_{aq}

ρ = the sum of the reaction radii of H_3O^+ and e^-_{aq}

k = the observed rate constant under conditions of homogeneous reaction.

With microscopic depletion of the H_3O^+ ions in the vicinity of a spur, the rate constant given by (8-1) will approach a steady state value k',

$$k' = \frac{4\pi\rho D'}{1 + \frac{4\pi\rho D'}{k}} \qquad (8-2)$$

Using the parameters $D' = 1.0 \times 10^{-4} cm^2 sec^{-1}$ and $\rho = 300$ picometers, this equation predicts a steady state rate constant k', about one-half

of the long time scale rate constant k. Furthermore, substitution of

the same values of D' and ρ in equation (8-1) shows that this steady

state situation corresponding to H_3O^+ depletion is achieved very rapidly,

because the time-dependent rate constant is diminished to within

20% of the steady rate constant in $< 10^{-11}$ seconds. Quantitative

agreement of the predicted steady state rate constant and that observed

in picosecond pulse radiolysis experiments was obtained by adjusting

the parameter ρ for the best fit. However the qualitative prediction

of a reduction in the rate constant remains unaltered, over the entire

range of physically possible reaction radii, and the choice of ρ = 300

picometers is quite a reasonable one.

The measured $G\varepsilon$ product at 580 nm yields a 100 eV yield G = 3.2 ± 0.9,

using the microsecond value of ε_{580} = 1.1 x 10^4 (90). Although there

is a substantial experimental uncertainty in this figure, within these

limits, it is definitely in conflict with the predictions of the spur

diffusion model (44), but before discussing the implications of this

conflict the H_2O_2 scavenging experiments will be presented.

(2) H_2O_2 Scavenging

In contrast to H_3O^+, hydrogen peroxide scavenging significantly

reduces the hydrated electron yield with increasing concentration

(figure 5-6). This phenomenon is attributed to pre-solvation scavenging

of thermalised electrons (4d), which does not occur with H_3O^+ because

of its stable, closed shell electronic state, but is quite possible

with species such as H_2O_2 with readily available low energy molecular

orbitals to accommodate the electron. That this is simply not a rate constant effect between H_3O^+ and H_2O_2 for hydrated electron scavenging is conclusively shown by direct kinetic observation (4d) of the hydrated electron decay in H_3O^+ - H_2O_2 solutions, where as the H_2O_2 concentration is increased the hydrated electron yield markedly decreases, with only a small change in the rate of disappearance.

There is little change in the spectrum of the hydrated electron compared to microsecond studies (90), even in molar concentrations of H_2O_2 scavenging occurred exclusively with mobile electrons. However the possible existence of a weakly associated complex consisting of a hydrated electron and the H_2O_2 molecule formed following pre-solvation scavenging of weakly solvated electrons by H_2O_2 might be expected to cause a spectral modification on this time scale.

(3)   The Implications of the Present Results

The general consistency of this work and the stroboscopic picosecond pulse radiolysis results, because of their completely different experimental origins, together constitute a very strong argument for certain modifications of the spur diffusion theory of radiation chemistry. The primary picosecond yield of hydrated electrons in neutral water cannot be as high as previously supposed, $G \sim 4.8$, instead being about $G = 3$, with a concomitantly slower disappearance in intraspur reactions, so that the long time-scale yield of 2.8 is ultimately obtained. An immediate contradiction to this conclusion is the high extrapolated yield of hydrated electrons calculated from scavenger studies at molar solute concentrations (43).

The disparity between these two yields is simply due to the fact that they measure different observables. That is, any scavenger experiments in which the yield of hydrated electrons is deduced from the formation of a chemical product will ultimately predict the primary yield of ionisation in the medium because of the phenomenon of extremely rapid pre-solvation scavenging of electrons, whereas direct physical measurements give only the yield of electrons which become solvated.

Therefore the scavenging results in water may be interpreted to indicate a primary ionisation yeild G $\sim$ 5, of which only 60% of the species survive to become hydrated electrons, G $\sim$ 3.

The mechanism responsible for the extremely rapid disappearance (10^{-12} seconds) of a substantial part of the primary ionization yield must be consistent with an unusual pH dependence. The constancy of the Gε product up to high H_3O^+ concentrations and the dramatic decrease in hydrated electron yield produced by other scavengers imply that the H_3O^+ does not react with unsolvated electrons. Yet the effect of a very high OH^- concentration is to increase the Gε product (for purposes of comparison, measured at 580 nm, ε_{580} = 1.1 x 10^7 (90)) up to G $\sim$ 5.5. These yields have been measured both in picosecond stroboscopic pulse radiolysis experiments (129) and longer time-scale microsecond pulse radiolysis experiments on low temperature alkaline glasses (131) where the effect of decreasing the temperature was to expand the kinetic time scale of radiation chemical events. (An increase in the Gε product in molar concentrations of OH^- was only qualitatively studied in this work because the appearance of a weak luminescence, occurring simultaneously with the pulse, interfered with such measurements).

The proposed mechanism to explain these primary yields and the very short time scale of events ($\sim 10^{-12}$), measured directly (4c), would suggest that the primary ionization produces both mobile free electrons and highly mobile positive holes (H_2O^+, (132)) which are intrinsically capable of undergoing extremely rapid neutralization because of their physical nature. Thus OH^- at a sufficiently high concentration could inhibit this geminate recombination by scavenging holes and so increase the primary yield of hydrated electrons; on the other hand H_3O^+, which has no observable effect on mobile electrons, is only important in the ensuing chemical stage and does not affect the primary yield.

Simultaneously with the occurrence of the initial physicochemical neutralization, the competing processes of electron solvation and H_2O^+ disproportionation will transfer the time scale of events to a chemical basis, resulting in similar initial spatial distributions for the hydrated electron, the hydroxyl radical and H_3O^+ in the spur. A detailed diffusion calculation would be necessary at this stage in order to test the compatability of this model with the long time-scale radiation chemical measurements, however on qualitative arguments, agreement would only require a larger average spur radius in these calculations (44). Moreover the theoretical deviations at high scavenger concentrations would likely be eliminated by the inclusion of the very rapid presolvation scavenging phenomenon which occurs in the physico-chemical stage.

Thus the basic framework of chemical inhomogeneity in the primary chemical events of radiation chemistry remains unaltered. Whereas the hitherto unexplored physico-chemical stage is substantially modified from the currently postulated theoretical model (133), the

interpretation of most radiation chemical measurements will remain for

the most part essentially the same, since few chemical events probe

the picosecond temporal range. The continuity between

steady state and pulse radiolysis studies therefore remains altered.

Nevertheless, this physical insight into the earliest times of

radiation-induced chemical change constitutes a significant advance

in the fundamental understanding of the primary processes of

energy deposition from ionising radiation.

(B) Alcohols

Spur diffusion theories which equate the primary yield

of solvated electrons in a polar medium to the primary ionisation

yield, make contact with the experimental long time-scale observation

of surviving electrons by varying the rate of the electron - positive

ion neutralization process to obtain the correct yield. On this

basis the aliphatic alcohols, which have a microsecond solvated electron

yield of about one-third that of water, would be expected to show a

significant temporal variation in primary yield, approaching the value

for water on a picosecond time-scale (127). Quite the opposite

effect is observed in this work, where the relative primary yields

(as given by the $G\varepsilon$ product) are approximately the same as those observed

in a microsecond studies (Table V). Similar results, although under

the conditions of a high scavenger concentration (H_2SO_4) necessary to

reduce the lifetime of the solvated electron, have also been obtained

fromsome of these alcohols using the stroboscopic pulse radiolysis

technique (4c). In view of the reported primary yields in alcohols

deduced from high concentration scavenger studies (128), it must be concluded, as has been previously proposed for water (section A, this Chapter) that neutralization of the primary ionisation products (ROH^+ and e^-) is also extremely rapid, being complete within 10^{-11} seconds. However the yield of surviving electrons is much lower than that in water.

The relative yields in the alcohols calculated from Table V, using the extinction coefficients from microsecond pulse radiolysis studies, appear to be quite similar (within the 10% uncertainty of these measurements). This observation is in contrast to theoretical predictions (128,134) and experimental measurements (128) which suggest that the primary solvated electron yield in these alcohols (and more generally in polar compounds (135)) is affected by the static dielectric constant of the medium. However, on the basis of the postulated short time-scale for neutralization in these media ($< 10^{-11}$ seconds) from this study; it would be expected that the static dielectric constant would not determine the primary yield. The reason for such a conclusion is that the time-scale required for the static dielectric constant to become effective is too long as compared to the very rapid neutralization, which is complete within $< 10^{-11}$ seconds. Thus, the high frequency dielectric constant may be the more appropriate dielectric property in determining the primary solvated electron yield in polar compounds. The difference in the solvated electron yield in water and the alcohols would then be explained by the anomalously large, high frequency dielectric constant of water $\varepsilon_\infty \sim 5$ (39) as compared to the alcohols when $\varepsilon_\infty \sim 2$.

More experimental measurements of primary solvated electrons are required before this question will be resolved. However the present results show that the role of the long time scale dielectric properties in determining the primary solvated electron yield in polar media (128,134) must be re-examined because of the shrinking temporal dimensions associated with the physicochemical stage of electron escape.

(C) A Critical Assessment of the Cerenkov Reabsorption Technique
     for Pulse Radiolysis

The pulse radiolysis technique of Cerenkov reabsorption spectroscopy developed in this work is a unique departure from previous methods of kinetic spectroscopy. Thus a considerable portion of this work has been devoted to both the methodology of quantiative measurements of this effect and the theoretical relationship between the physical parameters influencing the magnitude of the reabsorption and the experimental data actually obtained. The subsequent application of this technique to pulse radiolysis studies in liquid water has clearly demonstrated the potentialities of Cerenkov absorption measurements. It has been possible to obtain absorption spectra of very short-lived transient species existing for times as short as 30 picoseconds, to determine their primary yields and to estimate their reactivity with added solutes. Yet, the experimental measurements necessary to probe the subnanosecond time scale of events in radiation chemistry were made with nanosecond technology.

(1) Methodology

The experimental techniques which are necessary for the measurement
of the reference and absorbed Cerenkov light pulses are required
only to yield a figure which is proportional to the total light
emission per Cerenkov pulse, because reabsorption is characterized
by the ratio of the number of photons in the reference and absorbed.
Cerenkov light pulses. Thus the spectrographic method of working to
constant density was developed, giving the logarithm of the ratio of
light pulse areas directly while simultaneously accounting for reciprocity
law failure. In spectrophotometric measurements, although pulse distortion
was probably present, such effects would cancel out in the ratio of pulse
areas. This is because external attenuation of the light incident on
the photocathode ensured that the total number of photons per pulse
was the same. The upper and lower limits of the spectral range in this
work are set by different factors. The long wavelength cutoff is
established at about 870 nm by the limit of sensitivity of the high
speed infrared film, the spectrophotometric measurements being made
only as far as 650 nm where the 1P28 photomultiplier becomes insensitive.
Extension of these studies to the infrared should be possible with other
photodetectors or the use of type Z photographic emulsions. However,
it should be noted that the Cerenkov radiation intensity decreases with
increasing wavelength in a λ^{-2} dependency, so that a practical limitation
of measurements in the infrared may be a lack of sufficient sensitivity.
At short wavelengths, quantitative measurements of reabsorption below
$\sim$ 350 nm are limited by difficulties in obtaining a reference Cerenkov
pulse, since most scavengers seem to also have radiation-induced absorptions

in the ultra-violet region. Alternatively the intensity of a reference Cerenkov light pulse can be calculated using the results of Chapter IV, part B, from the emission of an inert compound, such as n-pentane, in which Cerenkov reabsorption would not be expected to occur at these wavelengths. However no experimental confirmation that this compound yields the correct spectral distribution of light emission in this wavelength range has yet been obtained.

(2) Origins of the Time Resolution

From the complicated expression for the absorbance in equation (4-184), there is no intuitive feeling as to why the significant reabsorption of Cerenkov light predicted by the evaluation of this equation shown in figure 4-4 should occur when the absorbing species disappear at rates in excess of 10^{10} M^{-1} sec^{-1}. Consequently it is not immediately obvious how these reabsorption measurements made on a nanosecond time-scale are related to the absorption spectra of transient species with lifetimes as short as 30 picoseconds. This apparent paradox is explained by the relative rates of disappearance of the abosrbing species as compared to their rate of creation by the high energy electron pulse. Thus at the dose-rate of about 2×10^{28} eV cm^{-2} sec^{-1} assuming that all energy is deposited in 0.2 cm, the rate of production of the absorbing species would be about 5×10^6 molar sec^{-1} for a 100 eV yield of G $\sim$ 3.

(This assumes that the absorbing species is a primary product so that its rate of formation will not be a limiting factor.) Then for a species such as the hydrated electron with a very high extinction coefficient, 10^4 M^{-1} sm^{-1}, the rate of growth of absorbance would be 5×10^{10} cm^{-1} sec^{-1}.

Therefore in spite of the very rapid scavenging of the hydrated electron in molar perchloric acid solutions, a significant reabsorption of Cerenkov radiation will be observed, because at these enormous dose-rates, the rates of creation and annihilation of this transient absorbing species are comparable. Such effects may be compared to the phenomenon of non-linear absorption induced by high intensity laser pulses. Conceptually, both Cerenkov reabsorption and non-linear absorption are quite similar effects, although they have completely different physical origins. Non-linear absorption arises because the rate of depopulation of the ground state by absorption of a photon exceeds the rate of decay from the excited state. The temporal capability of Cerenkov reabsorption is achieved because the rate of production of radiation induced absorbing species at very high dose rates is comparable to their rate of disappearance.

Because the experimental observable in Cerenkov reabsorption is the integrated "per pulse" light emission, the kinetic details of the disappearance of the absorbing species cannot be obtained direcly. Computer simulation of the experimental data over a range of scavenger concentrations was used to estimate the rate of disappearance of the hydrated electron in perchloric acid solutions. However, such a calculation requires a priori assumptions about both the kinetic details of the reaction and the primary yield of the absorbing species, so that the results obtained reflect the uncertainty in estimating these parameters. Nevertheless, the fact that kinetic information is not explicitly measured in Cerenkov

reabsorption is the very reason why subnanosecond absorption spectra can be obtained. That is, by integrating over the short time scale details of the dynamic effects which give rise to Cerenkov reabsorption, it is possible to make long time-scale measurements, which can be directly related to short time-scale events.

(3) Possibilities

Table VII presented some data on radiation-induced spectra that were recorded during the course of this work, but were not examined in detail, because their role was more of an incidental one. However this does demonstrate that "everything absorbs somewhere" so that one might expect to observe Cerenkov reabsorption in most compounds because the resulting non-selective ionization and excitation of the medium characteristic of the interaction of high energy radiation. Furthermore, the time resolution of this technique allows one to investigate transient species existing on a time scale, presently inaccessible by normal spectroscopic experiments. The main problem in this method is that all the spectral information is recorded in a single event, and if it is not chemically possible to selectively quench the absorption of a given species then the resulting spectral data may be too complicated to usefully interpret. For example if both short and long-lived strongly absorbing species are produced, the latter must be removed in order to avoid masking the absorption due to the former species. Otherwise the temporal capability of Cerenkov reabsorption cannot be realized. Nevertheless, with experimental ingenuity such problems can be overcome so Cerenkov reabsorption studies offer an opportunity to explore the physical and chemical behaviour of many unusual chemical species.

APPENDIX A

The Evaluation of Equation (4-51)

$$U = \log_{10} \frac{\int_o^b \lambda\, \xi_n \sin \frac{\pi}{b} t \, dt}{\int_o^b \lambda\, \xi_n \sin \frac{\pi}{b} t \exp\left(-2.303\, S_o\left(1 - \cos \frac{\pi}{b} t\right)\right) dt} \qquad (A-1)$$

$\lambda\, \xi_n$ cancels from numerator and denominator, and evaluating the numerator first

$$\int_o^b \sin \frac{\pi}{b} t \, dt = \frac{2b}{\pi} \qquad \text{(equation 47)} \qquad (A-2)$$

next, the denominator

$$\int_o^b \sin \frac{\pi}{b} t \cdot \exp\left(-2.303\, S_o + 2.303\, S_o \cos \frac{\pi}{b} t\right) dt \qquad (A-3)$$

$$= e^{-2.303\, S_o} \int_o^b \sin \frac{\pi}{b} t \exp\left(2.303\, S_o \cos \frac{\pi}{b} t\right) dt$$

The $e^{-2.303\, S_o}$ may be removed from the log to give

$$U = S_o + \log_{10} \frac{2b/\pi}{\int_o^b \sin \frac{\pi}{b} t \exp\left(2.303\, S_o \cos \frac{\pi}{b} t\right) dt} \qquad (A-4)$$

The integral

$$\int_o^b \sin\frac{\pi}{b} t \exp\left(2.303\, S_o \cos\frac{\pi}{b} t\right) dt$$

may be evaluated by substitution giving

$$\frac{b}{\pi} \frac{1}{2.303\, S_o} \left\{ e^{2.303\, S_o} - e^{-2.303\, S_o} \right\} \tag{A-5}$$

and thus substituting into (4-4),

$$U = S_o + \log_{10}\left\{ \frac{\frac{4.606\, S_o}{2.303\, S_o}}{e^{2.303\, S_o} - e^{-2.303\, S_o}} \right\} \tag{A-6}$$

for this work $S_o = 5\,\dfrac{G\,\epsilon}{N_o}\,D_A$ is $\geqslant 2$, so that

$$e^{2.303\, S_o} >> e^{-2.303\, S_o}, \text{ and thus}$$

$$U = S_o - S_o + \log_{10}(4.606\, S_o) \tag{A-7}$$

$$= \log_{10}\left\{ 23.03\,\frac{G\,\epsilon}{N_o}\,D_A \right\}$$

APPENDIX B

The Evaluation of Equation (4-76)

$$U = \log_{10} \frac{\int_o^{\frac{b}{2}} \lambda\, \xi_n\, dt + \int_{\frac{b}{2}}^{b} \lambda\, \xi_n\, (b-t)\, dt}{\int_o^{\frac{b}{2}} dt\, \lambda\, \xi_n\, t\, \exp\left\{-2.303\, T_o\, t^2\right\} + \int_{\frac{b}{2}}^{b} dt\, \lambda\, \xi_n\, (b-t)\, \exp\left\{-2.303\, T_o\, (-t^2 + 2bt - \frac{b^2}{2})\right\}} \tag{B-1}$$

First, $\lambda\, \xi_n$ cancels from the numerator and denomimator, and then the numerator, from (4-56), is equal to $\frac{b^2}{4}$. In the denominator, one has the two integrals,

$$D_1 = \int_o^{\frac{b}{2}} t\, \exp\left\{-2.303\, T_o\, t^2\right\}\, dt \tag{B-2}$$

$$D_2 = \int_{\frac{b}{2}}^{b} (b - t)\, \exp\left\{-2.303\, T_o\, (-t^2 + 2bt - \frac{b^2}{2})\right\} dt \tag{B-5}$$

These integrals may be evaluated by the method of substitution to give

$$D_1 = \frac{1}{2} \left\{- \frac{1}{2.303\, T_o}\right\} \left\{ \exp\left\{-2.303\, T_o\, \frac{b^2}{4}\right\} - 1 \right\} \tag{B-4}$$

$$D_2 = \frac{1}{2} \left\{- \frac{1}{2.303\, T_o}\right\} \left\{ \exp\left\{-2.303\, T_o\, \frac{b^2}{2}\right\} - \exp\left\{-2.303\, T_o\, \frac{b^2}{4}\right\} \right\} \tag{B-5}$$

Thus the argument of the logarithm equals

$$\frac{(4.606)\left(5\, \frac{G\, \epsilon}{N_o}\, D_A\right)}{1 - \exp\left(-(4.606)\, 5\, \frac{G\, \epsilon}{N_o}\, D_A\right)} \tag{B-6}$$

where the substitution $T_o = \left(20 \dfrac{G\,\epsilon\,D_A}{b^2 N_o} \right)$ has also been made.

since $(4.606) \left(5 \dfrac{G\,\epsilon\,D_A}{N_o} \right) \geqslant 4$ for all cases,

$$1 >> \exp\left\{ -(4.606) \left(5 \dfrac{G\,\epsilon\,D_A}{N_o} \right) \right\} \tag{B-7}$$

and the argument of the logarithm reduces to

$(4.606) \left(5 \dfrac{G\,\epsilon\,D_A}{N_o} \right)$ and thus

$$U = \log_{10} \left(23.03 \dfrac{G\,\epsilon\,D_A}{N_o} \right) \tag{B-8}$$

APPENDIX C

The Evaluation of Equation (4-152)

$$U = \log_{10} \frac{\displaystyle\int_{o}^{\frac{b}{2}} t \, dt + \int_{\frac{b}{2}}^{b} (b-t) \, dt}{\displaystyle\int_{o}^{\frac{b}{2}} t \exp\left\{-\frac{2.303}{k_1 b^2} T_1\right\} dt + \int_{\frac{b}{2}}^{b} (b-t) \exp\left\{-\frac{2.303}{k_1 b^2} T_1 (b-t)\right\} dt} \qquad (C-1)$$

As in appendix B, the numerator is equal to $\frac{b^2}{4}$, then in the denominator, the two integrals are

$$\int_{o}^{\frac{b}{2}} t \exp\left\{-\frac{2.303}{k_1 b^2} T_1 \, t\right\} dt = \left\{\frac{k_1 b^2}{2.303 \, T_1}\right\}^2 \left\{1 - \exp\left\{-\frac{2.303}{2 \, k_1 b} T_1\right\} - \left\{\frac{2.303}{2 \, k_1 b} T_1\right\}\right.$$

$$\left. - \exp\left\{\frac{2.303 \, T_1}{2 \, k_1 b}\right\}\right\} \qquad (C-2)$$

$$\int_{\frac{b}{2}}^{b} (b-t) \exp \frac{2.303}{k_1 b^2} T_1 (t-b) \, dt =$$

$$\left[\frac{k_1 b^3}{2.303 \, T_1}\right]\left\{1 - \exp\left\{-\frac{2.303}{2 \, k_1 b} T_1\right\}\right\} + \left[\frac{k_1 b^2}{2.303 \, T_1}\right]^2\left[\left\{\frac{2.303}{k_1 b} T_1 - 1\right\} + \right.$$

$$\left. \exp\left\{-\frac{2.303}{2 \, k_1 b} T_1\right\} - \left\{\frac{2.303}{2 \, k_1 b} T_1\right\} \exp\left\{-\frac{2.303}{2 \, k_1 b} T_1\right\}\right] \qquad (C-3)$$

Upon substitution in (C-1) and combining terms, the argument of the logarithm is

$$= \frac{2.303}{2 \, k_1 b} T_1 \left[\frac{1}{1 - \exp \frac{-2.303}{2 \, k_1 b} T_1}\right] \qquad (C-4)$$

where $T_1 = 40 \dfrac{G \ \epsilon}{N_o} D_A$

The argument of the exponential is

$$(46.06) \quad \frac{G \ \epsilon}{k_1 \ b \ N_o} D_A < 1 \quad \text{for } G \ \epsilon \ \sim 4 \times 10^4$$

since $k_1 > 5 \times 10^{10} \text{ sec}^{-1}, b \sim 4 \times 10^{-9} \text{ sec}$ and $k_1 b > 200$

so that no simplification is possible and

$$U = \log_{10} \left\{ 46.06 \frac{G \ \epsilon}{k_1 \ b \ N_o} D_A \left[\frac{1}{1 - \exp \left\{ - 46.06 \dfrac{G \ \epsilon}{k_1 \ b \ N_o} D_A \right\}} \right] \right\} \qquad \text{(C-5)}$$

APPENDIX D

The Calculation of a 100 eV Yield of Luminescence for Water, Using the

Fluorescence of Sodium Salicylate

Measurements of the light emission from water and 0.5 M

sodium salicylate were made at an accelerator charging voltage of

15 kV, so that the electron energy was $\sim$ 450 keV and the dose reduced

to $\sim$ 5 x 10^{18} eV cm^{-2}. Under these conditions Cerenkov reabsorption

in the sodium salicylate solution will be small (< 10% as calculated

from equation (4-184)) because the rate constant for the reaction

of the electron with salicylate is > 10^{10} M^{-1} sec^{-1} (83). Unabsorbed

Cerenkov emission in water was obtained by the addition of 1 molar H_2O_2.

The relative pulse areas given by the product of the width at half-height

and the peak height of the observed light emission are

    sodium salicylate,   area = 143

    water   ,   area = 91

In order to calculate a G value from the salicylate emission, a number

of adjustments must be made.

(1) Sodium salicylate

    (a) Subtract the Cerenkov radiation observed in water, since

        the light emission from sodium salicylate includes a Cerenkov

        contribution.

    (b) The G value for the whole band is 2.83 x 10^{-3} in 0.5 M

salicylate, however measurements were made at 420 nm, with a 0.2 nm

band pass, so that this G value must be reduced by a factor

of 325 corresponding to a 0.2 nm slice of the emission band.

(c) The salicylate fluorescence is emitted isotropically, where

Cerenkov luminescence is not. Moreover, an exact spatial

dependence of the Cerenkov radiation from the radiation

cell is not known. On the basis of qualitative photographic

estimates of the angular distribution, the Cerenkov emission

is predominantly in the forward direction, spreading broadly

over a region of $\sim 90^{\circ}$ to $\sim 120^{\circ}$. Since the aperture of the

collecting lens is f/1.0, accepting $\sim 52^{\circ}$, the best approximation

is to correct only for the differing spatial distributions of

Cerenkov radiation and fluorescence, assuming that both appear

isotropic to the collimating lens. Thus one divides the

G value for salicylate fluorescence by a factor ranging from

4 (120°) to 6.83 (90°) to take into account the spatial

anisotropy of the Cerenkov emission, with this range the

principle source of the uncertainty in the calculated G value

for Cerenkov emission.

(2) Water

(a) The G value for emission in the 0.2 nm wavelength interval
at 420 nm is

$$\frac{52}{91} \quad \frac{2.83 \times 10^{-3}}{325} \quad \left\{\frac{1}{4} \text{ to } \frac{1}{6.83}\right\}$$

$$= 1.0 \pm .3 \times 10^{-6} \text{ photons } (100 \text{ eV})^{-1}$$

(b) To compare this G value with the calculated yield,

it must be converted to the wavelength region 400 nm - 600 nm ,

hence using the Cerenkov λ^{-2} relationship, one multiplies by

$$\frac{(419.9)(420.1)}{0.2} \frac{(200)}{(600)(400)} = 7.34 \times 10^2$$

so that

$$G_{400-600} = 7.3 \pm 0.3 \text{ photons } (100 \text{ eV})^{-1}$$

and by multiplying by the average electron energy $\sim$ 450 keV,

the photon yield per electron is 3.3 photons per electron,

compared to 4.3 calculated from Chapter IV.

REFERENCES

1. J.P. Keene, Nature 188, 843 (1960).

2. M.S. Matheson and L.M. Dorfman, J. Chem. Phys., 32, 1870 (1960).

3. J.W. Hunt and J.K. Thomas, Radiation Res., 32, 149 (1967).

4. (a) M.J. Bronskill, R.K. Wolff, and J.W. Hunt, J. Phys. Chem., 73, 1175 (1969).

5. (b) M.J. Bronskill, W.B. Taylor, R.K. Wolff, and J.W. Hunt, Rev. Sci. Instr., 41, 333 (1970).

   (c) M.J. Bronskill, R.K. Wolff, and J.W. Hunt, J. Chem. Phys., 53, 4201 (1970).

   (d) R.K. Wolff, M.J. Bronskill, and J.W. Hunt, J. Chem. Phys., 53, 4211 (1970).

5. O. Klein and Y. Nishina, Z. Physik 52, 853 (1929).

6. C.M. Davisson, in α,β, and γ-Ray Spectroscopy, Kai Seigbahn Editor, North Holland, Amsterdam (1955), p. 41.

7. G. Moliere, Z. Naturf. 3a, 78 (1948).

8. R.D. Birkhoff, Handbuch der Physik 34, 53 (1958).

9. C.P. Jupiter, J.A. Lonegan, and G. Merkel, NASA SP169, 249 (1968).

10. M.J. Berger and S.M. Seltzer, NASA SP169, 285 (1968).

11. H.A. Bethe, Ann. Physik 5, 325 (1930).

12. H.A. Bethe, Z. Physik 76, 293 (1932).

13. M.J. Berger and S.M. Seltzer, NASA SP3012,   (1964).

14. M. Burton, K. Funabashi, R.R. Hentz, P.K. Ludwig, J.L. Magee, and A. Mozumder, in Storage and Transfer of Energy in Molecules. A.M. North, Editor, Wiley, London (1970).

15. H.W. Koch and J.W. Motz, Rev. Mod. Physics 31, 920 (1959).

16. P.A. Cerenkov, Dokl. Akad. Nauk. SSSR, 2, 451 (1934).

17. J.V. Jelley, Cerenkov Radiation and its Applications, Pergamon Press, London (1958).

18. I.M. Frank and I. Tamm, Dokl Akad. Nauk. SSSR, 14, 109 (1937).

19. B.M. Bolotovskii, Uspekhi Fizicheskikh Nauk. 62, 201 (1957).

20. D.A. Tidman, Nuclear Physics 2, 289 (1956/57).

21. R. Pratrap, Nuovo Cimento 52B, 63 (1967).

22. E.H. Belcher, Proc. Roy. Soc. A216, 90 (1953).

23. M.A. Greenfield, A. Norman, A.H. Dowdy and P.M. Kratz, J. Opt. Soc. Am. 43, 42 (1953).

24. J.A. Rich, R.E. Slovacek, and F.J. Studer, J. Opt. Soc. Am. 43, 750 (1953).

25. I.M. Frank, Uspekhi Fiz. Nauk. 87, 189 (1965).

26. H.W. Lewis, Phys. Rev. 78, 526 (1950).

27. M.J. Berger, Methods in Computational Physics 1, Academic Press, New York (1963), p. 135.

28. M.J. Kniedler and J. Silverman, Proceedings of a Symposium on the Utilization of Large Radiation Sources and Accelerators in Industrial Processing, Munich, 1969, STI/PUB/236.

29. L.W. Spencer, N.B.S. Monograph 1, 1 (1959).

30. N.D. Kessaris, Radiation Research 43, 281 (1970).

31. M.J. Berger and S.M. Seltzer, NASA SP169, 285 (1968).

32. A Mozumder, Advances in Radiation Chemistry, M. Burton and J.L. Magee Editors, Wiley-Interscience 1, 1 (1969).

33. R.L. Platzman, Proceedings of 3rd International Conference of the Radiation Research Society, G. Silini, Editor, North Holland, Amsterdam (1967), page 20.

34. F. Gutman and L. Lyons, Organic Semiconductors, Wiley, New York (1967).

35. A. Mozumder and J.L. Magee, Radiation Research 28, 203 (1966).

36. A. Mozumder and J.L. Magee, J. Chem. Phys. 45, 3332 (1966).

37. A. Mozumder and J.L. Magee, J. Chem. Phys. 47, 939 (1967).

38. Proceedings of the Symposium on Primary Radiation Effects in Chemistry and Biology, Buenos Aires (1970), W.P. Helman, A. Mozumder and Alberta Ross Editors, page 16.

39. R.L. Platzman, N.A.S./N.R.C. Publication 305, 22 (1953).

40. A.H. Samuel and J.L. Magee, J. Chem. Phys. 21, 1080 (1953).

41. M.L. Matheson and L.M. Dorfman, Pulse Radiolysis, MIT Press, Cambridge, Massachusetts, 1969, page 64.

42. E.J. Hart and R.L. Platzman, Mechanisms in Radiobiology, A. Hollander, Editor, Volume 1, Academic Press, New York (1961), Chapter 2.

43. T.I. Balkas, J.H. Fendler, and R.H. Schuler, J. Phys. Chem. 74, 4497 (1970).

44. H.A. Schwarz, J. Phys. Chem. 73, 1928 (1969).

45. (a) K.H. Schmidt and W. Buck, Science, 151, 70, (1965).

    (b) K.H. Schmidt and S.M. Ander, J. Phys. Chem. 73, 2046 (1969).

46. S. Gordon, E.J. Hart, M.S. Matheson, J. Rabani and J.K. Thomas, J. Am. Chem. Soc., 85, 1375 (1963).

47. E. Collinson, F.S. Dainton, D.R. Smith and S. Tazuké, Proc. Chem. Soc. 140 (1962).

48. (a) E.C. Avery, J.R. Remko and B. Smaller, J. Chem. Phys., 49, 951 (1968).

    (b) B. Smaller, J.R. Remko and E.C. Avery, Proc. IVth Intern. Congress of Rad. Research, Evian, 1970.

49. W.C. Gottschall and E.J. Hart, J. Phys. Chem., 71, 2102 (1967).

50. U. Schindewolf, H. Kohrman and G. Lang, Angew. Chem., 81, 496 (1969).

51. M. Anbar and E.J. Hart, J. Phys. Chem. 69, 1244 (1965).

52. D.C. Walker, Quarterly Reviews, 21, 79 (1967).

53. G.A. Kenney and D.C. Walker, in Electroanalytical Chemistry, Volume 5, Editor, A.J. Bard, Marcel Dekker, New York, 1972, pages 1-66.

54. (a) J. Jortner, Radiation Res. Suppl. 4, 24 (1964).

    (b) D.A. Copeland, N.R. Kestner and J. Jortner, J. Chem. Phys., 1189, 53 (1970).

55. L. Landau, Physik Z., Soviet Union 3, 664 (1933).

56. A.S. Davydov, Zh. Exsperim. Theor. Fiz.,18, 913 (1948).

57. S. Noda, K. Fueki, Z. Kuri, Bull. Chem. Soc. Japan, 42, 16 (1969).

58. K. Iguchi, J. Chem. Phys. 51, 3137 (1969).

59. (a) M. Natori and T. Watanabe, J. Phys. Soc. Japan, 21, 1573 (1966).

    (b) M. Natori, ibid., 24, 913 (1963).

60. B.J. McAloon and B.C. Webster, Theoretica Chim. Acta. (Berl), 15, 385 (1969

61. L. Raff and H. Pohl, Advan. Chem. Soc. 50 (1965).

62. G.A. Kenney-Wallace and D.C. Walker, Conference on Solvated Electrons, Herrenalb (1971).

63. E.J. Hart, E.M. Fielden, and M. Anbar, J. Phys. Chem., 71, 3993 (1967).

64. J.K. Thomas, J. Rabani, M.S. Matheson, E.J. Hart and S. Gordon, J. Phys. Chem., 70, 2409 (1966).

65. M.C. Sauer, S. Arai, and L.M. Dorfman, J. Chem. Phys., 42, 708 (1965).

66. M.S. Matheson and L.M. Dorfman, Pulse Radiolysis, MIT Press, Cambridge Massachusetts, 1969, p. 173.

67. W.V. Sherman, Chem. Comm. 790 (1966).

68. S. Arai, A. Kira, M. Imamura, J. Phys. Chem., 74, 2102 (1970).

69. E.A. Shaede and D.C. Walker, Int. J. Rad. Phys. Chem., 1, 307 (1969).

70. Field Emission Corporation, Published Data Memoranda.

71. F.M. Charbonnier, Field Emission Corporation, Personal Communication.

72. A.M. Bass and K.G. Kessler, J. Opt. Soc. Am., 49, 1223 (1959).

73. M. Churchland, M.Sc. thesis, Department of Physics, University of B.C. (1969

74. G.A. Kenney, Ph.D. Thesis, Department of Chemistry, University of B.C. (1970

75. (a) F.H. Verhoek, J. Am. Chem. Soc., 58, 2577 (1936).

    (b) John Thomas and D. Fennell Evans, J. Phys. Chem., 74, 3812 (1970).

76. J.G. Trump and R.J. Van de Graaf, J. Applied Physics, 19, 599 (1948).

77. E.M. Fielden and S. Lillicrap, Advances in Chemistry Series, 81, 444, (1968).

78. N.E. Dorsey, Properties of Ordinary Water-Substance, van Nostrand-Reinhold Co., Princeton, N.J., 1940, page 279.

79. (a) L.R. Painter, R.N. Hamm, E.T. Arakawa, and R.D. Birkhoff, Physical Rev. Letters, 21, 282 (1968).

    (b) L.R. Painter, R.D. Birkhoff, and E.T. Arakawa, J. Chem. Phys., 51, 243 (1969).

80. E.A. Shaede, M.Sc. Thesis, Dept. of Chemistry, University of British Columbia (1967).

81. D.N. Sitharamarao and J.F. Duncan, J. Am. Chem. Soc., 67, 2126 (1963).

82. G. Stein and Micha Tomkiewicz, NYO-3242-30 (1969).

83. C.B. Amphlett, G.E. Adams and B.D. Michael, Advances in Chemistry Series, 81, 23 (1963).

84. P. Merkel and W. Hamill, J. Chem. Phys., 54, 1695 (1971).

85. M. Hercher and B. Ruff, J. Opt. Soc. Am., 57, 103 (1967).

86. L.S. Birks, R.R. Whitlock, J.S. Vierling, D.J. Nagel, and S.G. Gorbics, J. Opt. Soc. Am., 60, 849 (1970).

87. D.C. Walker and S.C. Wallace, Chem. Phys. Letters 6, 111 (1970).

88. (a) M.C. Sauer, S. Arai, and L.M. Dorfman, J. Chem. Phys., 42, 708 (1965).

    (b) S. Arai and M.C. Sauer, J. Chem. Phys., 44, 2297 (1966).

89. R. Cooper and J.K. Thomas, J. Chem. Phys., 48, 5097 (1968).

90. (a) E.M. Fielden and E.J. Hart, Trans. Faraday Soc., 63, 2975 (1967).

    (b) E.J. Hart, Proc. 19th Farkas Memorial Symposium, G. Stein Editor, Weizmann Science Press, Jerusalem (1968), p. 73.

91. J.P. Keene, Radiation Research 22, 1 (1964).

92. (a) D.A. Head, Ph.D. Thesis, Department of Chemistry, University of British Columbia, (1970).

    (b) D.A. Head and D.C. Walker, Can. J. Chem. 48, 1657 (1970).

93. G.A. Kenney-Wallace and D.C. Walker, J. Chem. Phys., 1282, 53 (1970).

94. N.S. Fel, P.I. Dolin, V.I. Zolotarevskii, Khimiya Vysosikh Energii 1, 154 (1967), translation p. 132.

95. E.J. Hart, E.M. Fielden and M. Anbar, J. Phys. Chem., 71, 3393 (1967).

96. (a) A. Matsumoto and N.N. Lichtin, Advances in Chemistry Series,

    82, 547 (1969).

    (b) N.N. Lichtin, personal communication, 1970.

97. R.L. Platzman and J. Franck, Z. Physik, 138, 411 (1954).

98. M.J. Blandamer, R. Catterall, L. Shields, and M.C.R. Symons,

    J. Chem. Soc., 4357 (1964).

99. M. Anbar and E.J. Hart, J. Phys. Chem., 69, 1244 (1965).

100. M.S. Matheson and L.M. Dorfman, Pulse Radiolysis, M.I.T. Press,

    Cambridge, Massachusetts, 1969, page 168.

101. J.M. Brooks and R.R. Dewald, J. Phys. Chem., 72, 2655 (1968).

102. M.J. Blandamer and M.F. Fox, Chemical Reviews, 59 (1970).

103. M. Smith and M.C.R. Symons, Trans. Faraday Soc., 54, 338 (1958).

104. D. Shapira and A. Treinin, J. Phys. Chem., 70, 305 (1966).

105. J.L. Dye and M.G. DeBacker, J. Chem. Phys., 52, 6251 (1970).

106. U. Schindewolf, Angew. Chemie, 80, 165 (1968).

107. T.R. Griffiths and R.H. Wijayanayake, Trans. Faraday Soc., 67, 1563 (1970).

108. D.M. Brown, F.S. Dainton, J.P. Keene and D.C. Walker, Proc. Chem. Soc.,

    260 (1964).

109. J.K. Thomas, Proceedings of the Symposium on VeryEarly Events,

    Argentina, 1970, page 184.

110. D.M. Brown and F.S. Dainton, Trans. Faraday Soc., 62, 1139 (1966).

111. E.W.T. Richards, A.E.R.E., Rep. No. C/R 1901 (1956).

112. L.O. Brown and N. Miller, Trans. Faraday Soc. 1623, 51 (1955).

113. G. Czapski and D. Katakis, J. Phys. Chem. 2126, 67 (1963).

114. J.L. Magee and M. Burton, J. Am. Chem. Soc. 523, 73 (1951).

115. D. Lewis and W.H. Hamill, J. Chem. Phys. 456, 51 (1969).

116. S. Trajmar, W. Williams and Aron Kupperman, J. Chem. Phys. 2274, 54 (1971).

117. (a) T.J. Smorsk, Proceedings of the Fifth Informal Conference
           on the Radiation Chemistry of Water, Farhatzitz, R.J. Knight,
           I.J. Milner, A. Mozumder and R.J. Povinelli, Editors,
           Radiation Laboratory, University of Notre Dame, Notre Dame,
           Indiana, 1966, page 20.

      (b) T.J. Sworski, Adv. Chem. Series, 163, 50 (1965).

118. E. Hayon, Trans. Faraday Soc. 1059, 60 (1967).

119. M. Anbar, S. Guttman, and G. Stein, J. Chem. Phys. 703, 34 (1961).

120. J.K. Thomas, Advances in Radiation Chemistry, M. Burton and
      J.L. Magee, Editors, Wiley Interscience, 1, 153 (1969).

121. W. Anderson and E.H. Belcher, Brit. J. Appl. Phys. 53, 5 (1954).

122. K. Eiben and I.A. Taub, Nature 782, 216 (1967).

123. K. Fueki, D. Feng, and L. Kevan, J. Phys. Chem. 1976, 74 (1970).

124. A.H. Narten, J. Phys. Chem. 765, 74 (1970).

125. A.H. Narten, Science 447, 165 (1969).

126. H.A. Gillis and D.C. Walker, personal communication.

127. A. Haberstergerová, I. Janovsky and J. Teply, Rad. Res. Rev., $\underline{1}$, 109 (1968).

128. G. Freeman, Adv. Chem. Series, 339, $\underline{82}$ (1968).

129. J.W. Hunt, personal communication (1971).

130. Noyes, Prog. Reaction Kinetics.

131. G.V. Buxton, F.C.R. Cattell and F.S. Dainton, Chem. Comm. 23 (1971).

132. J.J. Weiss, Nature, $\underline{186}$, 751 (1960).

133. J.L. Magee, Proceedings of the Symposium on Very Early Events, Argentina, 1970, pages 1-15.

134. (a) A. Mozumder, J. Chem. Phys. 3153, $\underline{50}$ (1969).

    (b) A. Mozumder, J. Chem. Phys. 3162, $\underline{50}$ (1969).